Thesis

Experimental Demonstration of Back-Linked Fabry–Perot Interferometer for the Space Gravitational Wave Antenna

Ryosuke Sugimoto

Department of Space and Astronautical Science
School of Physical Sciences

The Graduate University for Advanced Studies, SOKENDAI

March 2024

Abstract

Since the groundbreaking observation of gravitational waves radiated from a binary black hole by Laser Interferometer Gravitational-Wave Observatory (LIGO) in 2015, the network of terrestrial gravitational wave interferometers finished conducting three observing runs in March 2020, reporting the observations of 90 gravitational wave event candidates from compact binary coalescences. Currently, the terrestrial network is in the fourth observing run. All the events so far were identified to be those radiated from binary systems consisting of either two neutron stars, two stellar-mass black holes or a combination of the two. They are found to be in the mass range of $1 - 100\ M_{\odot}$, corresponding to the observation frequency band of 10 Hz-1 kHz. In June 2023, the North American Nanohertz Observatory for Gravitational Wave, one of the pulsar timing array (PTA) experiments, reported the observational evidence of the detection of an nHz gravitational wave background, likely from the ensemble of supermassive black hole binaries.

On the other hand, the frequency band of mHz-10 Hz remains unexplored as a frequency gap, given the fact that the frequency band of terrestrial interferometers is limited by ground vibration noises and that of the PTA experiments is limited by the integration time. Complementing this gap is of high importance because it would offer observations of the binary systems of new mass range and cosmological sources. Several strategies, such as LISA, B-DECIGO, and DECIGO, have been proposed for space-borne interferometer missions to essentially avoid the terrestrial environment and exploit this frequency band.

In particular, B-DECIGO, an inter-satellite Fabry-Perot interferometer, has the potential to achieve a high sensitivity in the 0.1 Hz band. It is capable of observing the intermediate-mass black hole binaries with a total mass of $100 - 10^4 M_{\odot}$ up to a redshift of ~ 300 with a signal-to-noise ratio of 8. It will also be capable of detecting binary neutron stars before they merge. For instance, B-DECIGO should be able to detect such a system 7 years before the merger if it is at a distance of 40 Mpc comparable to GW170817. DECIGO, the ambitious successor of B-DECIGO, will improve the sensitivity by an order of magnitude and is hoped to achieve a direct observation of primordial gravitational wave backgrounds.

The back-linked Fabry-Perot interferometer (BLFPI) was proposed as an interferometer topology using the inter-satellite Fabry-Perot interferometers. We colloquially call the Fabry-Perot interferometer the Fabry-Perot cavity or cavity in short, hereafter. The BLFPI keeps all the cavities at a resonance by controlling the laser frequencies only, thus avoiding the need for precision control of

the inter-satellite distances at an unprecedented precision level of nanometers. Such a precision control would be required if the resonances were maintained by controlling the physical lengths of cavities. The BLFPI is expected to overcome the serious design problem where the amount of propellant stringently limits the length of the observation period due to continuous control of the satellite positions. In addition, if the inter-satellite cavity lengths were controlled for keeping the resonances, one cavity length degree of freedom would need to be left uncontrolled, requiring an additional adjustment for the cavity lengths. Since the BLFPI employs a simple control configuration in which each laser is locked to each corresponding cavity, there is no restrictions on the values of cavity lengths, allowing the satellites to form an arbitrary and time-variant triangular formation. Finally, the simple configuration makes the in-orbit operations more tractable such as lock acquisition.

While the BLFPI offers several advantages, it is vulnerable to laser frequency noises which would significantly deteriorate the observatory sensitivity if unaddressed. For the reason, the BLFPI was proposed together with a new offline noise subtraction scheme similarly to time-delay interferometry. In the BLFPI, the heterodyne beatnote signals are obtained by optically connecting the two lasers with an optical fiber called the back-link similarly to LISA in addition to the error signals from each cavity. The success of BLFPI heavily relies on this subtraction process which has not experimentally been tested to date.

This thesis reports an experimental demonstration of the BLFPI. A miniature of the BLFPI was built on an optical bench with the main aim of validating the critical function called the frequency noise subtraction. We show that the frequency noise can be subtracted to a suppression ratio of 188 ± 29 and discuss the current limitations for the subtraction ratio.

The results of this thesis have been published in Physical Review D in January 2024.

Revision history
Pre-Edition: Submitted on Oct. 13, 2023
1st Edition: Submitted on Jan. 10, 2024
2nd Edition: Submitted on Jan. 31, 2024

CONTENTS

LIST OF FIGURES

LIST OF TABLES

GLOSSARY

System of Units and Abbreviations in this Thesis

· The International System of Units is used in this paper unless otherwise noted.
· In tensor notation, superscripts and subscripts denote contravariant and covariate components, respectively.
· The Einstein rule is adopted, and when there are the same subscripts in the same term, the subscripts are assumed to be summed.
· The alphabetic subscripts represent one of the three space components (or one of the two laser loops), while the Greek subscripts represent one of the four space-time components.
· A comma denotes a partial derivative.

Symbols

i	imaginary unit
c	speed of light
G	Newtonian constant of gravitation
h	Planck's constant
$\hbar$	Dirac's constant: $\hbar = h/2\pi$
k_B	Boltzmann constant
$M_\odot$	Solar mass
E	Electric field
$\mathcal{F}$	Cavity finesse
f	Fourier frequency
$h(t)$, $h(\Omega)$	Strain of gravitational waves
L	Cavity length
P	Optical power
λ	Wavelength of light
Ω	Sideband or Fourier (angular) frequency
ω	Carrier (angular) frequency

Abbreviations

ADC	Analog to Digital Converter
ASD	Amplitude Spectral Density
BBH	Binary Black Hole
BH	Black Hole
BLFPI	Back-Linked Fabry–Perot Interferometer
BNS	Binary Neutron Star
BS	Beam Splitter
DoF	Degree of Freedom
DPDFP	dual-pass Differential Fabry-Perot
EOM	Electro-Optical Modulator
FG	Function Generator
FP	Fabry-Perot
FSR	Free Spectral Range
LO	Local Oscillator
NS	Neutron Star
OLTF	Open loop Transfer Function
OTP	Optical Transponders
PD	Photodiode/Photodetector
PDH	Pound Drever Hall
PGW	Primordial Gravitational Wave
PLL	Phase-Locked Loop
PSD	Power Spectral Density
RF	Radio Frequency
RIN	Relative Intensity Noise
RMS	Root Mean Square
RP	Radiation Pressure
S/C	Space Craft
TF	Transfer Function
TT	Transverse Traceless
VCO	Voltage-Controlled Oscillator
WD	White Dwarf

Chapter 1
INTRODUCTION

Gravitational wave is a ripple of space-time which is derived from the general theory of relativity. Since gravitational waves have extremely small interactions with matter, they are essentially not absorbed or scattered by matter. Therefore, the gravitational wave observations provide complementary insights to the conventional electromagnetic wave observations in astronomy.

Since the groundbreaking observation of gravitational waves radiated from a binary black hole in 2015 [1], the network of terrestrial gravitational wave interferometers finished conducting three observing runs in March 2020, reporting the observations of 90 gravitational wave event candidates from compact binary coalescences [2]. Currently, the terrestrial network is in the fourth observing run. All the events so far were identified to be those radiated from binary systems consisting of either two neutron stars, two stellar mass black holes or the combination of the two. They are found to be in the mass range of 1-100 $M_{\odot}$, corresponding to the observation frequency band of 10 Hz-1 kHz [3]. In June 2023, the North American Nanohertz Observatory for Gravitational Wave, one of the pulsar timing array (PTA) experiments, reported the observational evidence of detection of a nHz gravitational wave background, likely from the ensemble of supermassive black hole binaries [4].

The direct detection of gravitational waves is realized by measuring the variation of the distance between the test masses using the light. The observation bandwidth of a detector is determined mainly by the time that light travels between the test masses and the environment in which the detector is placed. In an approximation, the longer the baseline length between the test masses, the larger the length variation for the gravitational wave with the same amplitude. However, if the travel time of the light is longer than the period of the gravitational wave, the sensitivitiy diminishes because the wave effect is integrated and canceled out. For example, it is difficult for the PTA, which has a baseline length of several light years, to attain high sensitivity at frequencies higher than nHz. On the other hand, ground-based detectors are not suitable for observations at frequencies lower than approximately 10 Hz because of the effects of ground vibrations and variations in the local gravity field [5]. For the above reasons, the frequency band of mHz – 10 Hz which corresponds to the region between the PTA and the ground-based detector remains unexplored as a frequency gap.

Complementing this gap is of high importance because it would offer observations of the binary systems of new mass range [6, 7], and cosmological sources [8, 9]. Several strategies have been proposed to fill the frequency gap. They include plans to utilize torsional pendulums with low resonant frequency for effective vibration isolation, as represented by TOBA [10]; atomic interferometers that employ free-fall atoms to mitigate disturbances, such as AION [11], ZAIGA [12], and AEDGE [13]; plans to utilize the stable cryogenic materials to remove seismic noise with a high common mode rejection, exemplified by SOGRO [14], as well as a number of space-borne interferometer missions proposals, that essentially avoid the terrestrial environment, such as LISA [15], Taiji [16], TianQin [17], BBO [18], TianGO [19], B-DECIGO, DECIGO and other concepts [20]. Examples of sources and corresponding observation methods for each frequency band are shown in Fig. 1.1 [21].

In particular, B-DECIGO [22] employs the inter-satellite Fabry-Perot cavity. The Fabry-Perot cavity is a an interferometric device that resonates light between the mirrors. In the resonant state, the light circulates within the cavity and remains for a longer period of time. As a result, higher sensitivity can be obtained comparing against the ones without the cavity. Most of the space detectors employ a triangular configuration consisting of three spacecraft. In B-DECIGO, the optical cavities constitute three sides of a triangular configuration. A schematic view of DECIGO is shown in Fig. 1.2. This geometry was adopted for calibration and redundancy, as well as for improved sensitivity to the polarization of gravitational waves [23].

B-DECIGO has the potential to achieve a high sensitivity in the 0.1 Hz band. It is capable of observing the intermediate-mass black hole binaries with a total mass of 100-$10^4 M_\odot$ up to a redshift of ~ 300 with a signal-to-noise ratio of 8. The intermediate-mass black holes are candidates for the origin of supermassive black holes such as the one at the center of our galaxy. The observation of intermediate-mass black holes and understanding their mass distribution are important for identifying the formation scenario of supermassive black holes [6]. It will also be capable of detecting binary neutron stars before they merge. For instance, B-DECIGO should be able to detect such a system 7 years before the

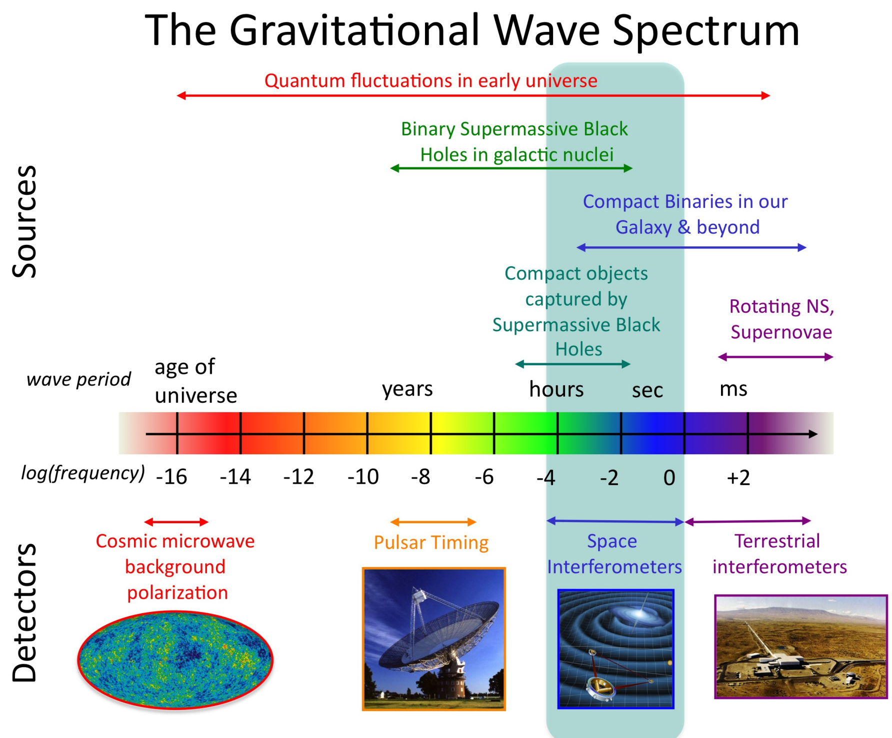

Figure 1.1: Examples of expected science and observation methods for the gravitational waves in each frequency band. Credit: NASA Goddard Space Flight Center [21]

merger if it is at a distance of 40 Mpc [25] comparable to GW170817 [26]. The early detection of binary neutron stars makes multi-messenger astronomy more complete with the electromagnetic observations [27]. In addition, the long time observations associated with early detection will allow the precise verification of general relativity [28] and the direct measurement of the expansion of the universe [29].

DECIGO, the ambitious successor of B-DECIGO, will improve the sensitivity by an order of magnitude. Since the 0.1-Hz band is less affected by the white dwarf binary foreground, it is hoped to achieve a direct observation of primordial gravitational wave (PGW) from the early universe [24]. The measurement of the spectral structure of the PGW provides very important information on various key physics, including thermal history of the universe after inflation, dark en-

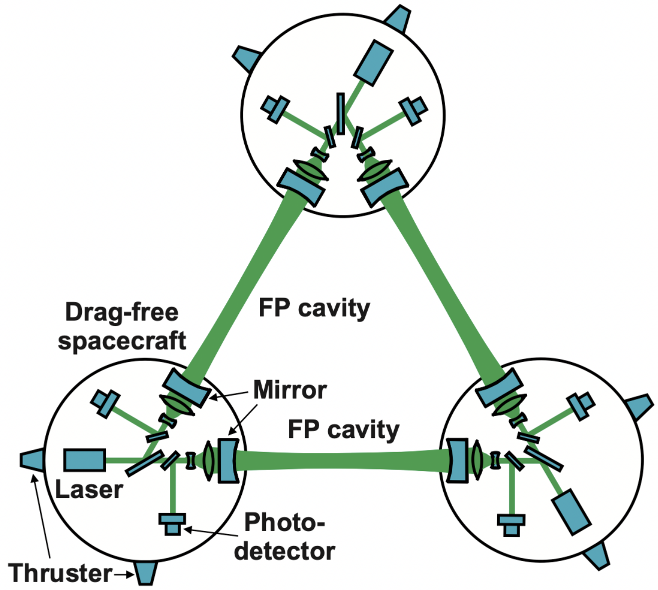

Figure 1.2: Schematic view of B-DECIGO (or DECIGO). In B-DECIGO, the optical cavities constitute three sides of a triangular. [24]

ergy, and first order phase transition dynamics, and verification of the inflation theory [9, 30–34].

The back-linked Fabry-Perot interferometer (BLFPI) was proposed [35] as an interferometer topology using the inter-satellite Fabry-Perot interferometers. We colloquially call the Fabry-Perot interferometer the Fabry-Perot cavity or cavity in short, hereafter. The BLFPI keeps all the cavities at a resonance by controlling the laser frequencies only, thus avoiding the need for precision control of the inter-satellite distances at an unprecedented precision level of nanometers. Such a precision control would be required if the resonances were maintained by controlling the physical lengths of cavities. The BLFPI is expected to overcome the serious design problem where the amount of propellant stringently limits the length of the observation period due to continuous control of the satellite positions. In addition, if the inter-satellite cavity lengths were controlled for keeping the resonances, one cavity length degree of freedom would need to be left uncontrolled, requiring an additional adjustment for the cavity lengths [36]. Since the BLFPI employs a simple control configuration in which each laser is locked to each corresponding cavity, there is no restrictions on the values of cavity lengths, allowing the satellites to form an arbitrary and time-variant triangular formation. Finally, the simple configuration makes the in-orbit operations more tractable such as lock acquisition.

While the BLFPI offers several advantages, it is vulnerable to laser frequency noises which would significantly deteriorate the observatory sensitivity if unaddressed. For the reason, the BLFPI was proposed together with a new offline noise subtraction scheme similarly to time-delay interferometry [37]. In the BLFPI, the heterodyne beatnote signals are obtained by optically connecting the two lasers with an optical fiber called the back-link similarly to LISA [38–40] in addition to the error signals from each cavity. The success of BLFPI heavily relies on this subtraction process which has not experimentally been tested to date.

This thesis for the first time reports an experimental demonstration of the BLFPI. A miniature of the BLFPI was built on an optical bench with the main aim of validating the frequency noise subtraction. We show that the frequency noise can be subtracted to a suppression ratio of 188 ± 29 and discuss the current limitations for the subtraction ratio.

This thesis is organized as follows. In Chapt 2, gravitational waves are derived from general relativity. Subsequently, their properties are summarized, typical examples of the radiation sources are presented. In Chapt 3, we will review the properties of the Michelson interferometer and Fabry-Perot cavity, both of which are the basis of laser interferometric gravitational wave detectors. Then summarize the main noise sources in gravitational wave detection. In Chapt 4, I introduce the frequency noise subtraction scheme and show that the frequency noises can be subtracted while leaving the gravitational wave signals or equivalently the length signals unaffected. In Chapt 5, the experimental setup and the implementation of the offline subtraction process are presented. In Chapt 6, it is shown that the laser frequency noises were successfully reduced by applying the subtraction process to the data acquired in the experiment . After that I discusses a number of sources that could limit the noise subtraction ratio and the implication to the space gravitational wave antennas. Finally, Chapt 7 conludes the thesis.

Chapter 2
GRAVITATIONAL WAVES

In this chapter, we derive the gravitational wave from the general theory of relativity and show that the gravitational wave has two tensor polarization modes. We then consider the effect of each polarization mode on the free masses, and consider the radiation of gravitational waves. Finally, we present the possible radiation sources.

2.1 Derivation of gravitational waves

2.1.1 Einstein equations in a weak gravitational field

In general relativity, the line element ds between two infinitesimally different points in 4-dimensional space-time, x^μ and $x^\mu + dx^\mu$, can be expressed as

$$ds^2 = g_{\mu\nu} dx^\mu dx^\nu, \tag{2.1}$$

with the metric tensor $g_{\mu\nu}$. When space-time is flat, the metric tensor coincides with the Minkovski metric tensor $\eta_{\mu\nu}$. We adopt $\eta_{\mu\nu} = \mathrm{diag}[-1, 1, 1, 1]$ in this thesis. The metric tensor follows the Einstein equation

$$G_{\mu\nu} = \frac{8\pi G}{c^4} T_{\mu\nu}. \tag{2.2}$$

Where $T_{\mu\nu}$ is the stress–energy tensor which represents the density and flux of energy and momentum of an object in spacetime. The Einstein tensor $G_{\mu\nu}$ is defined as

$$G_{\mu\nu} \equiv R_{\mu\nu} - \frac{1}{2} g_{\mu\nu} R, \tag{2.3}$$

using the Ricci tensor $R_{\mu\nu}$ and the scalar curvature R. We also define the curvature tensor $R^{\mu}_{\nu\alpha\beta}$ which expresses the distortion of space-time, as

$$\begin{aligned} R^{\mu}_{\nu\alpha\beta} &\equiv \Gamma^{\mu}_{\nu\beta,\alpha} - \Gamma^{\mu}_{\nu\alpha,\beta} + \Gamma^{\mu}_{\gamma\alpha}\Gamma^{\gamma}_{\nu\beta} - \Gamma^{\mu}_{\gamma\beta}\Gamma^{\gamma}_{\nu\alpha}, \\ \Gamma^{\mu}_{\nu\lambda} &\equiv \frac{1}{2} g^{\mu\alpha}\left(g_{\alpha\nu,\lambda} + g_{\alpha\lambda,\nu} - g_{\nu\lambda,\alpha}\right). \end{aligned} \tag{2.4}$$

The Rich tensor and scalar curvature are defined, respectively, from the contraction of the curvature tensor as

$$\begin{aligned} R_{\mu\nu} &\equiv R^{\alpha}{}_{\mu\alpha\nu}, \\ R &\equiv R^{\mu}_{\mu}. \end{aligned} \tag{2.5}$$

Assuming that the gravitational field is sufficiently small where $|h_{\mu\nu}| \ll 1$, the space-time metric is expressed as

$$g_{\mu\nu} = \eta_{\mu\nu} + h_{\mu\nu}, \tag{2.6}$$

using the Minkowski metric and the perturbation from the Minkowski metric. By plugging $g_{\mu\nu}$ into Einstein tensor, we can obtain

$$G_{\alpha\beta} = \frac{-1}{2}\left(h_{\alpha\beta,\mu}{}^{,\mu} + \eta_{\alpha\beta}\bar{h}_{\mu\nu}, \mu\nu - \bar{h}^{,\mu}_{\alpha\mu,\beta} - \bar{h}^{,\mu}_{\beta\mu,\alpha} + O\left({h_{\alpha\beta}}^2\right)\right). \tag{2.7}$$

Here, we defined the trace reverse tensor of $h_{\alpha\beta}$ as follows.

$$\bar{h}_{\alpha\beta} = h_{\alpha\beta} - \frac{1}{2}h, \tag{2.8}$$

with $h \equiv h^{\alpha}_{\alpha}$. Here, by performing a gauge transformation to coordinates satisfying the following conditions,

$$\bar{h}^{\mu\nu}{}_{,\nu} = 0, \tag{2.9}$$

we get

$$G_{\alpha\beta} = \frac{-1}{2}\Box\bar{h}_{\alpha\beta}, \tag{2.10}$$

where $\Box$ is the four-dimensional Laplacian. From Eq. (2.2) and (2.10) we finally arrive to the Einstein equations in a weak gravitational field

$$\Box\bar{h}^{\mu\nu} = -\frac{16\pi G}{c^4}T^{\mu\nu}. \tag{2.11}$$

This equation shows that $\bar{h}^{\mu\nu}$, the deviation of the metric tensor with respect to $\eta_{\mu\nu}$, propagates as waves in space-time, i.e., the existence of the gravitational wave.

2.1.2 Derivation of gravitational waves

In a vacuum sufficiently far away from the gravitational source ($T^{\mu\nu} = 0$), Eq. (2.11) becomes

$$\Box \bar{h}^{\alpha\beta} = 0. \tag{2.12}$$

Furthermore, by imposing a transverse trackless (TT) gauge condition, we write as,

$$h^{\alpha}{}_{\alpha} = 0, \tag{2.13}$$

$$h_{\alpha\beta} U^{\beta} = 0. \tag{2.14}$$

Where U^{β} is some fixed four-velocity vector. Here, the following two conditions can be satisfied if we choose a basis vector of time as U^{β} and set the direction of wave propagation to the z-axis [41],

$$\begin{aligned} h_{\alpha 0} &= 0, \\ h_{\alpha z} &= 0. \end{aligned} \tag{2.15}$$

From the symmetry of the Einstein tensor $G_{\mu\nu}$ and the conditions of (2.15), all the components except h_{xx}, h_{yy} and $h_{xy} = h_{yx}$ are zero. In addition, from the traceless condition (2.13), $h_{yy} = -h_{xx}$ is obtained.

From the above, the solution of Eq. (2.12), can be represented with independent functions $h_{xx}(t)$ and $h_{xy}(t)$ as follows

$$h_{\alpha\beta} = \begin{bmatrix} 0 & 0 & 0 & 0 \\ 0 & h_{xx}\left(t - \frac{z}{c}\right) & h_{xy}\left(t - \frac{z}{c}\right) & 0 \\ 0 & h_{xy}\left(t - \frac{z}{c}\right) & -h_{xx}\left(t - \frac{z}{c}\right) & 0 \\ 0 & 0 & 0 & 0 \end{bmatrix}. \tag{2.16}$$

Note that $h_{\alpha\beta} = \bar{h}_{\alpha\beta}$ since $\eta^{\alpha\beta} h_{\alpha\beta} = 0$ in the TT gauge condition.

The above shows that gravitational wave in general relativity propagates at the speed of light and has two independent polarizations h_{xx} and h_{xy}.

2.1.3 Effects of gravitational waves

Let us consider the situation where the point masses with no external force are placed at the coordinates $(ct, L\cos\theta, L\sin\theta, 0)$ on the xy-plane. The gravitational waves propagating in the z-axis direction pass through.

First, assuming only h_{xx} polarization in the gravitational wave, $h^{\alpha\beta}$ can be represented by

$$h^{\alpha\beta} = \begin{pmatrix} 0 & 0 & 0 & 0 \\ 0 & h_{xx} & 0 & 0 \\ 0 & 0 & -h_{xx} & 0 \\ 0 & 0 & 0 & 0 \end{pmatrix} \cos\phi t. \tag{2.17}$$

Here $h^\alpha\beta$ has assumed to oscillate with $\cos\phi t$. The proper distance Δl between the origin $(ct, 0, 0, 0)$ and the point masses can be expressed as follows.

$$\begin{aligned} \Delta l &= \int \left| g_{\alpha\beta} dx^\alpha dx^\beta \right|^{\frac{1}{2}}, \\ &= \int \left| (\eta_{\alpha\beta} + h_{\alpha\beta}) dx^\alpha dx^\beta \right|^{\frac{1}{2}}, \\ &= \sqrt{\int_0^{L\cos\theta} (1 + h_+ \cos\phi t)\, dx^2 + \int_0^{L\sin\theta} (1 - h_+ \cos\phi t)\, dy^2}, \\ &\simeq L\left(1 + \frac{1}{2} h_+ \cos 2\theta \cos\phi t\right). \end{aligned} \tag{2.18}$$

Here we assumed $h \ll 1$.

Next, similarly, assuming the h_{xy} polarization only, the proper distance Δl is obtained as follows.

$$\Delta l \simeq L\left(1 + \frac{1}{2} h_\times \sin 2\theta \cos\phi t\right). \tag{2.19}$$

A depiction of the time evolution of the free masses for each condition is shown in Fig. 2.1. It can be seen that the gravitational waves induce tidal variations. The gravitational wave detector, presented later in Chapt. 3, measures the variation of this proper distance. The fact that the variation of the proper distance is proportional to the separation length L is the essential reason why huge gravitational wave detectors are needed.

The polarization modes h_{xx} and h_{xy} are called $+$ mode and $\times$ mode, respectively.

2.2 Gravitational wave radiations

In this section, we consider the radiation of gravitational waves from the solution of the wave equation derived in Eq. (2.11). An order estimations are performed for the GW amplitudes. Finally, specific radiation sources are introduced.

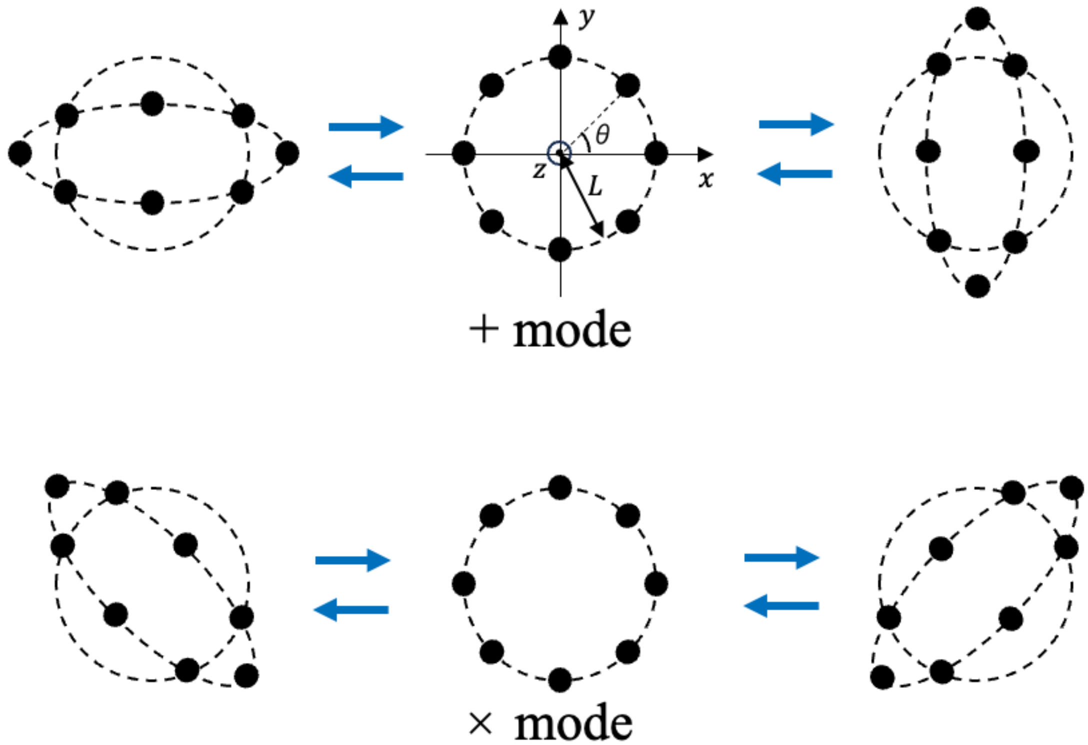

Figure 2.1: The time evolution of a free masses when a gravitational wave of each polarization mode arrives from the z-axis direction. The blue arrows represent time evolution.

Let us consider the radiation of gravitational waves. The solution of Eq. (2.11) is formally written as

$$\bar{h}^{\mu\nu}\left(t, x^{i}\right) = \frac{4G}{c^{4}} \int \frac{T^{\mu\nu}\left(t - \frac{\left|x^{i} - x^{i'}\right|}{c}, x^{i'}\right)}{\left|x^{i} - x^{i'}\right|} d^{3}x^{i'}, \tag{2.20}$$

where x^{i} is the position vector of the observer and $x^{i'}$ is the position vector of the gravitational wave radiation source. Assuming that $|x^{i}| \equiv r \gg \left|x^{i'}\right|$ and that the time derivative of $T^{\mu\nu}$ is small enough (i.e., the change of the radiation source is sufficiently slow relative to the speed of light), Eq. (2.20) can be approximated as

$$\bar{h}^{\mu\nu}\left(t, x^{i}\right) \simeq \frac{4G}{c^{4}r} \int T^{\mu\nu}\left(t - \frac{\left|x^{i} - x^{i'}\right|}{c}, x^{i'}\right) d^{3}x^{i'}. \tag{2.21}$$

In addition, from the laws of conservation of energy and momentum,

$$T^{\mu\nu}{}_{,\nu} = 0. \tag{2.22}$$

The lowest moment revelant to gravitational wave radiation is the quadrupole, so that

$$\bar{h}^{jk}(t, x^i) \simeq \frac{2G}{c^4 r}\ddot{I}^{jk}(t - r/c), \tag{2.23}$$

with, the quadrupole moment tensor

$$I^{jk}(t) \equiv \int x^j x^k T^{00}(t, x^i) d^3x^i. \tag{2.24}$$

Under the TT gauge conditions, Eq.(2.23) can write as

$$\begin{aligned} h_{ij}^{TT} &= \frac{2G}{c^4 r}\frac{d^2 I_{ij}^{TT}}{dt^2}, \\ &= \left[P_i^k P_j^l - \frac{1}{2}P_{ij}P^{kl}\right]\frac{2G}{c^4 r}\frac{d^2 I_{ij}}{dt^2}, \end{aligned} \tag{2.25}$$

with

$$\mathrm{I}_{ij} \equiv I_{ij} - \frac{1}{3}\delta_{ij}I_k^k, \tag{2.26}$$

and

$$P_i^k \equiv \delta_i^k - n_i n^k, \tag{2.27}$$

where

$$\delta_j^i = \begin{cases} 0 & (i \neq j) \\ 1 & (i = j) \end{cases}, \tag{2.28}$$

and unit radial normal n_i. Let T^{00} be approximated by the density ρ and let M be its spatial integral. In addition, we assume that the characteristic size of the gravitational wave source and the time scale of variation are R and T, respectively. The quadrupole moment can be approximated as MR^2 and its second time derivative as $MR^2/T^2 \sim Mv^2$ with the characteristic velocity v defined as $v \equiv R/T$. Therefore, the gravitational wave amplitude can be approximated as

$$h \sim \delta\frac{GM}{c^2 r}\frac{v^2}{c^2} = \delta\frac{R}{r}\frac{GM}{c^2 R}\frac{v^2}{c^2} \simeq 10^{-44}\delta\frac{Mv^2}{r}. \tag{2.29}$$

Here δ represents the asymmetry of the system ($\delta \leq 1$) and GM/c^2R is a dimensionless quantity that expresses the compactness of the radiation source. The above shows that gravitational waves are emitted strongly when a denser object is moving at a higher speed. For example, subsitiuting the parameters comparable to GW150914, i.e., $M = 30\ M_\odot$, 400 Mpc distance, and $0.6c$ as the velocity just before the merger, we get $h \sim 10^{-21}$. Here, δ is set to 1 for simplicity.

2.3 Possible radiation sources of gravitational wave

The following are examples of the possible sources of gravitational wave radiation.

2.3.1 Compact binary coalescence

As we have seen in Eq. (2.29), a binary system consisting of compact objects is one of the typical radiation sources of gravitational wave. The compact objects include black holes (BHs), neutron stars (NSs) and white dwarfs (WDs). Over 90 gravitational wave events have been reported by ground-based detectors namely LIGO and Virgo to date, after the first detection in 2015 [1,42]. All of these events are radiated from CBC and are identified to be combinations of of either BH-BH, BH-NS or NS-NS. In June 2023, NANOGrav, one of the Pulsar Timing Array (PTA) experiments, reported the detection of nHz band gravitational waves that possibly originated from a supermassive BH binary [4].

The orbital radius of the binary system decreases due to the energy loss caused by the gravitational wave radiation. As a result, its orbital velocity increases. With the evolution of the inspiral, both the amplitude and frequency of the radiated gravitational wave increase. This process is called the chirp phase. When the orbital radius reaches the innermost stable circular orbit (ISCO), which is the limit of a stable orbit, the binary object reaches a merger. And it emits a strong burst wave. After the merger, a new BH is formed in the case of binary BH system and the gravitational wave is radiated due to the quasi-normal Mode excited by the merger. Although, fundamentally, even in the case of binary NS systems, a BH is formed after the merger, it has been suggested that a large NS could exist for a short period of time after the merger, depending on the equation of state of the NS [43]. In binary WD systems with low total masses, the system might form a heavier white dwarf or yellow supergiant. If the binary mass is close to or exceeds the Chandrasekhar mass, a Type Ia supernova might occur. As shown later, such supernovae could also be a gravitational wave source [44].

Historically, the existence of the gravitational wave was first verified by the electromagnetic observation of the NS pulsar, as the decrease of the orbital period was consistent with the value expected from the energy loss due to the gravitational wave radiation [45].

The time evolution of the gravitational wave amplitude from the binary system during the chirp phase $h(t)$ in detector frame and its phase Φ_{GW} and frequency f_{GW} can be expressed as follows [46].

$$h(t) \simeq \frac{4}{d_{\mathrm{L}}}\left(\frac{GM_c}{c^3}\right)^{5/3}\left(\frac{\pi f_{\mathrm{GW}}(t)}{c}\right)^{2/3}\cos\left(\Phi_{\mathrm{GW}}(t)\right), \tag{2.30}$$

$$\Phi_{\mathrm{GW}}(\tau) = -2\left(\frac{5GM_c}{c^3}\right)^{-5/8}\tau^{5/8} + \phi_0, \tag{2.31}$$

$$\begin{aligned} f_{\mathrm{GW}}(\tau) &= \frac{1}{2\pi}\frac{\partial \Phi_{\mathrm{GW}}(\tau)}{\partial \tau}, \\ &= \frac{1}{\pi}\left(\frac{5}{256}\frac{1}{\tau}\right)^{3/8}\left(\frac{GM_c}{c^3}\right)^{-5/8}, \end{aligned} \tag{2.32}$$

where d_L is the luminosity distance, τ is the time taken to merge and is defined by $\tau \equiv t_{\mathrm{col}} - t$ using the collision time t_{col}, ϕ_0 is the phase factor, M_c is the chirp mass. The chirp mass is defined as

$$M_c = \frac{(m_1 m_2)^{3/5}}{(m_1 + m_2)^{1/5}}, \tag{2.33}$$

when the masses of the stars constituting the binary system are m_1 and m_2, respectively. The orbital frequency of the binary reaches the maximum when its orbit reaches ISCO. The gravitational wave frequency f_{ISCO} at that time can be expressed as follows [46].

$$\begin{aligned} f_{\mathrm{ISCO}} &= \frac{1}{12\sqrt{6}\pi}\frac{c^3}{GM}, \\ &\simeq 2.2 \times 10^3\left(\frac{M_\odot}{M}\right), \end{aligned} \tag{2.34}$$

where $M = m_1 + m_2$.

As seen from the above equation, heavier stars merge at a lower frequency of their inspiral. The gravitational wave amplitude in the chirp phase of the above equation in detector frame can be expressed as follows [46].

$$\begin{aligned} h(f_{\mathrm{GW}}) \simeq& \frac{1}{\pi^{2/3}}\left(\frac{5}{24}\right)^{1/2}\frac{c}{d_{\mathrm{L}}}\left(\frac{GM_c}{c^3}\right)^{5/6} f_{\mathrm{GW}}^{-7/6}, \\ \simeq& 7 \times 10^{-20}\left(\frac{1\mathrm{Mpc}}{d_{\mathrm{L}}}\right)\left(\frac{m}{1M_\odot}\right)^{5/6} f_{\mathrm{GW}}^{-7/6}. \end{aligned} \tag{2.35}$$

Here, we assumed that the masses of the objects constituting the binary system were equal, $m1 = m2 = m$. Fig. 2.1 shows the spectra of gravitational wave amplitudes of chirp waves radiated by the binary object consisting of the 1.4 $M_\odot$ neutron star and the 1000 $M_\odot$ black hole, respectively. The symbol 'X' in the figure represents the ISCO frequency. In addition, each arrow on the spectrum shows the time it takes from that point to the merger.

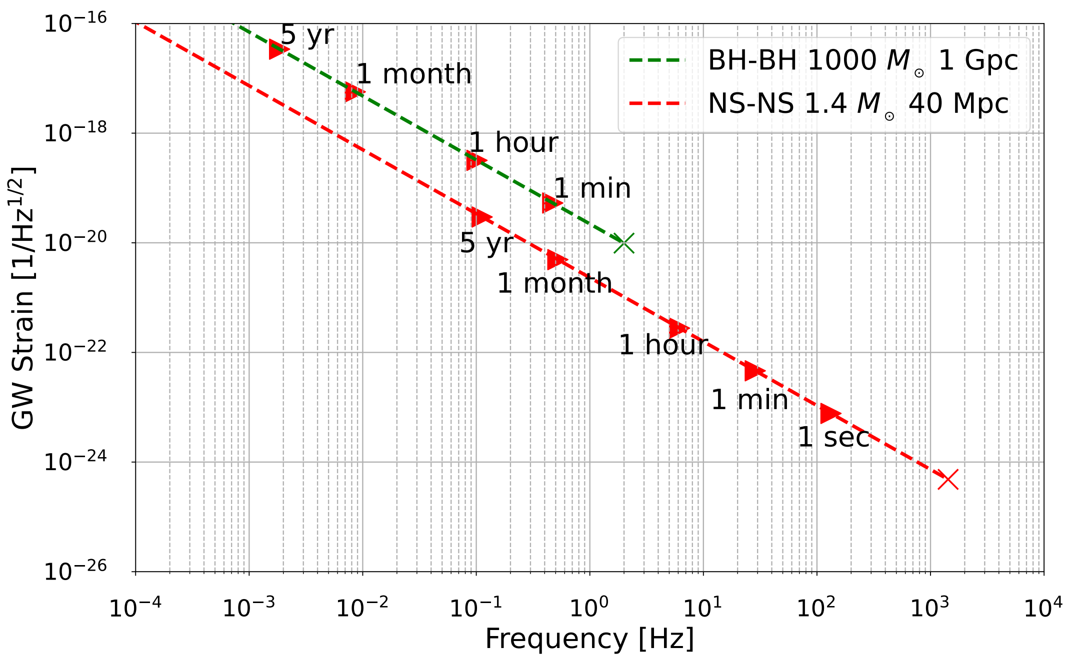

Figure 2.2: The gravitational wave strains from the binary stars with masses of $1000M_\odot$ and $1.4M_\odot$, located at a luminosity distance of 1 Gpc and 40 Mpc respectively. It can be seen that the frequency increases as the spiral evolves. The heavier binary star system radiates stronger gravitational waves and reaches the merger at an earlier stage of the inspiral.

2.3.2 Rotating neutron stars

Continuous waves are signals of constant frequency and amplitude that persist over long scales of a few years or longer. One promising source is rotating neutron stars with an asymmetry. The detection of continuous waves from rotating neutron stars allows us to study the properties of dense matter under conditions different from binary inspirals and mergers and to perform additional tests of theories of gravity. The amplitude of gravitational waves associated with the rotation of the neutron star can be expressed as follows [46]

$$\begin{aligned} h(f_{\mathrm{GW}}) &= \frac{4\pi^2 G}{c^4}\frac{I_{zz} f_{\mathrm{GW}}^2}{d_{\mathrm{L}}}\epsilon, \\ &\simeq 1.1\times 10^{-25}\left(\frac{\epsilon}{10^{-6}}\right)\left(\frac{I_{zz}}{10^{38}\ \mathrm{kg\ m^2}}\right)\left(\frac{10\mathrm{kpc}}{d_{\mathrm{L}}}\right)\left(\frac{f_{\mathrm{GW}}}{1\mathrm{kHz}}\right)^2, \end{aligned} \tag{2.36}$$

where I_{zz} is the moment of inertia around the rotational axis of the neutron star,ϵ is the ellipticity of the neutron star respectively. An upper limit of the continuous wave amplitude is given by the observation of the ground detectors. The current value is $h < 1.1\times 10^{-25}$ at 111.5 Hz [47].

2.3.3 Supernovae

Supernova explosions can be sources of gravitational waves if there is asymmetry. In the case of a Type Ia supernova caused by WD exceeding the Chandrasekhar limit due to mass accretion, gravitational waves of the order of $h \sim 10^{-22}$ at 1 Hz are expected at a distance of 10 kpc [48]. In addition, in the case of a Type II supernova caused by gravitational collapse, gravitational waves of the order of $h \sim 10^{-21}$ to 10^{-22} at 1 kHz are expected at a distance of 10 pc [44].

In addition, if a rotating remnant is produced after the explosion, it can be a source of the gravitational wave in a low-frequency band, around 0.1 Hz [49].

2.3.4 Primordial gravitational waves

In the early universe, electromagnetic waves are scattered and cannot travel straight ahead due to the high temperature plasma. Therefore, gravitational waves with strong transmissivity are the only way for direct observation of the early universe [8,9]. Such gravitational waves are called primordial gravitational waves (PGWs). For observing PGW, it is important to choose an observation frequency band where the foreground GW can be removed [24, 50, 51]. The amplitude spectral density of the PGW can be written as follow [46].

$$h(f_{\mathrm{GW}}) = \sqrt{\frac{3H_0^2 \Omega_{\mathrm{GW}}}{4\pi^2 f_{\mathrm{GW}}^3}}, \tag{2.37}$$

where $\Omega_{\rm GW}$ is the energy density of gravitational waves, with an upper limit of $\Omega_{\rm GW} \sim 10^{-16}$ based on the CMB observations [52] and H_0 is the Hubble constant.

The measurement of the spectral structure of the PGW provides very important information on various key physics, including thermal history of the universe after inflation, dark energy, and first order phase transition dynamics, and verification of the inflation theory [30–34].

Chapter 3
LASER INTERFEROMETRIC GRAVITATIONAL WAVE DETECTOR

This chapter summarizes gravitational wave detectors, focusing on the laser interferometric type. First, I provide an overview of gravitational wave detectors in Sect.3.1. Next, the basic properties of Michelson interferometers and Fabry-Perot detectors in Sect 3.2 and 3.3, which are the fundamental components of laser interferometer-type detectors, are summarized. Then, noise sources in gravitational wave detection is summarized in Sect.3.4. After that, I summarize the sensitivity of the major laser interferometric detectors in Sect.3.5. Finally, we compare the optical transponder scheme and the Fabry-Perot scheme, the major schemes for space laser interferometric detectors in Sect.3.6.

3.1 Overview of gravitational wave detector

The principles of direct detection of gravitational waves can mainly be divided into two methods.

· Measuring the mechanical oscillations induced by the acceleration of the test mass due to the gravitational waves.
· Measuring the variations in proper distance between the test masses due to the gravitational waves using photons or particles.

An example from the former is the resonant bar detector. This method has a high sensitivity near the mechanical resonance frequency of the test mass. It was used for the first gravitational wave detector [53]. Recently, there have been attempts to detect ultra-high-frequency gravitational waves using a small test mass and a superconducting sensor [54].

Methods that correspond to the latter include laser interferometric detectors, doppler tracking, and PTA. Laser interferometric detectors make a laser beam round-trip between the test masses and detect the variations in optical distance due to the gravitational waves by measuring the phase change of the laser beam. The ground-based detectors such as advanced LIGO [55], advanced Virgo [56] and KAGRA [57], as well as the future space-based detectors such as LISA [15], Taiji [16], TianQin [17], BBO [18], TianGO [19], B-DECIGO [22] and DECIGO [24] utilize this method. This principle is also applied to the Doppler tracking and PTA. The Doppler tracking measures the phase change of radio waves between the ground and a spacecraft. In PTA, which measures the change in the flicker period of pulsars due to gravitational waves. The typical baseline lengths and measurement bandwidths for each of these methods are listed in Table 3.1. This is related to, as derived in Eq. (2.19), a longer baseline length gives higher sensitivity to gravitational waves. On the other hand, as can be seen from the response of the detector, which will be derived later in Eq. (3.10) and Eq. (3.35), gravitational waves with a shorter period (i.e., higher frequency) than the photon round-trip time are less sensitive due to the canceling effect of the integration time.

Hereafter, we will focus on laser interferometric detectors. A laser interferometric detector is composed of a Michelson interferometer, which compares the phases of lasers propagating in two different paths (hereafter called arm), and/or a Fabry-Perot cavity, which makes the resonance of the laser between mirrors and gain the effective distance as introduced in Sect. 3.3.

The ground-based detectors such as LIGO are based on the Michelson interferometer. However, the optimum arm length for a simple Michelson interferometer, for example, for a 100 Hz gravitational wave, is about 750 km, which is not practical for construction on the Earth. Therefore, Fabry-Perot cavities are incorporated in each arm to obtain an effective length.

In the case of space detectors, it is possible to take sufficiently long arm lengths compared to the ground-based ones. For example, LISA has arms of about 2.5 million km without a cavity, optimized for gravitational waves in the 0.1-100 mHz band. In the case of DECIGO, the arm is optimized for the gravitational waves of 0.1-10 Hz by using an arm with a Fabry-Perot cavity of about 1000 km length. The reason for using cavities instead of longer baseline lengths is to prevent diffraction loss and reduce shot noise.

Table 3.1: Characteristics of various detectors

example	type	baseline length	frequency band
NANOgrav	PTA	$\sim 10^{15} - 10^{16}$ m	$\sim$ nHz
CASSINI	Doppler tracking	$\sim 10^{12}$ m	0.01-0.1 mHz
LISA	space laser interferometer	2.5×10^9 m	0.1-100 mHz
DECIGO	space laser interferometer	1×10^6 m	0.1-10 Hz
LIGO	laser interferometer	4×10^3 m	10-1000 Hz

3.2 Michelson interferometer

3.2.1 Fundamental operation of Michelson interferometer

A schematic view of the Michelson interferometer is shown in Fig. 3.1. Here, the vertical direction is set as the y-axis and the horizontal direction as the x-axis. The beam from the laser source is split into two optical paths by the BS (beam splitter) at the vertex. These beams are reflected by mirrors TMX (test mass X) and TMY (test mass Y) located in the x- and y-axis directions. The reflected beam recombine at the BS, and the interfered light is detected by a PD (Photo Detector). Assuming that the amplitude of the incident laser electric field is E_0 and the angular frequency is Ω, the incident electric field $E_{\rm in}$ can be written as

$$E_{\rm in} = E_0 e^{i\Omega t}. \tag{3.1}$$

In addition, putting that the phase shift of the electric field during the round trip of each arm is Φ_x and Φ_y, and that both the intensity reflectance and transmittance of BS are 0.5, the power of the laser light received by the PD, $P_{\rm PD}$, can be written as

$$\begin{aligned} P_{\rm PD} &= \left| \frac{1}{2} E_{\rm in} \mathrm{e}^{i(\Omega t - \Phi_x)} - \frac{1}{2} E_{\rm in} \mathrm{e}^{i(\Omega t - \Phi_y)} \right|^2 , \\ &= \frac{1}{2} P_{\rm in} \left(1 - \cos \Phi_-\right) , \end{aligned} \tag{3.2}$$

where $P_{\rm in} \equiv |E_{\rm in}|^2$ and $\Phi_- \equiv \Phi_x - \Phi_y$. Thus, the Michelson interferometer can convert the difference in the lengths of the two arms (i.e., the difference in phase) into light intensity. Gravitational waves produce tidal fluctuations as seen in Sect. (2.1). Thus, the Michelson interferometer can be utilized as a gravitational wave detector.

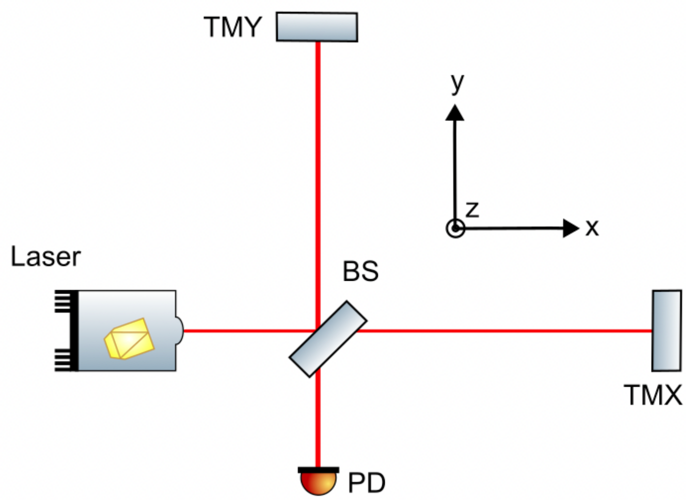

Figure 3.1: Schematic view of Michelson interferometer

3.2.2 Response of Michelson interferometer to gravitational wave

Let us consider the case where the + mode gravitational wave is incident on an interferometer in the xy plane from the z direction. First, the line element between BS and TMX is

$$\begin{aligned} ds^2 &= -(cdt)^2 + \{1 + h(t)\}dx^2, \\ &= 0. \end{aligned} \tag{3.3}$$

Note that $ds^2 = 0$ since the photon travels on a null geodesic. Now, let us assume the $dx/dt > 0$. Furthermore, the gravitational wave amplitude is small so that $1 \gg h(t)$, Eq. (3.3) can be written as

$$cdt\left\{1 - \frac{1}{2}h(t)\right\} \simeq dx. \tag{3.4}$$

By integrating Eq. (3.4) with round-trip time, it can be written as

$$\int_{t-\frac{2l_x}{c}}^{t} \left\{1 - \frac{1}{2}h\left(t'\right)\right\} dt' \simeq \frac{2l_x}{c}, \tag{3.5}$$

where l_x is the distance between TMX and BS. Therefore, the time $\varDelta t_x$ for photon round-trip in the X-arm can be written as

$$\varDelta t_x \simeq \frac{2l_x}{c} + \frac{1}{2}\int_{t-\frac{2l_x}{c}}^{t} h\left(t'\right)dt'. \tag{3.6}$$

The phase shift $\varPhi_x$ resulting in an X-arm round trip is the value of Eq. (3.6) multiplied by the laser angular frequency $\varOmega$. The phase shift in the light round-trip on the Y arm can be obtained in the same way, noting that the effect of the gravitational wave is the opposite of that on the X arm. By taking the difference between them, the differential change in the phase $\varPhi_-$ can be written as

$$\begin{aligned}\varPhi_- &= \varPhi_x - \varPhi_y \\ &= \frac{2\left(l_x - l_y\right)\varOmega}{c} + \varOmega\int_{t-\frac{2l}{c}}^{t} h\left(t'\right)dt',\end{aligned} \tag{3.7}$$

where l_y is the distance between BS and TMY similar to l_x, and we assumed $l_x \simeq l_y \simeq l$. The second term in Eq. (3.7) represents the effect of the phase shift due to the gravitational waves. The first term is simply the component resulting from the difference in arm lengths.

The expression of the Fourier transform of the gravitational wave amplitude is,

$$h(t) = \int_{-\infty}^{\infty} h(\omega)\mathrm{e}^{i\omega t}d\omega. \tag{3.8}$$

By plugging the second term of Eq. (3.7), the phase shift induced by gravitational waves can be written as

$$\begin{aligned}\varDelta\varPhi(t)_{GW} &= \varOmega\int_{t-\frac{2l}{c}}^{t}\int_{-\infty}^{\infty} h(\omega)\mathrm{e}^{i\omega t}d\omega dt', \\ &= \int_{-\infty}^{\infty}\frac{2\varOmega}{\omega}\sin\left(\frac{\omega l}{c}\right)\mathrm{e}^{\frac{-i\omega l}{c}}h(\omega)\mathrm{e}^{i\omega t}d\omega, \\ &= \int_{-\infty}^{\infty}\alpha_{\mathrm{MI}}H_{\mathrm{MI}}(\omega)h(\omega)\mathrm{e}^{i\omega t}d\omega,\end{aligned} \tag{3.9}$$

where

$$H_{\mathrm{MI}}(\omega) = \frac{c}{\omega l}\sin\left(\frac{\omega l}{c}\right)\mathrm{e}^{\frac{-i\omega l}{c}}, \tag{3.10}$$

and

$$\alpha_{\mathrm{MI}} = \frac{2\varOmega l}{c}, \tag{3.11}$$

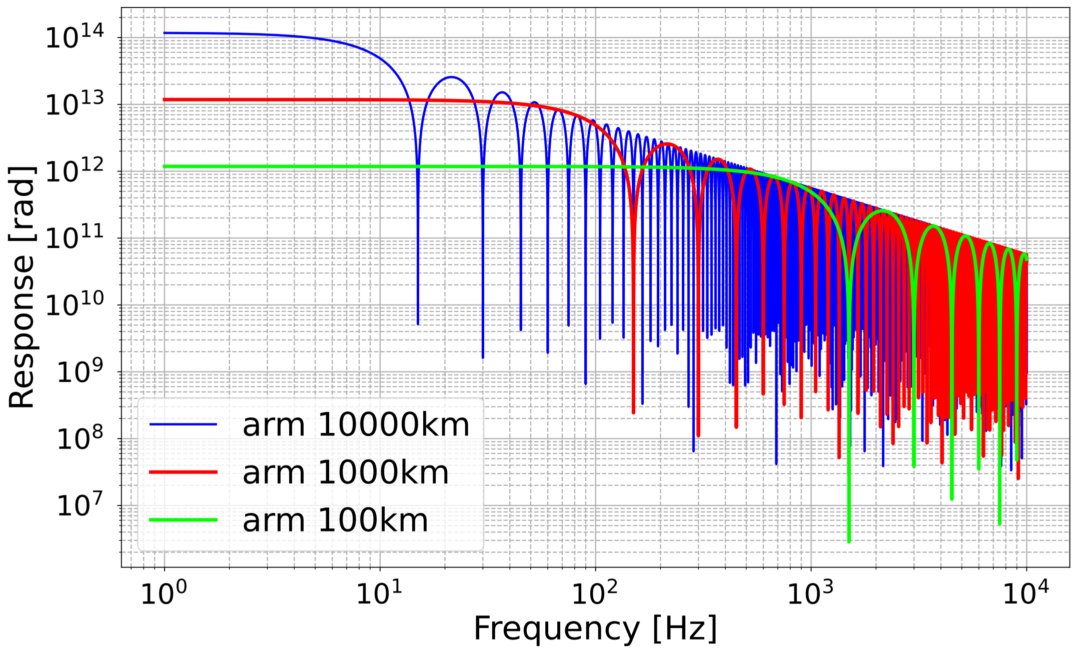

Figure 3.2: Frequency dependence of Michelson interferometer response at a few selected arm lengths

represents the normalized response function of the Michelson interferometer to the gravitational wave and normalized constant. Fig. 3.2 shows the Michelson response plotted as a function of frequency for baseline lengths of 100 km, 1000 km, and 10000 km, and Fig. 3.3 shows the plot as a function of length for gravitational waves of 0.1 Hz, 1 Hz, and 10 Hz. The effect of the gravitational wave is maximized when the round trip time of the light is equal to the half period of the gravitational wave, while the canceling effect begins when the round trip time exceeds the half period. When the round-trip time is equal to the gravitational wave period, it means that the light cannot detect changes caused by gravitational waves. The optimal baseline length for gravitational wave frequency, at 10 Hz, is about 7500 km. This optimum baseline length becomes longer at lower frequencies. The Fabry-Perot cavity introduced in Sect. 3.3 allows for a longer effective baseline length. However, as introduced in Sect. 3.4.1, the effect of seismic noise becomes significant in the low-frequency band on the ground.

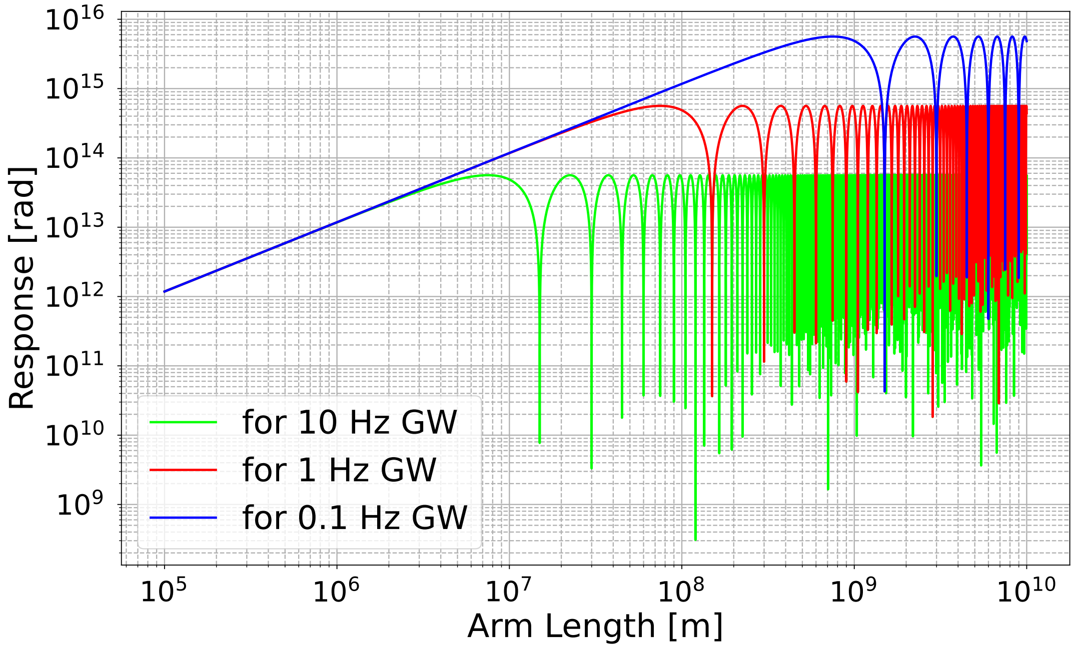

Figure 3.3: Arm length dependence of Michelson interferometer response at a few selected frequency points

3.3 Favry-Perot cavity

The mechanism that makes the resonance of the laser between the mirrors is called a cavity. In particular, a cavity with mirrors arranged in a straight line is called a Fabry-Perot cavity. The cavity can achieve an extended optical path length through repeated round-trips of light. Consequently, it can achieve a larger phase shift (i.e., higher sensitivity) to gravitational waves than a simple Michelson interferometer.

Because of this property, cavities are incorporated into ground-based detectors with limited space. In addition, the cavities can be utilized in space detectors to enhance sensitivity in cases where they can receive enough light.

In this section, the basic properties of the Fabry-Perot cavity are derived, and then the frequency response for the incident laser and gravitational wave are derived. Finally, we summarize the Pound Drever Hall scheme for obtaining the error signal to the cavity resonance.

3.3.1 Basic properties of Fabry-Perot cavity

Let us consider a Fabry-Perot cavity with length L, consisting of mirrors ITM (input test mass) and ETM (end test mass) with amplitude reflectance and transmittance r_i, t_i, and r_e, t_e, respectively, as shown in Fig. 3.4. In addition, let t be the amplitude transmittance (corresponding to the loss) inside the cavity. From the viewpoint of energy conservation, it is assumed that the phase is inverted when light is reflected on the outer surface of the mirror (the side with the minus sign in the figure).

The light incident to the cavity is repeatedly reflected by the mirror in part and transmitted in the rest. As a result, the reflected electric field E_r, the internal electric field E_c, and the transmitted electric field E_t of the cavity can be expressed as an addition of the electric fields as be shown in Fig. 3.4. The reflected and transmitted electric fields relative to the incident electric field (i.e., cavity reflectance $r_\mathrm{cav}(\Phi)$ and transmission $t_\mathrm{cav}(\Phi)$) can be written as

$$\begin{aligned} r_\mathrm{cav}(\Phi) &\equiv \frac{E_\mathrm{r}}{E_\mathrm{in}}, \\ &= -r_\mathrm{i} + t_\mathrm{i}^2 r_\mathrm{e} t^2 \mathrm{e}^{-i\Phi} \sum_{n=0}^{\infty} \left(r_\mathrm{i} r_\mathrm{e} t^2 \mathrm{e}^{-i\Phi} \right)^n, \\ &= -r_\mathrm{i} + \frac{t_\mathrm{i}^2 r_\mathrm{e} t^2 \mathrm{e}^{-i\Phi}}{1 - r_\mathrm{i} r_\mathrm{e} t^2 \mathrm{e}^{-i\Phi}}, \end{aligned} \tag{3.12}$$

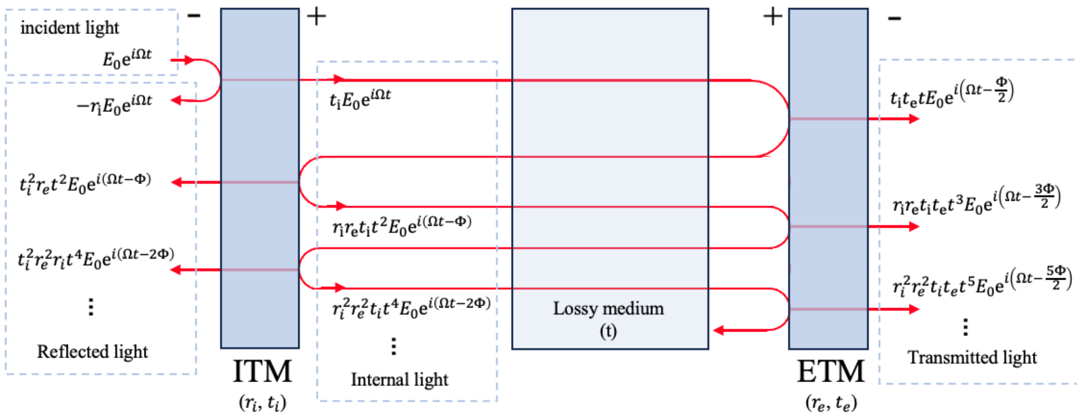

Figure 3.4: The electric field inside the cavity

$$
\begin{aligned}
t_{\text{cav}}(\Phi) &\equiv \frac{E_{\text{t}}}{E_{\text{in}}}, \\
\frac{E_{\text{t}}}{E_{\text{in}}} &= t_{\text{i}} t_{\text{e}} t \mathrm{e}^{\frac{-i\Phi}{2}} \sum_{n=0}^{\infty} \left(r_{\text{i}} r_{\text{e}} t^2 \mathrm{e}^{\frac{-i\Phi}{2}} \right)^n, \\
&= \frac{t_{\text{i}} t_{\text{e}} t \mathrm{e}^{\frac{-i\Phi}{2}}}{1 - r_{\text{i}} r_{\text{e}} t^2 \mathrm{e}^{-i\Phi}},
\end{aligned}
\tag{3.13}
$$

where Φ is the phase shift that results when the light round-trip through the cavity. This value is obtained by multiplying the angular frequency of light, Ω, by the round-trip time of $2L/c$. Similarly, the internal electric field can be written as

$$
\begin{aligned}
\frac{E_{\text{c}}}{E_{\text{in}}} &= t_{\text{i}} \sum_{n=0}^{\infty} \left(r_{\text{i}} r_{\text{e}} t^2 \mathrm{e}^{-i\Phi} \right)^n, \\
&= \frac{t_{\text{i}}}{1 - r_{\text{i}} r_{\text{e}} t^2 \mathrm{e}^{-i\Phi}}.
\end{aligned}
\tag{3.14}
$$

The amplitude and phase of reflected and transmitted light relative to incident light (i.e., cavity reflectance and transmittance) are shown in Figs. 3.5 and 3.6. Here we assumed $t_{\text{i}}^2 = t_{\text{e}}^2 = 0.001, t = 0$. The point where the transmitted light is maximum and the reflected light is minimum is called the resonance. At the resonance point, since the cavity length is an integer multiple of the half-wavelength of the laser, the phase is matched with the incident light. Therefore, the phase change of reflected and transmitted light is zero. In the region near the resonance, since the light circulates inside the cavity many times, it shows

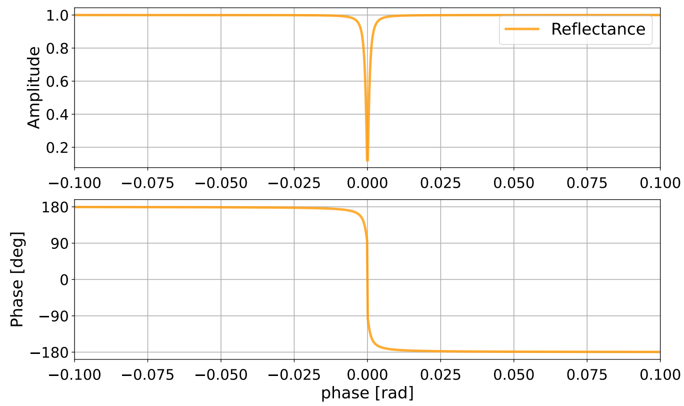

Figure 3.5: The reflectance of the cavity as a function of the deviation from resonance. The horizontal axis represents the deviation from the resonance.

a steep phase change for the deviation from the resonance. This slope becomes steeper as the number of round trips of the light is larger. This property makes the cavity a highly sensitive sensor for mirror displacement and incident laser frequency. In the regions where the deviation from the resonance is large, the light does not enter the cavity, and the cavity behaves like a simple mirror, and the phase is almost unchanged.

In addition, by taking the square of the absolute value of Eqs. (3.12) and (3.14), the intensity normalized by the incident light intensity for each light can be written as

$$\left|\frac{E_\mathrm{r}}{E_\mathrm{in}}\right|^2 = \frac{\left(r_\mathrm{i} - r_\mathrm{e}t^2\right)^2 + 4r_\mathrm{i}r_\mathrm{e}t^2\sin^2\frac{\Phi}{2}}{\left(1 - r_\mathrm{i}r_\mathrm{e}t^2\right)^2 + 4r_\mathrm{i}r_\mathrm{e}t^2\sin^2\frac{\Phi}{2}} \tag{3.15}$$

$$\left|\frac{E_\mathrm{c}}{E_\mathrm{in}}\right|^2 = \frac{t_\mathrm{i}^2}{\left(1 - r_\mathrm{i}r_\mathrm{e}t^2\right)^2 + 4r_\mathrm{i}r_\mathrm{e}t^2\sin^2\frac{\Phi}{2}} \tag{3.16}$$

For the transmitted light intensity, the value can be obtain by multiplying $t_\mathrm{e}^2t^2$ to Eq. (3.16).

Resonance occurs when the phase Φ fulfills $\Phi = 2n\pi$ $(\mathrm{n}: \text{ integer})$, so it repeats at a regular interval. This resonance interval is called FSR (Free Spectral Range) and FSR $= 2\pi$. Here, let FSR expressed in frequency be ν_FSR, it can be represent as

$$\nu_\mathrm{FSR} = \frac{c}{2L}, \tag{3.17}$$

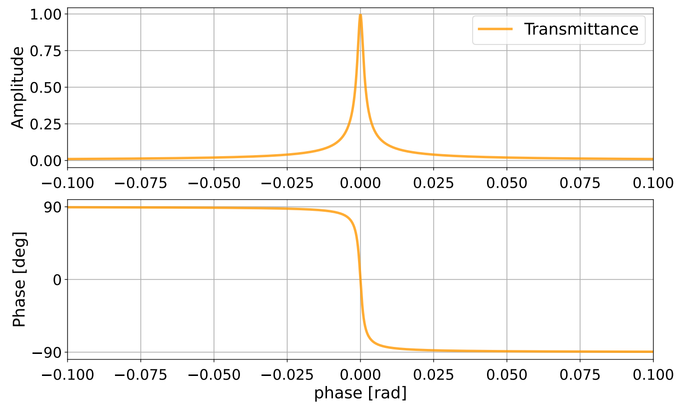

Figure 3.6: The transmittance of the cavity as a function of the deviation from resonance. The horizontal axis represents the deviation from the resonance.

since

$$\begin{aligned}\mathrm{FSR} &= 2\pi, \\ &= \frac{2L}{c} 2\pi \nu_{\mathrm{FSR}}.\end{aligned} \tag{3.18}$$

By differentiating both sides of Eq. (3.17) by the cavity length L, we can obtain the relation of

$$\frac{\delta \nu}{\nu} = -\frac{\delta L}{L}. \tag{3.19}$$

This result shows that the frequency variation is equivalent to the resonator length variation for the cavity.

Now, let us consider the phase $\Phi_{1/2}$ in which the internal light power becomes half of the power at the resonance as follows,

$$\frac{1}{2}\frac{t_{\mathrm{i}}^2}{(1 - r_{\mathrm{i}} r_{\mathrm{e}} t^2)^2} = \frac{t_{\mathrm{i}}^2}{(1 - r_{\mathrm{i}} r_{\mathrm{e}} t^2)^2 + 4 r_{\mathrm{i}} r_{\mathrm{e}} t^2 \sin^2 \frac{\Phi_{1/2}}{2}}. \tag{3.20}$$

Here, we used the expression Eq. (3.16) for the internal light intensity of the cavity. Assuming that the resonance is sharp and $\Phi_{1/2} \gg 1$,then $\sin^{-1} \Phi_{1/2} \simeq \Phi_{1/2}$, thus $\Phi_{1/2}$ can be represent as

$$\Phi_{1/2} \simeq \frac{1 - r_{\mathrm{i}} r_2 t^2}{t\sqrt{r_{\mathrm{i}} r_2}}. \tag{3.21}$$

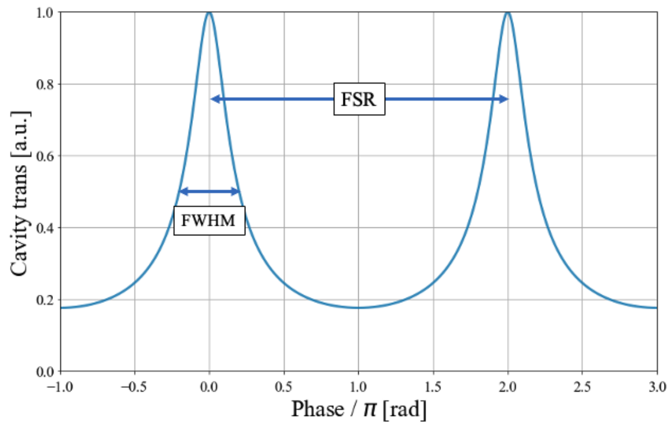

Figure 3.7: Relation between FWHM and FSR in the intensity of cavity transmitted light

By putting the frequency equivalent of $\varPhi_{1/2}$ as $\nu_{1/2}$, it can be written as

$$\nu_{1/2} = \frac{c}{4\pi L}\frac{1 - r_\mathrm{i} r_\mathrm{e} t^2}{t\sqrt{r_\mathrm{i} r_\mathrm{e}}}, \tag{3.22}$$

since

$$\varPhi_{1/2} = 2\pi\frac{2L}{c}\nu_{1/2}. \tag{3.23}$$

The full width at half maximum (FWHM) is defined as twice this value, and expressed as

$$\mathrm{FWHM} \equiv 2\nu_{1/2} = \frac{c}{2\pi L}\frac{1 - r_\mathrm{i} r_\mathrm{e} t^2}{t\sqrt{r_\mathrm{i} r_\mathrm{e}}}. \tag{3.24}$$

The relation between FSR and FWHM is shown in Fig. 3.7. The sharpness of the resonance of the cavity is characterized by finesse $\mathcal{F}$ which is defined as the ratio of the FSR and the full width at half maximum,

$$\begin{aligned} \mathcal{F} &\equiv \frac{\mathrm{FSR}}{\mathrm{FWHM}}, \\ &= \frac{\pi t\sqrt{r_\mathrm{i} r_\mathrm{e}}}{1 - r_\mathrm{i} r_\mathrm{e} t^2}. \end{aligned} \tag{3.25}$$

3.3.2 Response of Favry-Perot cavity to laser frequency

Let us consider the light E_{in} with phase deviation $\delta p(t)$ incident to the cavity. Assuming that the amplitude is E_0 and the angular frequency is $\mathit{\Omega}$, E_{in} can be written as

$$\begin{aligned} E_{\mathrm{in}} &= E_0 \mathrm{e}^{i\{\mathit{\Omega} t+\delta p(t)\}}, \\ &\simeq E_0 \mathrm{e}^{i\mathit{\Omega} t}\{1+i\delta p(t)\}, \end{aligned} \tag{3.26}$$

with $\delta p(t) \ll 1$. At this time, E_{in} can be represented as

$$E_{\mathrm{in}} = E_0 \mathrm{e}^{i\mathit{\Omega} t} + iE_0 \int_{-\infty}^{\infty} \delta p(\omega) \mathrm{e}^{i(\mathit{\Omega}+\omega)t} d\omega. \tag{3.27}$$

Here we used the inverse Fourier transform

$$\delta p(t) = \int_{-\infty}^{\infty} \delta p(\omega) \mathrm{e}^{i\omega t} d\omega. \tag{3.28}$$

Since the cavity shows different reflectance for different frequency components from Eq. (3.12), the reflected electric field E_r can be represented as

$$\begin{aligned} E_{\mathrm{r}} &= E_0 \mathrm{e}^{i\mathit{\Omega} t} r_{\mathrm{cav}}(\mathit{\Phi}) + iE_0 \int_{-\infty}^{\infty} \delta p(\omega) r_{\mathrm{cav}}\left(\mathit{\Phi}_\omega\right) \mathrm{e}^{i(\mathit{\Omega}+\omega)t} d\omega, \\ &= E_0 \mathrm{e}^{i\mathit{\Omega} t} r_{\mathrm{cav}}(\mathit{\Phi}) \left(1 + i\int_{-\infty}^{\infty} \delta p(\omega) \mathrm{e}^{i\omega t} d\omega\right) - iE_0 \mathrm{e}^{i\mathit{\Omega} t} r_{\mathrm{cav}}(\mathit{\Phi}) \int_{-\infty}^{\infty} \delta p(\omega) \mathrm{e}^{i\omega t} d\omega, \\ &= E_0 e^{i\mathit{\Omega} t} r_{\mathrm{cav}}(\mathit{\Phi}) \{1 + i\delta p(t)\} + iE_0 \mathrm{e}^{i\mathit{\Omega} t} \int_{-\infty}^{\infty} \delta p(\omega) \mathrm{e}^{i\omega t} \omega \left\{r_{\mathrm{cav}}(\mathit{\Phi}_m) - r_{\mathrm{cav}}(\mathit{\Phi})\right\}, \\ &\simeq E_{\mathrm{in}} \left\{ r_{\mathrm{cav}}(\mathit{\Phi}) + \int_{-\infty}^{\infty} \delta p(\omega) \mathrm{e}^{i\omega t} d\omega \frac{2r_{\mathrm{e}} t_{\mathrm{i}}^2 t^2 \mathrm{e}^{-i(\mathit{\Phi}+\gamma)} \sin\gamma}{\left\{1 - r_{\mathrm{i}} r_{\mathrm{e}} t^2 \mathrm{e}^{-i(\mathit{\Phi}+2\gamma)}\right\}\left(1 - r_{\mathrm{i}} r_{\mathrm{e}} t^2 \mathrm{e}^{-i\mathit{\Phi}}\right)} \right\}, \end{aligned} \tag{3.29}$$

with

$$\frac{2L\left(\mathit{\Omega}+\omega\right)}{c} \equiv \mathit{\Phi} + 2\gamma. \tag{3.30}$$

When the cavity is in resonance condition or $\Phi = 2\pi n$ is satisfied, Eq. (3.29) becomes

$$\begin{aligned} E_{\mathrm{r}} &\simeq E_{\mathrm{in}}\left\{r_{\mathrm{cav\_reso}} + \int_{-\infty}^{\infty} \delta p(\omega)\mathrm{e}^{i\omega t}d\omega \frac{2r_{\mathrm{e}}t_{\mathrm{i}}^2t^2\mathrm{e}^{-i\gamma}\sin\gamma}{(1-r_{\mathrm{i}}r_{\mathrm{e}}t^2\mathrm{e}^{-2i\gamma})(1-r_{\mathrm{i}}r_{\mathrm{e}}t^2)}\right\}, \\ &= E_{\mathrm{in}}\left\{r_{\mathrm{cav\_reso}} - i\int_{-\infty}^{\infty} \frac{2\pi\delta\nu(\omega)}{\omega}\mathrm{e}^{i\omega t}d\omega \frac{2r_{\mathrm{e}}t_{\mathrm{i}}^2t^2\mathrm{e}^{-i\gamma}\sin\gamma}{(1-r_{\mathrm{i}}r_{\mathrm{e}}t^2\mathrm{e}^{-2i\gamma})(1-r_{\mathrm{i}}r_{\mathrm{e}}t^2)}\right\}, \\ &= E_{\mathrm{in}}\left\{r_{\mathrm{cav\_reso}} - i\alpha_{\mathrm{FP}}^{(\nu)}\int_{-\infty}^{\infty} H_{\mathrm{FP}}(\omega)\delta\nu(\omega)\mathrm{e}^{i\omega t}d\omega\right\}. \end{aligned} \tag{3.31}$$

Here, we used the fact that the frequency deviation $\delta\nu(\omega)$ is the time derivative of the phase noise and can be written as

$$\delta p(\omega) = \frac{2\pi\delta\nu(\omega)}{i\omega}, \tag{3.32}$$

$r_{\mathrm{cav\_reso}}$ is the cavity reflectance at resonance,

$$r_{\mathrm{cav\_reso}} = \frac{-r_{\mathrm{i}} + r_{\mathrm{e}}t^2(r_{\mathrm{i}}^2 + t_{\mathrm{i}}^2)}{1 - r_{\mathrm{i}}r_{\mathrm{e}}}, \tag{3.33}$$

$\alpha_{\mathrm{FP}}^{(\nu)}$ is a normalized constant,

$$\alpha_{\mathrm{FP}}^{(\nu)} = \frac{r_{\mathrm{e}}t_{\mathrm{i}}^2t^2}{(1-r_{\mathrm{i}}r_{\mathrm{e}}t^2)^2}\frac{4\pi L}{c}, \tag{3.34}$$

and $H_{\mathrm{FP}}^{(\nu)}(\omega)$ in the final term of Eq. (3.31) is the normalized frequency response of the cavity,

$$H_{\mathrm{FP}}(\omega) = (1 - r_{\mathrm{i}}r_{\mathrm{e}}t^2)\frac{c}{L}\frac{1}{\omega}\frac{\mathrm{e}^{-i\gamma}\sin\gamma}{1 - r_{\mathrm{i}}r_{\mathrm{e}}t^2\mathrm{e}^{-2i\gamma}}. \tag{3.35}$$

By taking the absolute value of Eq. (3.35),

$$\begin{aligned} |H_{\mathrm{FP}}(\omega)| &\simeq \frac{1}{\sqrt{1 + \frac{4r_{\mathrm{i}}r_{\mathrm{e}}t^2}{(1-r_{\mathrm{i}}r_{\mathrm{e}}t^2)^2}\left(\frac{L}{c}\right)^2\omega^2}}, \\ &= \frac{1}{\sqrt{1+\tau^2\omega^2}}, \end{aligned} \tag{3.36}$$

where τ is the average storage time for photons and can be written as

$$\tau^2 = \frac{4r_{\mathrm{i}}r_{\mathrm{e}}t^2}{(1-r_{\mathrm{i}}r_{\mathrm{e}}t^2)^2}\left(\frac{L}{c}\right)^2. \tag{3.37}$$

Here I assumed a long-wavelength approximation where the laser frequency variation time is sufficiently slower than the travel time of the light in the cavity(i.e., $\frac{L}{c} \ll \frac{1}{\omega}$). As can be seen from Eq. (3.36), the frequency response of the cavity shows a response similar to a low-pass. The cutoff frequency of the low-pass ν_c can be represented as

$$\nu_c = \frac{1}{2\pi\tau} = \frac{1}{\mathcal{F}}\frac{c}{4L}. \tag{3.38}$$

Additionally, from Eqs. (3.37) and (3.25), the average round-trip number of light within the cavity, denoted as N, can be expressed in terms of finesse as

$$N = \frac{\tau c}{L} = \frac{2\mathcal{F}}{\pi}. \tag{3.39}$$

The frequency response of the cavity given by Eq. (3.35) and the transfer function of a single pole with cutoff frequency ν_c are shown in Fig. 3.8. The figure shows that the cavity response deviates from the single-pole model around 150 Hz, the FSR frequency, and its constant multiplier frequency. However, the single-pole model can be approximated well in the frequency range below FSR.

Physically, this response means that there is a cancellation effect for fluctuations that are roughly faster than the storage time of the cavity. Unlike the case of the Michelson interferometer, each photon makes multiple round-trips, and the round-trip numbers are different, so the response is not zero even at frequencies where the disturbance period is equal to the round-trip time of the light. However, at the FSR frequency, any round trip number of photons makes an integer number of round trips so that the response is zero.

3.3.3 Response of Favry-Perot cavity to gravitational wave

In this section, we consider the response of cavities to the gravitational waves. For the reflected light from the cavity, rewrite the right-hand side of Eq. (3.12) to include the time $\mathit{\Delta} t_n$ for the light to make the n round trips in the cavity,

$$\frac{E_{\mathrm{r}}}{E_{\mathrm{in}}} = -r_{\mathrm{i}} + t_{\mathrm{e}}^2 t^2 r_{\mathrm{e}} \sum_{n=1}^{\infty} \left(r_{\mathrm{i}} r_{\mathrm{e}} t^2\right)^{n-1} \mathrm{e}^{-i\mathit{\Delta} t_n \mathit{\Omega}}, \tag{3.40}$$

where $\mathit{\Delta} t_n$ can be represented by including the effect of the gravitational wave similar to Eq. (3.6),

$$\mathit{\Delta} t_n \simeq \frac{2Ln}{c} + \frac{1}{2}\int_{t-\frac{2Ln}{c}}^{t} h\left(t'\right) dt'. \tag{3.41}$$

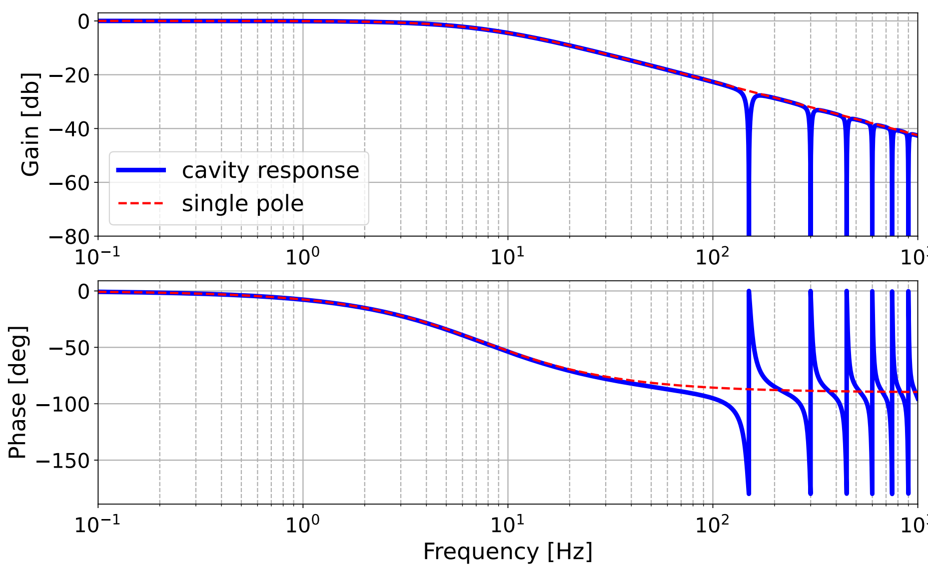

Figure 3.8: Normalized frequency response of the cavity and its single-pole approximation. Cavity parameters are adopted $L = 1000$ km and $\mathcal{F} = 10$.

By Fourier transforming the gravitational wave amplitude,

$$\begin{aligned} \Delta t_n &\simeq \frac{2Ln}{c} + \frac{1}{2}\int_{t-\frac{2Ln}{c}}^{t}\int_{-\infty}^{\infty} h(\omega)\mathrm{e}^{i\omega t'}dt'd\omega, \\ &= \frac{2Ln}{c} + \frac{1}{2i\omega}\int_{-\infty}^{\infty}\mathrm{e}^{i\omega t}\left(1-\mathrm{e}^{-i\omega\frac{2Ln}{c}}\right)h(\omega)d\omega. \end{aligned} \tag{3.42}$$

By plugging Eq. (3.40), Eq. (3.42) can be written as

$$\begin{aligned} \frac{E_\mathrm{r}}{E_\mathrm{in}} =& -r_\mathrm{i} \\ &+t_\mathrm{i}^2 r_\mathrm{e} t^2 \sum_{n=1}^{\infty}\left(r_\mathrm{i}r_\mathrm{e}t^2\right)^{n-1}\exp\left[-i\Omega\left\{\frac{2Ln}{c}+\frac{1}{2i\omega}\int_{-\infty}^{\infty}\mathrm{e}^{i\omega t}\left(1-\mathrm{e}^{-i\omega\frac{2Ln}{c}}\right)h(\omega)d\omega\right\}\right]. \end{aligned} \tag{3.43}$$

By expanding the exp part to the first order of $h(\omega)$ with the gravitational wave amplitude as $|h(\omega)| \ll 1$, Eq. (3.43) can be written as

$$\begin{aligned} \frac{E_\mathrm{r}}{E_\mathrm{in}} &\simeq r_\mathrm{i} + t_\mathrm{e}^2 r_\mathrm{e} t^2 \sum_{n=1}^{\infty}\left(r_\mathrm{i}r_\mathrm{e}t^2\right)^{n-1}\mathrm{e}^{-i\Omega\frac{2Ln}{c}}\left\{1-\frac{\Omega}{2\omega}\int_{-\infty}^{\infty}\mathrm{e}^{i\omega t}\left(1-\mathrm{e}^{-i\omega\frac{2Ln}{c}}\right)h(\omega)d\omega\right\}, \\ &= -r_\mathrm{i} + \frac{t_\mathrm{e}^2 r_\mathrm{e} t^2}{1-r_\mathrm{i}r_\mathrm{e}t^2\mathrm{e}^{-i\Omega\frac{2L}{c}}} \\ &\quad - t_\mathrm{e}^2 r_\mathrm{e} t^2\int_{-\infty}^{\infty}\frac{\Omega}{2\omega}\left(\frac{\mathrm{e}^{-i\Omega\frac{2L}{c}}}{1-r_\mathrm{i}r_\mathrm{e}t^2\mathrm{e}^{-i\Omega\frac{2L}{c}}} - \frac{\mathrm{e}^{-i\Omega\frac{2L}{c}}\mathrm{e}^{-i\omega\frac{2L}{c}}}{1-r_\mathrm{i}r_\mathrm{e}t^2\mathrm{e}^{-i\omega\frac{2L}{c}}\mathrm{e}^{-i\Omega\frac{2L}{c}}}\right)h(\omega)\mathrm{e}^{i\omega t}d\omega, \\ &= -r_\mathrm{i} + \frac{t_\mathrm{e}^2 r_\mathrm{e} t^2}{1-r_\mathrm{i}r_\mathrm{e}t^2\mathrm{e}^{-i\Omega\frac{2L}{c}}} \\ &\quad - \frac{t_\mathrm{e}^2 r_\mathrm{e} t^2}{1-r_\mathrm{i}r_\mathrm{e}t^2\mathrm{e}^{-i\Omega\frac{2L}{c}}}\int_{-\infty}^{\infty}\frac{\Omega}{2\omega}\frac{\mathrm{e}^{-i\Omega\frac{2L}{c}}\left(1-\mathrm{e}^{-i\omega\frac{2L}{c}}\right)}{1-r_\mathrm{i}r_\mathrm{e}t^2\mathrm{e}^{-i\omega\frac{2L}{c}}\mathrm{e}^{-i\Omega\frac{2L}{c}}}h(\omega)\mathrm{e}^{i\omega t}d\omega. \end{aligned} \tag{3.44}$$

Assuming resonance condition $\frac{2L}{c}\Omega = 2\pi n$, Eq. (3.44) can be written as

$$\begin{aligned} \frac{E_r}{E_\mathrm{in}} &= \frac{-r_\mathrm{i}+\left(r_\mathrm{i}^2+t_\mathrm{e}^2\right)r_\mathrm{e}t^2}{1-r_\mathrm{i}r_\mathrm{e}t^2}\left(1-\frac{t_\mathrm{e}^2 r_\mathrm{e}t^2}{-r_\mathrm{i}+\left(r_\mathrm{i}^2+t_\mathrm{e}^2\right)r_\mathrm{e}t^2}\int_{-\infty}^{\infty}\frac{\Omega}{\omega}\frac{\mathrm{e}^{-i\omega\frac{L}{c}}i\sin\left(\omega\frac{L}{c}\right)}{1-r_\mathrm{i}r_\mathrm{e}t^2\mathrm{e}^{-i\omega 2L}}h(\omega)\mathrm{e}^{i\omega t}d\omega\right), \\ &= \frac{-r_\mathrm{i}+\left(r_\mathrm{i}^2+t_\mathrm{e}^2\right)r_\mathrm{e}t^2}{1-r_\mathrm{i}r_\mathrm{e}t^2}\left(1-i\alpha_\mathrm{FP}^{(\mathrm{GW})}\int_{-\infty}^{\infty}H_\mathrm{FP}(\omega)h(\omega)\mathrm{e}^{i\omega t}d\omega\right), \end{aligned} \tag{3.45}$$

where $\alpha_{\mathrm{FP}}^{(\mathrm{GW})}(\omega)$ is the normalized constant,

$$\begin{aligned}\alpha_{\mathrm{FP}}^{(\mathrm{GW})}(\omega) &= \frac{t_{\mathrm{e}}^2 r_{\mathrm{e}} t^2}{-r_{\mathrm{i}} + \left(r_{\mathrm{i}}^2 + t_{\mathrm{e}}^2\right) r_{\mathrm{e}} t^2} \frac{\Omega L}{c} \frac{1}{1 - r_{\mathrm{i}} r_{\mathrm{e}} t^2}, \\ &\simeq \frac{t_{\mathrm{e}}^2 r_{\mathrm{e}} t^2}{-r_{\mathrm{i}} + \left(r_{\mathrm{i}}^2 + t_{\mathrm{e}}^2\right) r_{\mathrm{e}} t^2} \frac{\Omega L \mathcal{F}}{c\pi}.\end{aligned} \tag{3.46}$$

The above result shows that the Fabry-Perot cavity has a similar frequency response to gravitational waves as the frequency deviation.

The response of the Fabry-Perot cavity to the gravitational wave given by Eq. (3.46) is shown in Fig. 3.9. For comparison, the response of the Michelson interferometer with the same length and the one with the length NL as the effective length considering the number of cavity round trips are also shown. It can be seen that the Fabry-Perot cavity is half as sensitive as the actual long Michelson interferometer. This is because a single cavity was considered, as compared to Michelson, which has two arms. In the case of the FPMI (Fabry-Perot Michelson interferometer), which incorporates a Fabry-Perot cavity in the Michelson interferometer arm, the sensitivity in the DC band is perfectly consistent with the long Michelson interferometer. The cavity parameters are from DECIGO and the finesse is about 10 [24].

3.3.4 Pound Drever Hall scheme

As described in the previous sections, to use the cavity for gravitational wave detection, it is necessary to keep the cavity under the resonant condition. In order to control the cavity resonant condition, it is necessary to obtain the error signal corresponding to the deviation of the cavity about the resonance. In this section, we summarize the PDH (Pound Drever Hall) scheme [58], which is known as a method for obtaining the error signal.

Figure 3.10 shows the layout of the PDH scheme. The incident light passes through the EOM (Eectro-Optic Modulator). EOM is a component that changes its refractive index with voltage applied across it and can modulate the phase of light. Let the electric field of the light source be $E_0 \mathrm{e}^{i\Omega t}$ and the angular frequency of the modulation signal be Ω_{m}, the electric field of the incident light

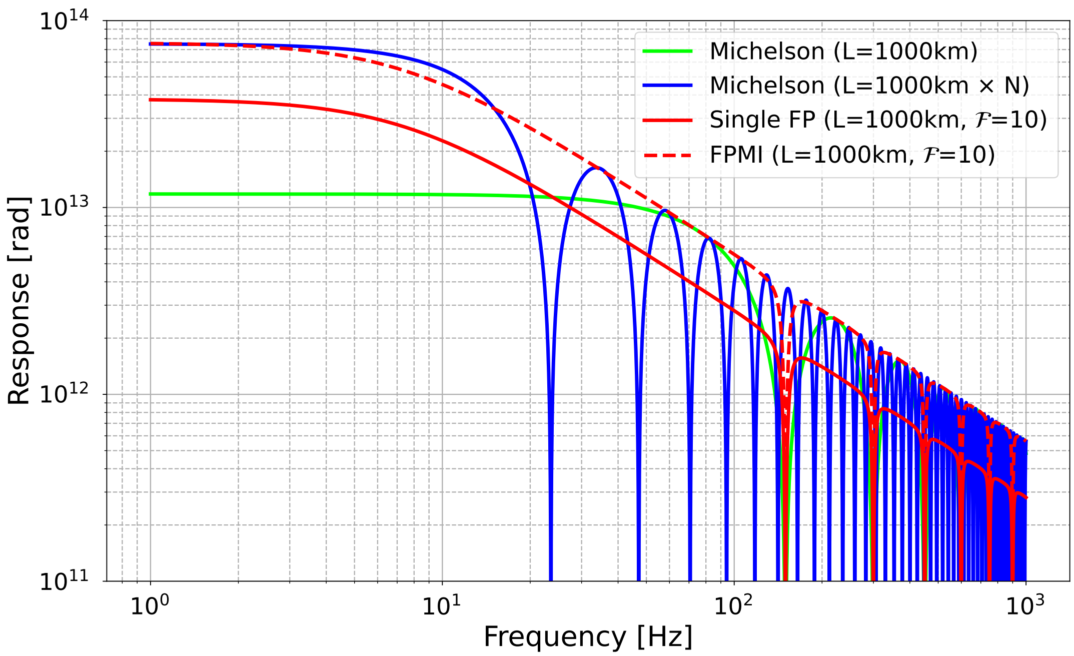

Figure 3.9: Response of Fabry-Perot Cavity to the gravitational wave. The horizontal axis is the frequency of the gravitational waves.

to the cavity, E_{in} can be written as

$$\begin{aligned} E_{\mathrm{in}} &= E_0 \mathrm{e}^{i(\Omega_0+\beta\sin\Omega_{\mathrm{m}})t}, \\ &= E_0 \sum_{-\infty}^{\infty} \mathrm{J}_n(\beta) \mathrm{e}^{i(\Omega_0+\Omega_{\mathrm{m}} n)t}, \\ &\simeq E_0 \mathrm{e}^{i\Omega_0 t} \left(\mathrm{J}_0(\beta) + \mathrm{J}_1(\beta)\mathrm{e}^{i\Omega_{\mathrm{m}} t} - \mathrm{J}_1(\beta)\mathrm{e}^{-i\Omega_m t} \right), \end{aligned} \tag{3.47}$$

where β is the modulation index, and the second equal sign in the above equation is the relation obtained by setting $t = \mathrm{e}^{i\Omega_{\mathrm{m}} t}$ in the mother function of the first kind of Bessel function,

$$\exp\left\{\frac{\beta}{2}\left(t - \frac{1}{t}\right)\right\} = \sum_{-\infty}^{\infty} \mathrm{J}_n(\beta) t^n, \tag{3.48}$$

and, the last approximation ignored the higher-order terms above the second order of the Bessel function and used the properties of the Bessel function

$$\mathrm{J}_{-n}(\beta) = (-1)^n \ \mathrm{J}_n(\beta). \tag{3.49}$$

From Eq. (3.47), it can be seen that the phase modulation generates two frequency components in addition to the original laser frequency component. The component with the same angular frequency Ω_0 as the original laser is called the carrier, while the component with angular frequency $\Omega_0 \pm \Omega_{\mathrm{m}}$ is called the upper (lower) sideband.

The PDH scheme utilizes the reflected light from the cavity. The cavity provides a different reflectance for each frequency component, as shown in Eq. (3.12). Thus, the reflected optical field E_{r} can be written as

$$\begin{aligned} E_{\mathrm{r}} &= E_0 \mathrm{e}^{i\Omega_0 t} \left\{ r\left(\Omega_0\right) \mathrm{J}_0(\beta) + r\left(\Omega_0+\Omega_{\mathrm{m}}\right) \mathrm{J}_1(\beta)\mathrm{e}^{i\Omega_{\mathrm{m}} t} - r\left(\Omega_0-\Omega_{\mathrm{m}}\right) \mathrm{J}_1(\beta)\mathrm{e}^{-i\Omega_{\mathrm{m}} t} \right\}, \\ &= E_0' \mathrm{e}^{i\Omega_0 t} + E_1 \mathrm{e}^{i(\Omega_0+\Omega_{\mathrm{m}})t} - E_{-1} \mathrm{e}^{i(\Omega_0-\Omega_{\mathrm{m}})t}, \end{aligned} \tag{3.50}$$

where $E_0' \equiv E_0 r\left(\Omega_0\right) \mathrm{J}_0(\beta)$, $E_1 \equiv E_0 r\left(\Omega_0+\Omega_{\mathrm{m}}\right) \mathrm{J}_1(\beta)$ and $E_{-1} \equiv E_0 r\left(\Omega_0-\Omega_{\mathrm{m}}\right) \mathrm{J}_1(\beta)$.

Since the photodetector ($\mathrm{PD_{refl}}$ in Fig 3.10) acquires the intensity of the light, by taking the square of the absolute value of the electric field in Eq. (3.50),

$$\begin{aligned} |E|^2 = (\text{DC Component}) &+ 2\,\mathrm{Re}\left[\left(-E_0' E_{-1}^* + E_0'^* E_1\right) e^{i\Omega_{\mathrm{m}} t}\right] \\ &+ \left(\text{Component of } 2\Omega_{\mathrm{m}}\right). \end{aligned} \tag{3.51}$$

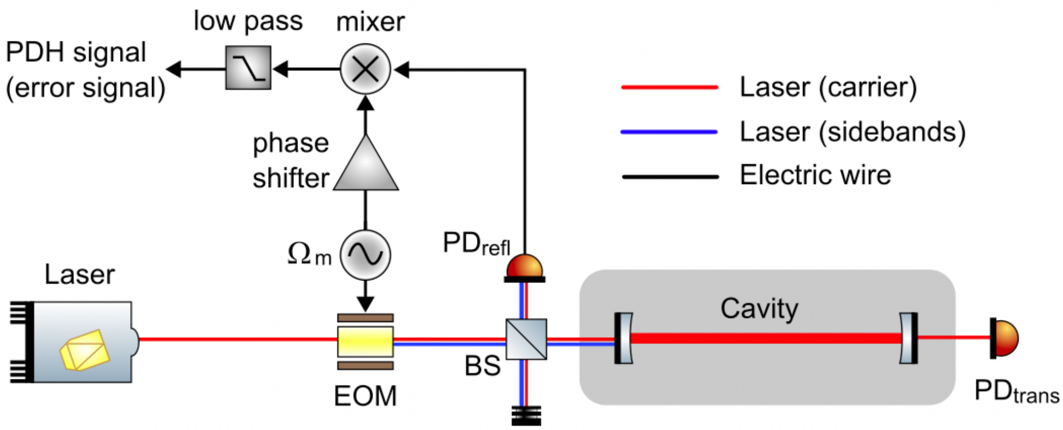

Figure 3.10: Layout of PDH scheme

By adapting this relation of Eq. (3.51) to Eq. (3.50), we can obtain,

$$|E_{\mathrm{r}}|^2 = 2E_0^2\ \mathrm{J}_0(\beta)\mathrm{J}_1(\beta)\,\mathrm{Re}\left[\left\{-r\left(\Omega_0\right)r^*\left(\Omega_0-\Omega_{\mathrm{m}}\right)+r\left(\Omega_0\right)^*r\left(\Omega_0+\Omega_{\mathrm{m}}\right)\right\}\mathrm{e}^{i\Omega_{\mathrm{m}}t}\right] \\ +\left(\text{DC Component}\right)+\left(\text{Component of } 2\Omega_{\mathrm{m}}\right). \tag{3.52}$$

By multiplying this signal with the signal from the oscillator used for modulation by the mixer, only the frequency components near Ω_{m} are down-converted to frequencies near DC. Here, by using the phase shifter, the phase of the signal from the oscillator is adjusted to be $\sin\left(\Omega_{\mathrm{m}}\mathrm{t}\right)$ with respect to the PD signal. By removing the RF component from the mixer output by the low-pass filter, the PDH signal V_{PDH} is obtained as

$$V_{\mathrm{PDH}} = E_0^2\ \mathrm{J}_0(\beta)\mathrm{J}_1(\beta)\,\mathrm{Im}\left[-r\left(\Omega_0\right)r^*\left(\Omega_0-\Omega_{\mathrm{m}}\right)+r\left(\Omega_0\right)^*r\left(\Omega_0+\Omega_{\mathrm{m}}\right)\right]. \tag{3.53}$$

The PDH signal and the cavity transmitted light, for comparison, are shown in Fig. 3.11. It can be seen that the error signal is obtained in the cavity resonance. This corresponds to extraction of the linear phase change in the reflected light near the resonance as a change in intensity by interfering with the carrier light near the resonance and the sidebands that are sufficiently far from the resonance (i.e., not sensitive to phase change). This can be understood from Eq. (3.53), which takes the imaginary part of the reflectivity. The structure on both sides corresponds to the resonance of sidebands where the carrier is non-resonant.

Let us consider the behavior of the PDH signal near the resonance point. Assuming that the sidebands are sufficiently far from the resonance point, we

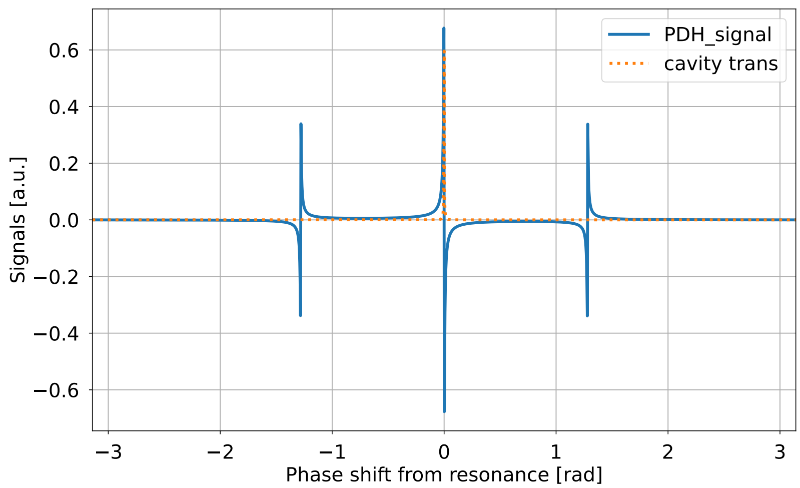

Figure 3.11: PDH signal and cavity transmitted light

can approximate $r^*(\Omega_0 - \Omega_\mathrm{m}) = r(\Omega_0 + \Omega_\mathrm{m}) \simeq r$ in Eq. (3.53). Therefore,

$$\begin{aligned} V_\mathrm{PDH} &\simeq E_0^2\ \mathrm{J}_0(\beta)\mathrm{J}_1(\beta) r\, \mathrm{Im}\left[-r(\Omega_0) + r(\Omega_0)^*\right] \\ &= 2E_0^2\ \mathrm{J}_0(\beta)\mathrm{J}_1(\beta) r\, \mathrm{Im}\left[r(\Omega_0)\right]. \end{aligned} \tag{3.54}$$

By plugging Eq. (3.12) into Eq. (3.54), we can obtain

$$V_\mathrm{PDH} = \frac{2E_0^2\ \mathrm{J}_0(\beta)\mathrm{J}_1(\beta) r t_\mathrm{e}^2 r_\mathrm{e} t^2 \sin\Phi}{1 + r_\mathrm{i}^2 r_\mathrm{e}^2 t^4 - 2r_\mathrm{i} r_\mathrm{e} t^2 \cos\Phi}. \tag{3.55}$$

By differentiating Eq. (3.55) to find the approximate width of the linear region,

$$\frac{\partial V_\mathrm{PDH}}{\partial\phi} = \frac{2E_0^2\ \mathrm{J}_0(\beta)\mathrm{J}_1(\beta) r t_\mathrm{e}^2 r_\mathrm{e} t^2}{1 + r_\mathrm{i}^2 r_\mathrm{e}^2 t^4 - 2r_\mathrm{i} r_\mathrm{e} t^2 \cos\Phi} \left\{\cos\Phi - \frac{2r_\mathrm{i} r_\mathrm{e} t^2 \left(1 - \cos^2\phi\right)}{1 + r_\mathrm{i}^2 r_\mathrm{e}^2 t^4 - 2r_\mathrm{i} r_\mathrm{e} t^2 \cos\Phi}\right\}. \tag{3.56}$$

Equation (3.56) takes extreme values when

$$\cos\Phi = \frac{2r_\mathrm{i} r_\mathrm{e} t^2}{1 + r_\mathrm{i}^2 r_\mathrm{e}^2 t^4}. \tag{3.57}$$

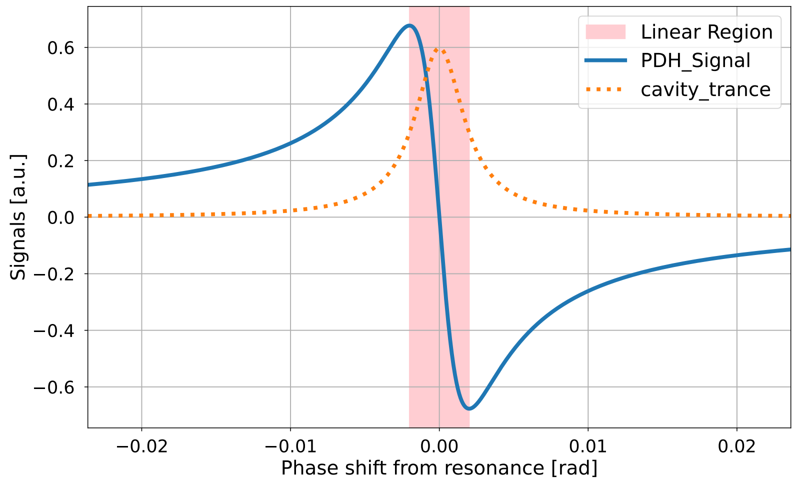

Figure 3.12: PDH signal and cavity transmitted light near the resonance

By expanding Eq. (3.57) to the second order of ϕ, we can obtain

$$\begin{aligned} \varPhi &\simeq \pm\frac{\sqrt{2}\,(1 - r_\mathrm{i} r_\mathrm{e} t^2)}{\sqrt{1 + r_\mathrm{i}^2 r_\mathrm{e}^2 t^4}} \\ &= \pm\frac{\pi}{\mathcal{F}} \end{aligned} \tag{3.58}$$

Here, we used the finesse expression (3.25). The above shows that the approximately linear region of the PDH signal is comparable with the FWHM of the cavity. Figure 3.12 provides a close-up view of the region near resonance, as shown in Fig. 3.11.

3.4 Noise sources in laser interferometric detector

3.4.1 Seismic noise

The surface of the earth is moving microscopically due to a variety of factors. The ground vibration is known to be generally proportional to f^{-2}, and the value varies from place to place. The amplitude spectral density δx_{seis} is modeled as

$$\delta x_{seis} = A \left(\frac{1\ \mathrm{Hz}}{f} \right)^2 [\mathrm{m}/\sqrt{\mathrm{Hz}}]. \tag{3.59}$$

It is known to be several orders of magnitude smaller underground than at the surface, and the value of coefficient A is $\sim 10^{-7}$ at the earth surface and $\sim 10^{-9}$ underground.

The seismic noise reduction is mainly performed by a pendulum called a suspension in the ground-based detectors. Let us consider the suspended mass as shown in Fig. 3.13. The equation of motion of the mass point can be written as follows, assuming that the mass displacement x is small.

$$m\frac{\mathrm{d}^2 x}{\mathrm{d}t^2} = -\frac{mg}{l}(x - x_0) - \mathit{\Gamma}\frac{\mathrm{d}(x - x_0)}{\mathrm{d}t}, \tag{3.60}$$

where the mass of the mass is m, the damping factor is $\mathit{\Gamma}$, and the suspended position is x_0. By Fourier transform above equation

$$-m\omega^2 X(\omega) = -\frac{mg}{l}(X(\omega) - X_0(\omega)) + i\frac{\mathit{\Gamma}\omega}{m}(X(\omega) - X_0(\omega)) \tag{3.61}$$

From the above results, the transfer function $X(\omega)/X_0(\omega)$ from the suspended part to the mass point can be written as,

$$\frac{X(\omega)}{X_0(\omega)} = \frac{\omega_0^2 - i\frac{\omega}{Q}}{\omega^2 + i\frac{\omega}{Q} - \omega_0^2}, \tag{3.62}$$

where ω_0 is the resonance frequency of the pendulum, $\omega_0^2 \equiv \frac{g}{l}$, and Q is the sharpness of the resonance, $Q \equiv \frac{m}{\mathit{\Gamma}}$. Some examples of the transfer functions are shown in Fig. 3.14. It can be seen that the pendulum has a vibration isolation effect proportional to f in the frequency range above the resonance frequency. We can obtain an vibration isolation ratio of $(1/f^2)^n$ in this region using a pendulum with n stages. On the other hand, there is no vibration isolation effect below the resonant frequency. The resonance frequency can be lowered by increasing the pendulum length, but since the effect is square root, it is not realistic to lower the resonance frequency beyond a certain level.

Thus, seismic noise increases at low frequencies. In addition, pendulums are incompatible because they are less effective at low frequencies. To avoid seismic noise on the ground, methods such as torsion pendulum [10] that can achieve low resonance frequencies and Atomic interferometer [11–13] that use free-falling atom are being considered. On the other hand, space detectors essentially solve this problem and provide high sensitivity at low frequencies.

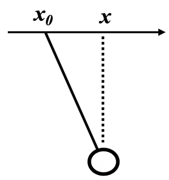

Figure 3.13: Suspended mass point.

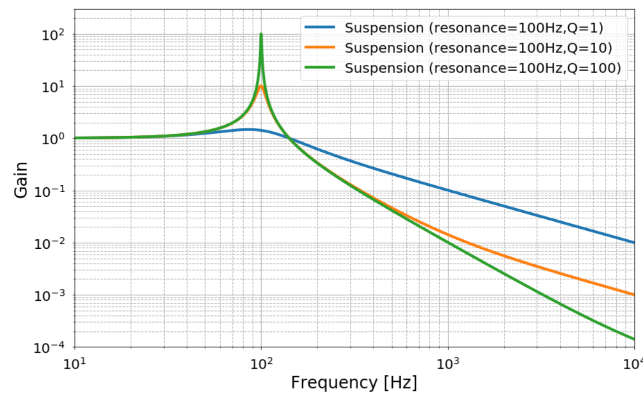

Figure 3.14: Transfer function from suspension point to mass point.

3.4.2 Thermal noise

The thermal noise is caused by the Brownian motion of the mirror substrate, mirror coatings, and suspension wires. The main methods to reduce the thermal noise are to cooling the mirrors and suspension wires or to use coatings and suspension wires with high Q factors. In this case, the temperature dependence of the Q factor should be taken into account.

3.4.3 Quantum noise

Here, we introduce the shot noise and radiation pressure noise derived from the quantum nature of light.

Shot noise

The interferometer detects the phase shift, and the shot noise is the quantum fluctuation of this phase. The shot noise can be determined from the fact that the variation of the number of photons follows the Poisson distribution and is proportional to the square root of the number of photons or the power of the light.

The shot noise for gravitational wave signals in the Michelson interferometer $h_{\rm mich\_shot}$ and the Fabry-Perot cavity $h_{\rm FP\_shot}$ can be written as follows, respectively [46,59]. The shot noise is proportional to the square root of the light power, and the gravitational wave signal is proportional to the light power. Therefore, the signal-to-noise ratio improves in proportion to the square root of the power. In the case of a Fabry-Perot cavity, the phase shift to the gravitational wave is $\pi/2\mathcal{F}$ times (i.e., N times) larger than the Michelson. In addition, a factor of 2 is added because a single Fabry-Perot cavity is considered, as compared to Michelson. Eq. 3.10 and 3.35 were used for the Michelson and Fabry-Perot frequency responses.

$$h_{\mathrm{MI\_shot}} = \frac{1}{2\pi L|H_{\mathrm{MI}}(\omega)|}\sqrt{\frac{h\lambda c}{2P}}\ [1/\sqrt{\mathrm{Hz}}]. \tag{3.63}$$

$$h_{\mathrm{FP\_shot}} = \frac{2}{2\pi L|H_{\mathrm{FP}}(\omega)|}\frac{\pi}{2\mathcal{F}}\sqrt{\frac{h\lambda c}{2P}}\ [1/\sqrt{\mathrm{Hz}}]. \tag{3.64}$$

Radiation pressure noise

The mirror receives radiation pressure as a reaction when it reflects light. At the same time, due to quantum fluctuations in the number of photons, the radiation pressure also fluctuates, generating displacement noise, which is called radiation pressure noise [46,59]. The effect of noise is smaller when the mass of the mirror receiving the force is large. In addition, the acceleration term in the equation of motion makes the factor of ω^{-2} in the frequency domain. Unlike shot noise, the noise increases as the power in the cavity increases. Therefore, the noise is lower with lower laser power and finesse.

$$h_{\mathrm{MI\_rad}} = \frac{|H_{\mathrm{MI}}(\omega)|}{m\omega^2 L}\sqrt{\frac{32hP}{c\lambda}}\ [1/\sqrt{\mathrm{Hz}}]. \tag{3.65}$$

$$h_{\mathrm{FP\_rad}} = \frac{2|H_{\mathrm{FP}}(\omega)|}{m\omega^2 L}\frac{2\mathcal{F}}{\pi}\sqrt{\frac{32hP}{c\lambda}}\ [1/\sqrt{\mathrm{Hz}}]. \tag{3.66}$$

3.4.4 Gravitational wave foreground noise

In order to observe the primordial gravitational waves (PGW), the gravitational waves from a large number of binary stars are expected to be noise [60, 61]. Multiple gravitational wave signals in one frequency bin result in the foreground noise that cannot be resolved. In particualar, in the region below 0.01 Hz, the effect of the gravitational waves from binary white dwarf systems is expected. There are plans such as DECIGO to observe the 0.1-10 Hz region with high sensitivity where these effects are minimal. However, even in the 0.1 Hz band, there is a possibility of foreground noise effects from binary neutron stars [50,51]. One of the purposes of B-DECIGO is to probe the effects of such foreground noise.

3.5 Sensitivity of GW detectors

This section summarizes the sensitivity of the major laser interferometric detectors. Figure 3.15 shows the sensitivity curves for the major laser interferometric gravitational wave detector projects design sensitivity for each gravitational wave frequency band [24, 57, 61] with the gravitational waves from CBC (1.4 $M_\odot$-1.4 $M_\odot$ in 40 Mpc and 1000 $M_\odot$-1000 $M_\odot$ in 1 Gpc) and PGW ($\Omega_{\rm GW} \sim 10^{-16}$), and foreground waves from WD binaries. The vertical axis is the detector noise calibrated to the gravitational wave amplitude, which can detect gravitational waves with amplitudes above the detector's sensitivity curve. Also, the noise budget of the sensitivity curve of KAGRA is shown in Fig. 3.16 [57], and the noise budget of DECIGO is shown in Fig. 3.17 [24].

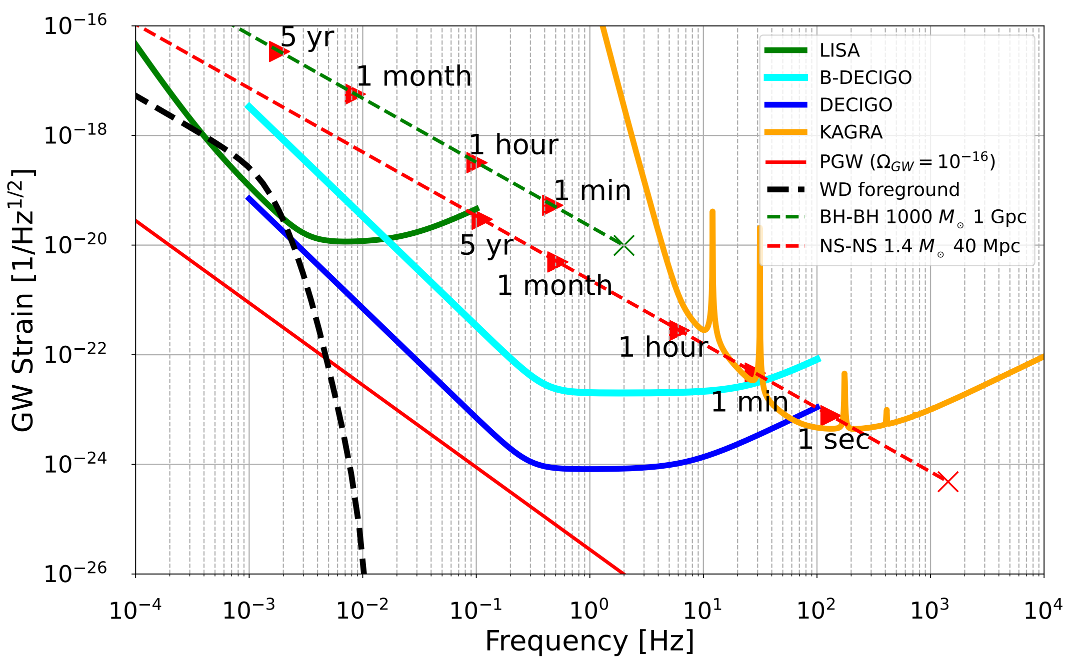

Figure 3.15: Sensitivity curves of major detectors.

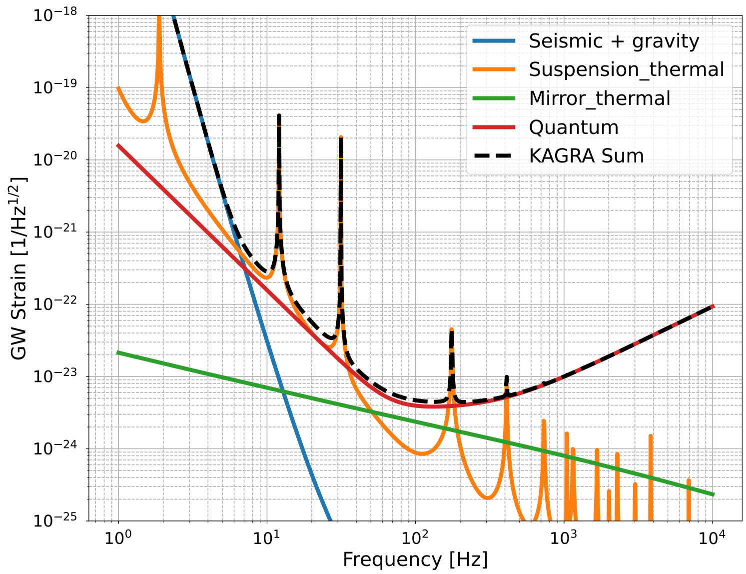

Figure 3.16: sensitivity curve of KAGRA.

Ground-based detectors, represented by KAGRA, are limited in their sensitivity in the low-frequency band by the seismic noise. Therefore, they observe high-frequency bands above $\sim$ 10 Hz. Expected observation targets include CBCs just before coalescence and supernova explosions. Advantages of the ground-based detector include better maintainability and the high feasibility of achieving high-power, complex interferometer configuration.

Space detectors are unaffected by seismic noise and can take longer baseline lengths, suitable for low-frequency band observations. It can detect heavier CBCs than observed on the ground or CBCs in the mass range observed on the ground at an earlier stage of the inspiral.

LISA consists of three spacecraft, each placed at the apex of a triangle with about 2.5×10^9 m sides to optimize for 0.1-100 mHz observation. Due to the long baseline length, the emitted laser spreads out due to diffraction, and the laser diameter becomes several tens of kilometers at the receiver side of the spacecraft, which can only receive a portion of the light. Therefore, LISA employs a method called an optical transponder. The spacecraft that receives the light phase locks the light to its own laser source and hits it back, making it behave like a pseudo-mirror. The spacecraft that first emitted the laser then interferes with the returned laser and its own laser and extracts the effects of gravitational waves. The sensitivity of optical transponders can basically be regarded as equivalent

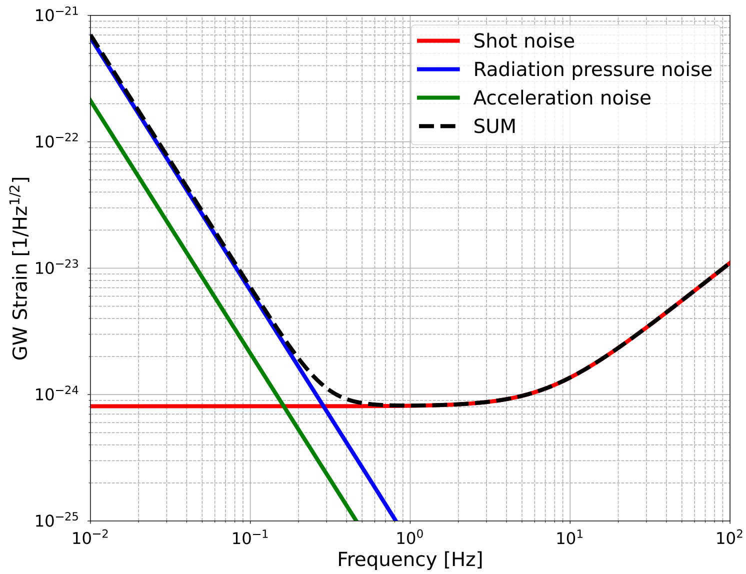

Figure 3.17: sensitivity curve of DECIGO.

to that of Michelson interferometers. LISA is expected to reveal the history of galaxy formation through observations of supermassive BH binary and verify the general theory of relativity in strong gravitational fields through observations of stellar BH orbiting supermassive BHs, called Extreme mass ratio inspiral (EMRI) [15].

DECIGO has a baseline length of about 1000 km (B-DECIGO is 100 km), optimized for observing the 0.1-10 Hz band. With this length, the laser diameter in the receiver side spacecraft is about 1 m and can be received mostly by a realistically sized mirror. This means that Fabry-Perot cavities can be implemented, and in fact, DECIGO utilizes a cavity with finesse 10 (finesse 100 with B-DECIGO). Since the sensitivity of DECIGO is largely limited by the shot noise, thus the introduction of cavities significantly improves the sensitivity. Instead, sensitivity in the low-frequency band worsens due to increased radiation pressure noise associated with increased laser power. Since the 0.1-10 Hz band is not affected by WD foreground, there is a possibility of direct observation of PGW by high-sensitivity observations in this band. In Fig. 3.15, the DECIGO sensitivity seems not to reach the expected amplitude of PGW, but it is estimated that it is possible to reach the PGW level with 3 years of correlated observations [24].

3.6 Comparison of Fabry-Perot cavity and optical transponder

In this section, we compare the Fabry-Perot cavity method and the optical transponder method for space detectors.

A representative detector that uses the Fabry-Perot cavity method is DECIGO. The properties of the Fabry-Perot cavity have already been summarized in Sect. 3.3.

On the other hand, the optical transponder is the method used in LISAL-ISA [15], TianQin [17], Taiji [16] and BBO [18]. The schematic view of the optical transponder-type gravitational wave detector is shown in Fig. 3.20. First, spacecraft 1 illuminates light to spacecraft 2. Spacecraft 2 then phase-locks an internal light source to the received light. The light is then returned to spacecraft 1. In this way, spacecraft 2 acts as a pseudo-mirror. Finally, spacecraft 1 extracts the gravitational wave signal from the heterodyne beat signals of the light returned from spacecraft 2 and the outgoing light. The response of the optical transponder to the gravitational wave is similar to that of the Michelson interferometer.

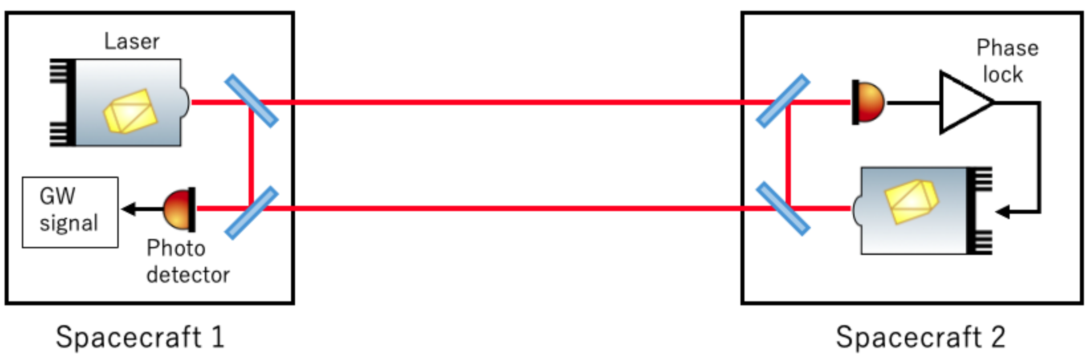

Figure 3.18: Schematic view of the optical transponder-type gravitational wave detector.

The emitted light spreads over a wider area with increasing distance due to diffraction. Therefore, when the distance between spacecraft increases, it is difficult toreflect the large portion of the light with a realistically sized mirror. The optical transponder method works even if a small portion of the radiated light is received. Therefore, it is possible to design very long baseline lengths.

Let us consider the following three cases of conditions as shown in Fig 3.19.

I. Base line length is 10^9 m and optical transponder method.
II. Base line length is 10^6 m and optical transponder method.
III. base line length is 10^6 m and a Fabry-Perot cavity method.

The power of the light source is set to 10 W. It is assumed that all light can be received at a baseline length of 10^6 m. Although detailed studies have been performed for diffraction loss [62], for simplicity, it is assumed that at distances above 10^6 m, the received light power decreases in proportion to the square of the distance. In other words, the optical power that can be received in Condition I is 10^{-5} W. The finesse of the Fabry-Perot cavity was set to 10.

The sensitivity curve of the gravitational wave detector for each condition is shown in Fig. 3.19. Here, only the shot noise and radiation pressure noise given by Eq. (3.63-3.66) were considered for noise. Note that sensitivity curves such as DECIGO and LISA in Sect. 3.5 simplify the response of Michelson and Fabry-Perot. In addition, in the case of actual LISA and B-DECIGO, the low frequency band is limited by acceleration noise [22, 63].

Consider the sensitivity based on Condition I. Radiation pressure noise is low because the received light is very weak. Due to the long light travel time associated with the long arm, it is not suitable for high-frequency gravitational wave detection. In Condition II, where the arm is shortened from Condition I, the received light power increases from Condition I. As a result, the radiation pressure noise increases and the low frequency band is limited. The shot noise decreases proportionally to the distance. However, the gravitational wave signal also decreases proportional to the distance. Thus, the noise floor remains the same. On the high frequency side, the cutoff frequency shifts to a higher frequency due to the shorter travel time of the light. In condition III, the phase change obtained for the gravitational wave is greater than $2\mathcal{F}/\pi$ times than the transponder. Thus the sensitivity is increased correspondingly. On the other hand, radiation pressure noise worsens further as the amount of light is amplified by the cavity.

As described above, the optical transponders are suitable for low-frequency band observations due to the long baseline length and small radiation pressure noise. On the other hand, for the distance where sufficient amount of light can be received, higher sensitivity can be obtained at the same optical power by introducing a Fabry-Perot cavity.

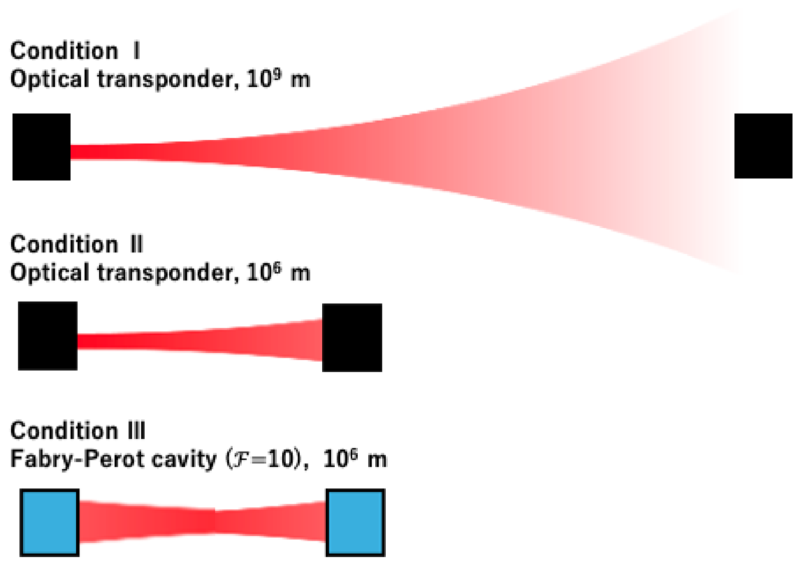

Figure 3.19: Schematic view of each condition. It is assumed to be a single arm in all cases.

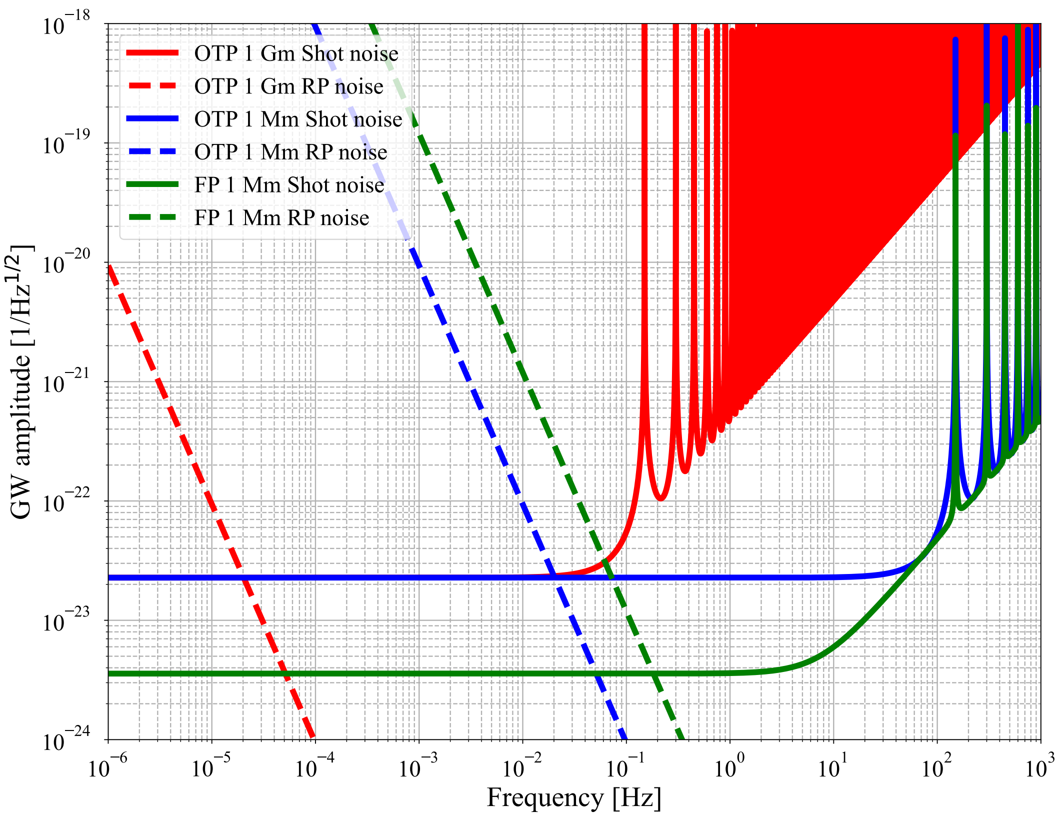

Figure 3.20: Shot noise and radiated pressure noise for each condition. Note that the noise of the optical transponder is twice larger than the expression in Eq. (3.63 and 3.65) because the single arm is considered. For the notation of legends in the figure, RP indicates radiation pressure, and OTP indicates optical transponder.

Chapter 4
BACK-LINKED FABRY–PEROT INTERFEROMETER

In this chapter, we explain the working principle of Back-Linked Fabry–Perot Interferometer (BLFPI), and then summarize the mechanism of the frequency noise reduction method in the post-process, called the subtractive method.

4.1 Working principle of Back-Linked Fabry–Perot Interferometer as a gravitational wave detector

A schematic view of the entire laser interferometric space detector utilizing the BLFPI and the schematic view of the internal structure of each spacecraft are shown in Fig. 4.1.

BLFPI consists of three spacecraft deployed at the apex of a triangle. Each of the three spacecraft has two mirrors that act as test masses against the gravitational waves and constitute three Fabry-Perot cavities in the orbit. The cavity resonance is maintained by feeding back the error signal acquired by the PDH scheme to the frequency actuators of the lasers. Since BLFPI is equipped with two lasers in one spacecraft, all resonant degrees of freedom can be controlled by the laser frequency only i.e., in principle, it is not required to control the cavity length. In addition, since each laser follows the cavity independently, BLFPI has the advantage that it can be realized with a simple control system.

I briefly explain the working principle of BLFPI and set the definitions of parameters relevant to the experiment. While the proposal paper [35] handles frequency noises in terms of phase in rad, I treat them in terms of frequencies

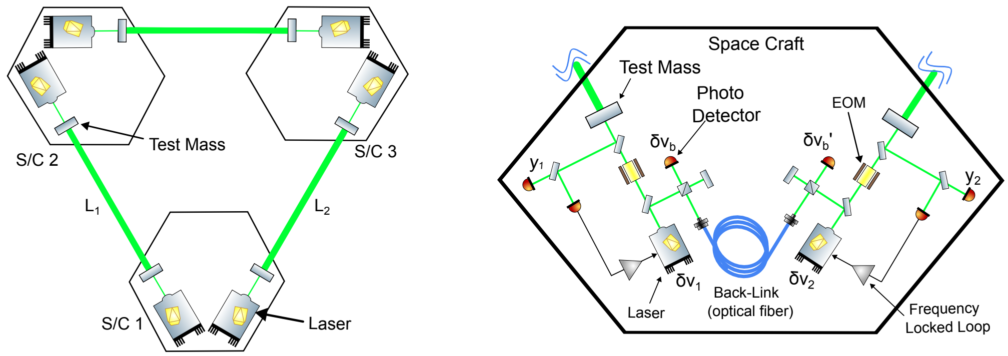

(a) (b)

Figure 4.1: (a) Schematic view of the BLFPI. Three inter-satellite interferometers are constructed by three S/C (spacecraft). Each spacecraft is equipped with two laser sources so that all lasers can be locked to the cavities by frequency locked loops without controlling the position of test masses. (b) Schematic of the internal optical system of each S/C. The heterodyne beat signals as $\delta\nu_{\mathrm{b}}$ and $\delta\nu_{\mathrm{b}}'$ are acquired at each end of the back-link path with two photodetectors. The combination of the two heterodyne signals can subtract phase noises introduced in the back-link fiber in the post-process. The reflected light from each cavity is monitored by two photodetectors, one for laser frequency control and the other out-of-loop photodetectors for obtaining the y_1 and y_2 signals for the subtraction.

in Hz such that they can be easily translated to the measurement values in the experiment.

Figure 4.2 illustrates the block diagram for a single interferometer of the BLFPI constellation. The frequency of each laser source is converting frequency into voltage with a sensing transfer function S_j with $j = 1, 2$. The each laser source is locked to the corresponding cavity length via a liner servo filter F_j. The frequency of each laser comes with fluctuations or frequency noise denoted by $\delta\nu_j$. The frequency locking servo then suppresses frequency noises by feeding the signal back to a frequency actuator A_j. Consequently, the laser frequency tracks the cavity length fluctuation δL_j.

The back-link path optically combines the two laser beams before they are incident on the Fabry-Perot cavities, producing heterodyne beatnote signals. Due to the frequency-locked loops, the beatnote signals contain the frequency noises of laser sources as well as the length fluctuation of the Fabry-Perot cavities. The

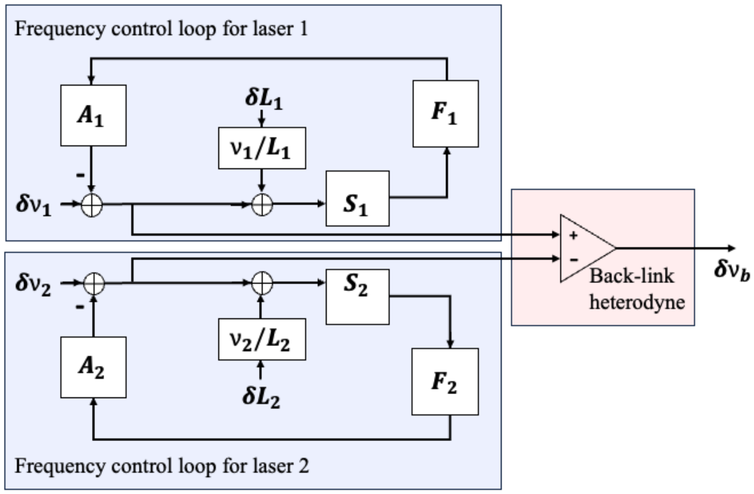

Figure 4.2: Block diagram of the control system for the BLFPI. The system is composed of two laser control loops. The control loops lock the laser frequency to the resonant frequency of respective cavities. The difference frequencies of the controlled lasers are acquired as the beat signal by the backlink heterodyne interferometer.

beat signal in terms of its frequency shift $\delta\nu_{\mathrm{b}}$ can be expressed as

$$\delta\nu_{\mathrm{b}} = \frac{1}{1+G_1}\delta\nu_1 - \frac{G_1}{1+G_1}\frac{\nu_1}{L_1}\delta L_1 - \frac{1}{1+G_2}\delta\nu_2 + \frac{G_2}{1+G_2}\frac{\nu_2}{L_2}\delta L_2. \tag{4.1}$$

where G_j describe a open loop gain defined by $G_j \equiv S_j F_j A_j$.

Here, assuming infinity for the control gain G_j, $\delta\nu_{\mathrm{b}}$ can be written as

$$\delta\upsilon_{\mathrm{b}} = \frac{\delta L_1}{L_1}\nu_1 - \frac{\delta L_2}{L_2}\nu_2. \tag{4.2}$$

The relative change in length is equal to gravitational waves amplitude, $h \sim \delta L/L$, as derived in Eq. (2.18),

$$\delta\upsilon_{\mathrm{b}} = (h_1 - h_2)\,\nu. \tag{4.3}$$

where h_j is the amplitude of gravitational waves through L_j and we used the fact that the laser frequencies can be approximated as $\nu_1 \sim \nu_2 \sim \nu$ as we will show later. In this way, the beat signal provides a measurement of gravitational waves. This is the basic principle of operation of BLFPI as a gravitational wave detector.

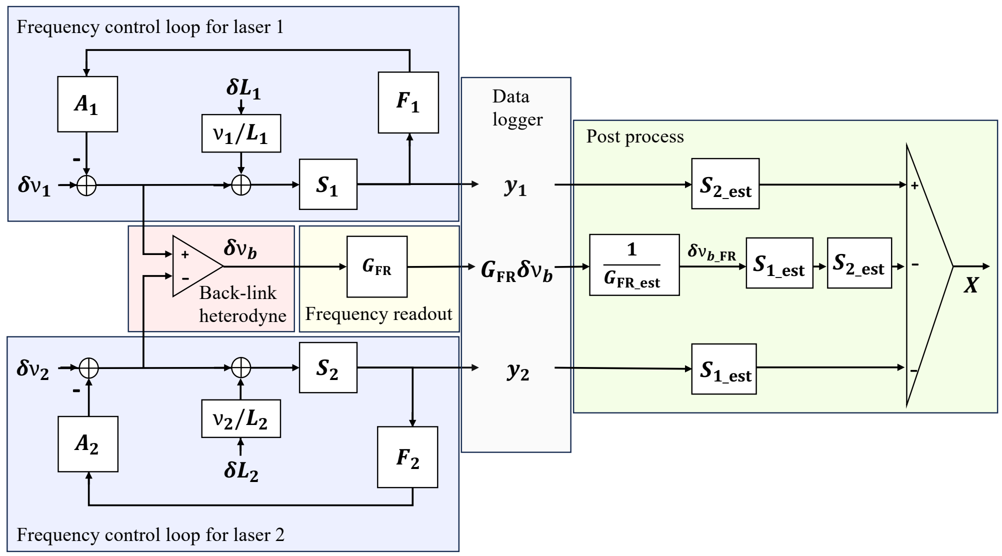

Figure 4.3: Block diagram of the control system and post process for the BLFPI. The system consists of the experimental system for signal acquisition and the post process system to subtract laser frequency noises. The experimental system is further divided into the control system to lock the lasers to a cavity resonance, the back-link part to monitor the heterodyne beat signals, and the frequency readout part to monitor the time evolution of the beatnote frequency.

4.2 Frequency noise subtraction

In reality, G_j has a finite value. Thus, the frequency noise is still very large relative to the expected gravitational wave signal. In order to subtract the frequency noise in BLFPI, a post-process called the subtraction method has been proposed. The block diagram of BLFPI, which is closer to the actual operation, is shown in Fig. (4.3). In this diagram, in addition to the experimental setup, the signal acquisition using data loggers and the subtraction method using estimated values are considered.

The error signals for the j-th laser source with respect to the length of cavity can be expressed in the frequency domain as

$$y_j = \frac{S_j}{1+G_j}\delta\nu_j + \frac{S_j}{1+G_j}\frac{\nu_j}{L_j}\delta L_j. \tag{4.4}$$

In the subtraction method, the frequency noise is subtracted from the heterodyne beat signal using this error signal leaving the effect of the gravitational wave.

The frequency shift has to be read out and converted to a voltage by a phase meter, in practice. The transfer function from frequency to voltage is given by G_{FR}.

Once the three measurement data y_j and ν_{b} are recorded at the same time, one can obtain the synthesized signal X as

$$
\begin{aligned}
X &= \delta\nu_{b\_\mathrm{FR}} S_{1\_\mathrm{est}} S_{2\_\mathrm{est}} - \left(y_1 S_{2\_\mathrm{est}} - y_2 S_{1\_\mathrm{est}}\right), \\
&= \left[\frac{1}{1+G_1}\left\{\left(\frac{G_{\mathrm{FR}}}{G_{\mathrm{FR}\ \_\mathrm{est}}} - \frac{S_1}{S_{1\_\mathrm{est}}}\right)\delta\nu_1 \ - \left(\frac{G_{\mathrm{FR}}}{G_{\mathrm{FR}\ \_\mathrm{est}}} G_1 + \frac{S_1}{S_{1\_\mathrm{est}}}\right)\frac{\nu_1}{L_1}\delta L_1\right\}\right. \\
&\quad \left. - \frac{1}{1+G_2}\left\{\left(\frac{G_{\mathrm{FR}}}{G_{\mathrm{FR}\ \_\mathrm{est}}} - \frac{S_2}{S_{2\_\mathrm{est}}}\right)\delta\nu_2 \ - \left(\frac{G_{\mathrm{FR}}}{G_{\mathrm{FR}\ \_\mathrm{est}}} G_2 + \frac{S_2}{S_{2\_\mathrm{est}}}\right)\frac{\nu_2}{L_2}\delta L_2\right\}\right] S_{1\_\mathrm{est}} S_{2\_\mathrm{est}}.
\end{aligned}
\tag{4.5}
$$

The quantities with the subscript "est" represent the estimated parameters for the subtraction method. Assuming that S_1, S_2, and G_{FR} can be estimated with sufficiently high accuracy so that $S_{1\_est} \to S_1$, $S_{2\_est} \to S_2$, and $G_{\mathrm{FR}\ \_\mathrm{est}} \to G_{\mathrm{FR}}$, one can arrive at

$$
\begin{aligned}
X &= \left(-\frac{\nu_1}{L_1}\delta L_1 + \frac{\nu_2}{L_2}\delta L_2\right) S_1 S_2, \\
&= \left\{\left(-\frac{\nu_1}{L_1} + \frac{\nu_2}{L_2}\right)\delta L_+ - \left(\frac{\nu_1}{L_1} + \frac{\nu_2}{L_2}\right)\delta L_-\right\} S_1 S_2, \\
&\approx \left\{\frac{-\mathit{\Delta} L}{L_1\left(L_1 + \mathit{\Delta} L\right)}\delta L_+ - \frac{2L_1 + \mathit{\Delta} L}{L_1\left(L_1 + \mathit{\Delta} L\right)}\delta L_-\right\} S_1 S_2 \nu,
\end{aligned}
\tag{4.6}
$$

with $\delta L_\pm$ being the common and differential components of two lengths defined by

$$
\delta L_\pm \equiv \frac{\delta L_1 \pm \delta L_2}{2}. \tag{4.7}
$$

In addition, we have approximated the laser frequencies as $\nu \approx \nu_1 \approx \nu_2$. This is valid as long as the beatnote frequency is approximately 100 MHz or smaller for the laser frequency of several 100 THz, as mentioned in Sect 5. In this case, the relative difference between the two laser frequencies should be less than 1 ppm. Two cavity lengths are related via $L_2 \equiv L_1 + \mathit{\Delta} L$ where $\mathit{\Delta} L$ is the macroscopic difference.

The synthesized output now contains only the displacement of the cavity length. In the event of gravitational waves passing through the Fabry-Perot cavity, they appear as the differential mode of the lengths with the laser frequency noises subtracted. This is the working principle of the BLFPI and frequency noise subtraction. As is apparent from Eq. (4.5), the success of frequency noise subtraction largely depends on the accuracy in the estimation of the interferometer responses S_1 and S_2. Additionally, the transfer function for the frequency readout G_{FR} also affects the subtraction performance. However, it can be independently calibrated with an oscillator of known amplitude and frequency.

Chapter 5
EXPERIMENTAL SETUP

For the practical application of the BLFPI, it is necessary to conduct the experimental test to demonstrate the frequency noise subtraction and possibly identify issues associated with the implementation.

In this chapter, we summarize the layout for the demonstration experiment and the implementation method of the subtraction process.

First, it summarizes the requirements and design of the experimental setup. Second, the configuration of the optical and control systems are described. Third, I summarize the evaluation of the constructed experimental system. Finally, I summarize the implementation of the subtraction process.

5.1 Requirements and design of the experimental setup

The requirements for the experimental layout are as follows.

· The experimental setup shall be to perform demonstrations under conditions as relevant as possible to the actual implementation.
· It shall be capable of demonstrating the reduction of frequency noise by the subtraction method in a laboratory environment.

From the first condition, the experimental setup consisted of two uncorrelated lasers and two Fabry-Perot cavities. This corresponds to simulating a BLFPI consisting of the three spacecraft shown in the red framed area of Fig. 5.1. In the laboratory, it is difficult to conduct the demonstration with the same scale and frequency bandwidth as a actual implementation due to the limitation in available space. In this time, we focused on the cavity pole, which is the char-

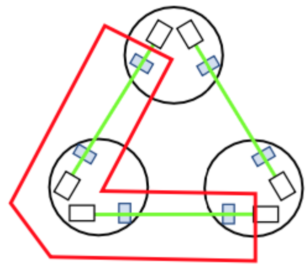

Figure 5.1: The red boxed area of BLFPI is simulated in the experimental setup.

Table 5.1: Comparison of the experimental setup and space detectors for the main parameters of the optical cavity.

	Experimental setup	DECIGO
Cavity length [m]	0.46	1.0×10^6
Free spectral range [Hz]	$\sim 3.3 \times 10^8$	1.5×10^2
Finesse	$\sim 10^4$	10
Cavity pole [Hz]	$\sim 10^4$	7.5
Frequency band [Hz]	$100 - 5.0 \times 10^4$	$0.1 - 10$
Laser wave length [nm]	1064	515
Cavity Incident Laser Power [W]	$\sim 2.5 \times 10^{-3}$	10

acteristic frequency point of Fabry-Perot cavities. Detectors such as DECIGO include cavity poles in their observation band. Therefore, it is important to demonstrate the subtraction method in the frequency band around the cavity pole. We adopted an experimental setup that enables us to demonstrate the subtraction method in the band, including the cavity pole. Specifically, the cavity finesse was set to a high value to increase the travel time of light in the cavity so that the cavity pole is included in the realistic measurement bandwidth. Table 1 shows a comparison of the main cavity of DECIGO and the experimental setup.

To achieve the second condition, the following two designs were employed. One is a design with two Fabry-Perot cavities incorporated into a single spacer, as shown in Fig. 5.2. In a laboratory environment, disturbances such as acoustics, vibrations, and temperature changes are expected. In this design, the two cavity

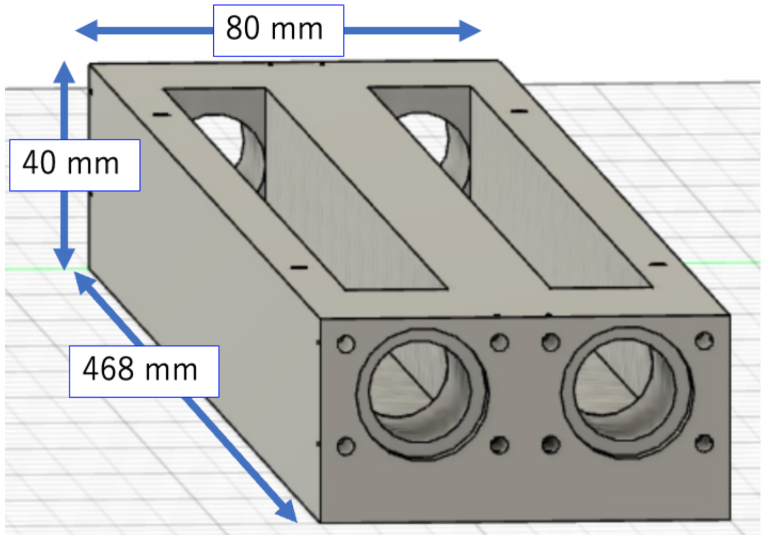

Figure 5.2: Spacer design with two cavities incorporated.

lengths are expected to displace in common. As a result, the disturbances are expected to be common-mode rejected from the heterodyne beat signal of the laser following the two cavity lengths.

The other is the excitation of laser frequency noise. Despite the cavity design described above, technical noise remains in the beat signal, as will be shown later. To achieve a demonstration in this situation, we excited the laser frequency noise with a known signal and measured the reduction of the elevated frequency noise.

5.2 Layout of the experimental system

The experimental setup for our demonstration is illustrated in Fig. 5.3 where an equivalent of the single BLFPI miniature is built on a tabletop under the atmospheric pressure. Details of the actual layout and the model numbers of the components used are summarized in Appendix D. Two independent laser sources at a wavelength of 1064 nm are employed. Each laser field is divided into two paths by an unpolarized beam splitter with a splitting ratio of 50:50. One is the optical path to the cavity, and the laser field is phase-modulated by an Electro Optic Modulator (EOM) at a radio frequency before the Fabry-Perot cavity, allowing for the Pound- Drever-Hall readout scheme [58]. The other backlink

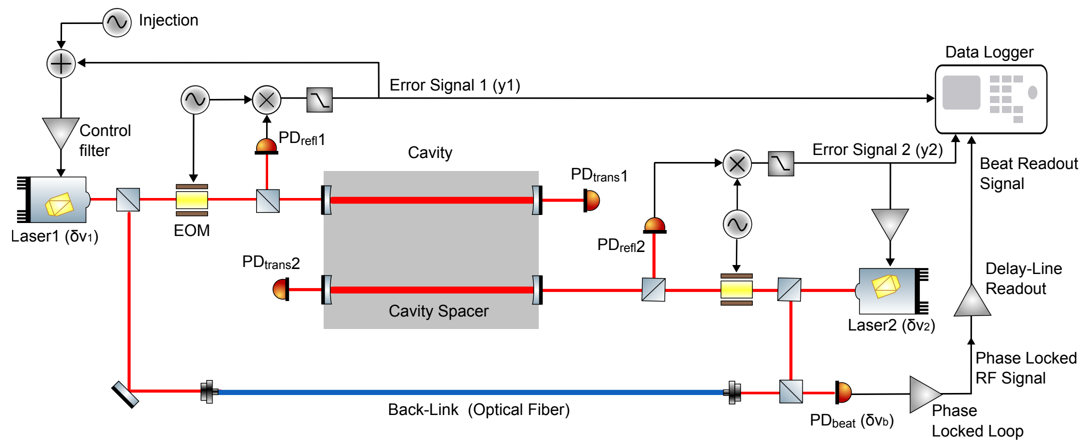

Figure 5.3: Experimental setup for demonstration. It consists of the laser frequency locked loops using the Pound-Drever-Hall readout and the back-link part for producing the heterodyne beatnote signals. The frequency fluctuation of the heterodyne beatnote signal is converted to voltage signals by the combination of the phase locked loop and delay line. The frequency fluctuations is then recorded by the data logger along with the error signals (200 kHz sampling rate with 64 kHz aliasing filter). The difference from the spacecraft layout shown in Fig. 4.1b is that the error signal used for subtraction process is shared with the in-loop signal used for laser frequency lock. Since the phase noise expected to be introduced from the 1 m length backlink optical fiber [64] is almost negligible compared to the expected noise floor shown in Fig. 5.7, the heterodyne beat signal is acquired with only one photodetector. In addition, square waves to excite the frequency noise are injected for the demonstration at a point before the control filter of the frequency locked loop for laser 1.

optical path is implemented by a 1 m of optical fiber sending the light of a laser source to the other, producing the heterodyne beatnote. Each laser light has a power of about 5 mW before the beamsplitter.

The frequency of each laser is locked to the cavity length by feeding the Pound-Drever-Hall signals with a linear control filter. Therefore, two Fabry-Perot cavities are locked at resonance points.

The two Fabry-Perot cavities have an identical design length value of 46 cm. The finesse of cavity 1 was measured to be approximately 11000, and 14000 for cavity 2 from the open loop transfer function fitting. The fitting results are described later. We estimated the cavity pole frequency to be approximately

15 kHz and 12 kHz, for cavities 1 and 2, respectively based on the measurement values for finesse. A dedicated spacer accommodating the two Fabry-Perot cavities is designed and implemented. The spacer is made of a super invar, IC-36FS, from Shinhokoku Material Corporation with a dimension of $80 \times 460 \times 40$ mm^3. The thermal expansion coefficient is expected to be 0.8 ppm/K so that the effect from ambient temperature is small. The cavity mirrors are attached to the spacer with a combination of acrylic plate and rubber ring. Additionally, we installed an aperture mask in both intra-cavities to suppress the excitation of high-order spatial modes.

Since, as shown later, the laser frequency noises are far below the technical noises across the frequency band, a function generator was hooked up to laser 1 to deliberately increase the magnitude of the frequency noise. The square waves at a fundamental frequency of 113 Hz are applied to increase the laser frequency noise in a broad frequency range. The excitation can be switched off whenever necessary.

5.3 Evaluation of the experimental setup

5.3.1 Open loop transfer function of frequency lock loop

The measured open-loop transfer functions (OLTF) for each loop and their fitting results are shown in Figs 5.4 and 5.5. The unity gain frequency for both loops is approximately 40 kHz and the phase margin is approximately 45-50 deg. The following model function Eq. 5.1 was used for the fitting. Here, S_j is the sensing transfer function. a_j, τ_j, and $f_{c,j}$ are all constants of real values representing the optical gain in V/Hz, relative time delay in sec, and cavity pole frequency in Hz, respectively. Since the free spectral range of the cavity is a sufficiently high value of $\sim$326 MHz comparing to the frequency band of interest, the single-pole model is accurate enough for our purpose as confirmed by Fig. 3.8. The servo-filter transfer function F_j and the laser frequency actuator efficiency A_j are known values obtained from another measurement.

The obtained parameters for each sensing transfer function as a result of the fitting are summarized in Table 5.2. The results show that the cavity finesse satisfies the requirement mentioned above. The values of these parameters fluctuate several percent depending on the time the measurements are performed. This may be related to the temporal variation of the system, discussed in later chapters.

$$G_j(f) = S_j(f)F_j(f)A_j, \\ = \frac{a_j \exp(-2\pi f \tau_j \mathrm{i})}{1 + \mathrm{i}f/f_{c,j}} F_j(f)A_j. \tag{5.1}$$

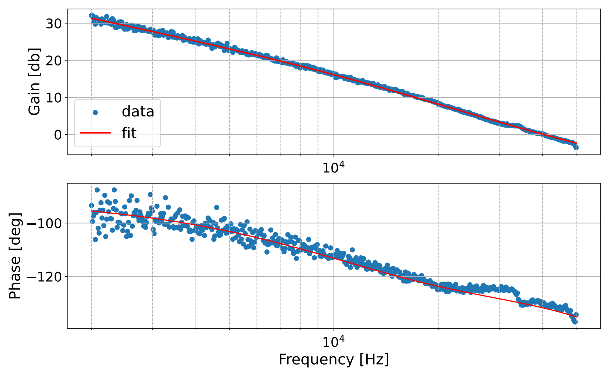

Figure 5.4: Measured OLTF and fitting results for Frequency Locked Loop 1.

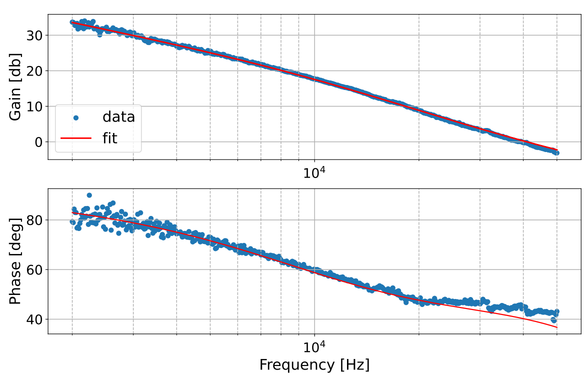

Figure 5.5: Measured OLTF and fitting results for Frequency Locked Loop 2.

Table 5.2: Parameters of the sensing transfer function obtained by OLTF fitting

	loop 1	loop2
a_j [V/Hz]	$4.78 \pm 0.02 \times 10^{-6}$	$2.40 \pm 0.01 \times 10^{-6}$
$f_{c,j}$ [Hz]	$1.43 \pm 0.03 \times 10^{4}$	$1.11 \pm 0.02 \times 10^{4}$
τ_j [sec]	$1.54 \pm 0.22 \times 10^{-6}$	$1.71 \pm 0.19 \times 10^{-6}$

5.3.2 Signals measured from the control system

Control signal

The control signals of the frequency-locked loops were measured to evaluate the system. The control signal is the feedback signal from the control filter to the frequency actuator of the laser. The control signal corresponds to the level of disturbance that the frequency actuator compensates for maintaining the resonance. From the control signal, the cavity length fluctuations and laser frequency noise can be mainly evaluated.

The top panel of Fig. 5.6 shows the control signal without 113 Hz excitation measured at each loop and the laser frequency noise during the free run. The control signal is calibrated to the frequency noise by multiplying the laser actuator efficiency. The laser frequency noise during the free run was obtained by measuring the heterodyne beat signal in the uncontrolled state with the phase meter. The bandwidth of the phase-locked loop of the phase meter is approximately 10 kHz. The bottom row of Fig. 5.6 shows the coherence of the two control signals.

The bands where the laser frequency noise is not dominant in the control signal are considered to be dominated by cavity length variations. In fact, high coherence is obtained in such bands. This means that the cavity design assuming common mode length variation as described above is functional.

Heterodyne beat signal and error signals

Two types of signals are recorded in the measurements for demonstrate the subtraction method. One is the error signals derived by the Pound-Drever-Hall scheme, representing the relative measure of laser frequency with respect to the cavity length. The setup contains two such signals, y_1 and y_2, introduced in the previous chapter. The other type is the frequency variations of the beatnote generated by the back-link heterodyne. It corresponds to ν_b introduced in the previous chapter. This beatnote signal is designed to produce a monochromatic

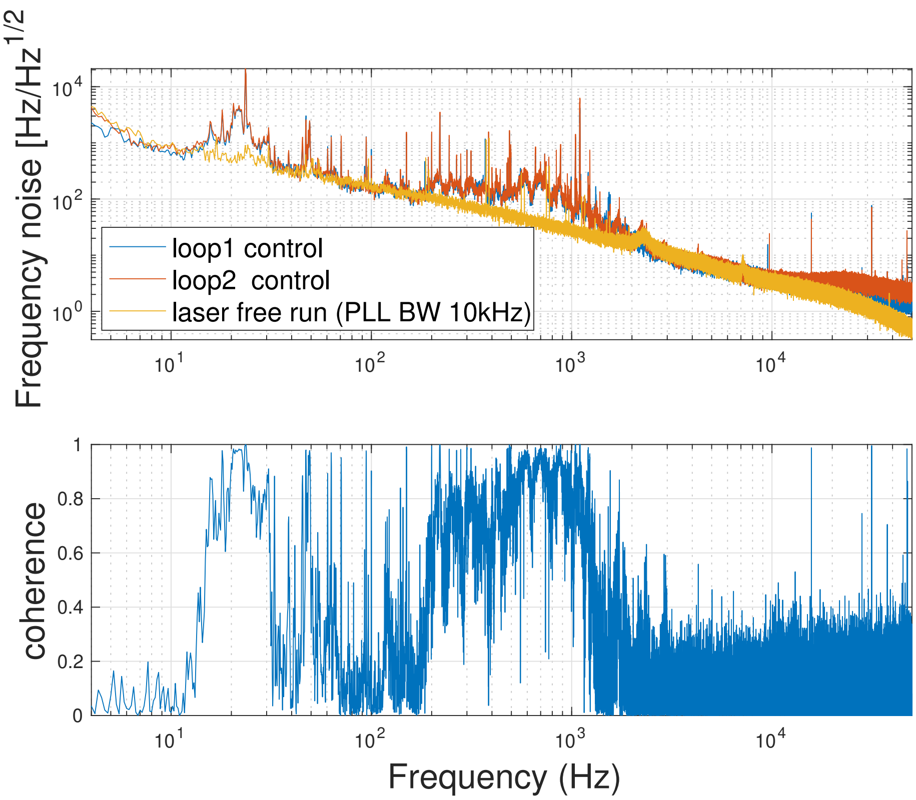

Figure 5.6: The control signal for each laser locked loop and the laser frequency noise during the free run (upper panel) and their coherence (lower panel). The control signals are calibrated to frequency noise by multiplying the actuator efficiency.

oscillative signal at 10-160 MHz. The center frequency of the beatnote signal can change depending on the resonant conditions of the Fabry-Perot cavities. The beatnote signal is then fed to a commercial phasemeter which tracks the phase evolution via the digital phase-locked loop. The phasemeter then produces an analog copy of the input signal with a fixed amplitude to reduce the adverse effect from amplitude fluctuations and higher harmonics. Finally, the analog copy of the beatnote signal is converted into the voltage signal in proportional to the beatnote frequency via the delay line fequency discreminator [65]. Although the phasemeter has the function of recording the phase evolution, we did not use it. The use of the phase record function will require an additional system to synchronize the phasemeter and data logger. The details of the response measurements for the phase meter and delay line are shown in the Appendix B.

The spectrum of the beatnote frequency without the subtraction was determined to be dominated by technical noises as summarized in Fig. 5.7. Unexpected acoustic noise exists in a broad band up to several kHz. Since these acoustic noises are not present when the cavities are not resonant, they are likely be associated with the frequency locked loops. Possible noise sources include the residual of the differential cavity fluctuation and the sensing noise of the control. The ADC noise of the data logger, which is dominant at high frequencies, can be reduced by introducing a preamplifier if lower noise is required in future.

The noise budgets and measurements of the error signal in both loops are shown in Figs. 5.8 and 5.9. On the high frequency side, the error signal is consistent with the budget, indicating that laser frequency noise is dominant. On the other hand, on the low frequency side, there is unexpected acoustic noise similar to the beatnote signal.

The budget in Fig. 5.7 assumes a perfect common-mode fluctuation in the length of the two cavities.

5.4 implementation of the subtraction process

The subtraction process was implemented in the frequency domain as opposed to the time domain. As pointed out in time-delay interferometry for LISA [37], the frequency domain subtraction introduces undesired residuals due to the finite-length Fourier transform. Nonetheless, in our demonstration the subtraction ratio is not limited by that and therefore adopted the frequency domain treatment for simplicity.

The data streams y_1, y_2 and ν_{b_FR} are divided into $2n-1$ data chunks each

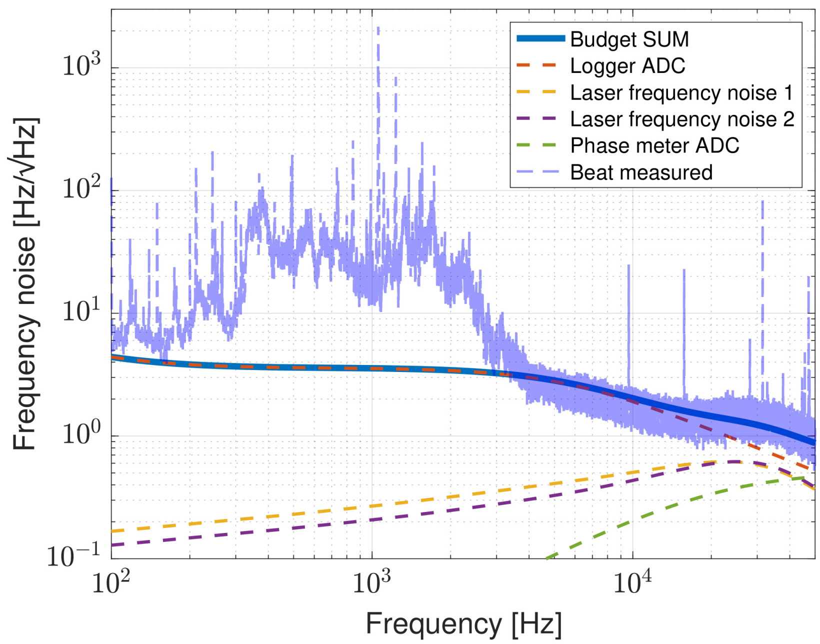

Figure 5.7: Amplitude spectral densities of measured frequency fluctuation at the heterodyne beatnote $\delta\nu_{\mathrm{b}}$ and various estimated noise contributions. (Dashed blue) Measured noise without an excitation. (Thick blue curve) Quadrature sum of all known noise contributions. (Red dashed) digitization noise of ADC or analog-to-digital converter for the logger used for recording the heterodyne beatnote. (Dashed yellow) Suppressed laser frequency noise from laser 1. (Dashed purple) the same for laser 2. (Dashed green) ADC digitization noise for the digital phase-locked loop in the phasemeter.

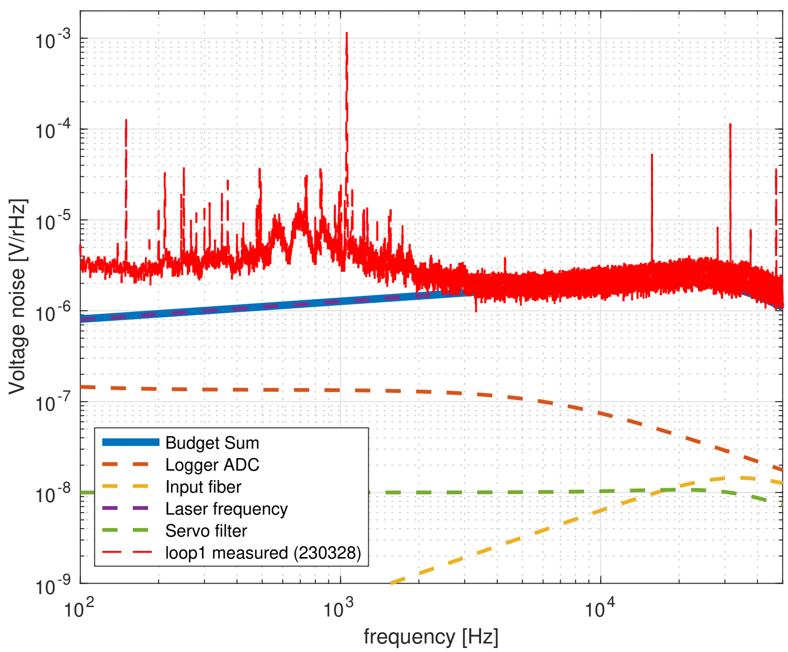

Figure 5.8: Amplitude spectral densities of measured frequency fluctuation at the error signal y_1 and various estimated noise contributions. (Dashed red) Measured noise without an excitation. (Thick blue curve) Quadrature sum of all known noise contributions. (orange dashed) digitization noise of ADC or analog-to-digital converter for the logger used for recording the signal. (Dashed purple) Suppressed laser frequency noise from laser 1. (Dashed green) Circuit noise in servo filter. (Dashed yellow) Optical fiber noise in input optics.

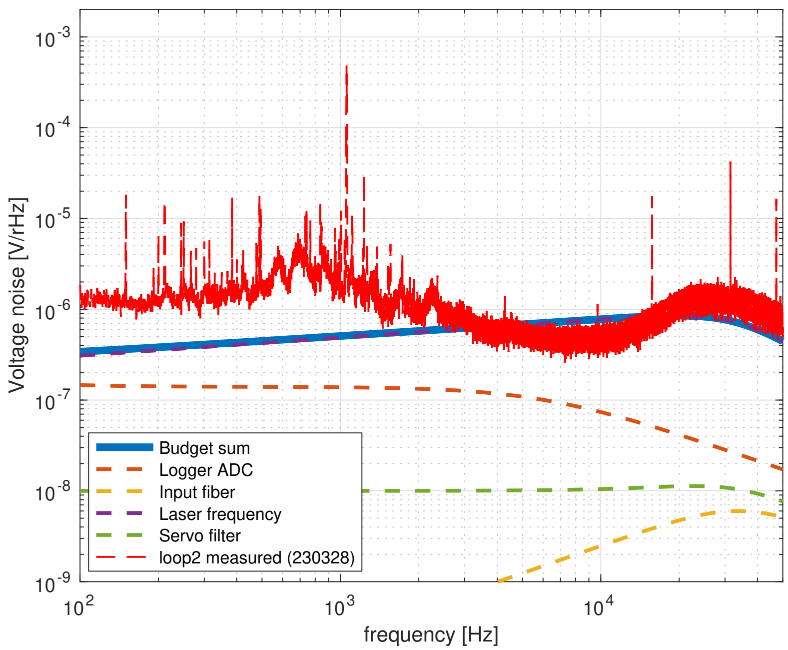

Figure 5.9: Amplitude spectral densities of measured frequency fluctuation at the error signal y_2 and various estimated noise contributions. (Dashed red) Measured noise without an excitation. (Thick blue curve) Quadrature sum of all known noise contributions. (orange dashed) digitization noise of ADC or analog-to-digital converter for the logger used for recording the signal. (Dashed purple) Suppressed laser frequency noise from laser 2. (Dashed green) Circuit noise in servo filter. (Dashed yellow) Optical fiber noise in input optics.

with a 50% overlap so that Welch's method [66] can be applied. The data length of each chunk N_C is N/n whereas the overall data length is N. We estimate the power spectral density $S(f)$ of the synthesized output X referred to the beatnote frequency by

$$\begin{aligned} S(f) &= \frac{2C}{T} \sum_{k=1}^{2n-1} \left| \frac{X^{(k)}}{S_{1\_\mathrm{est}} S_{2\_\mathrm{est}}} \right|^2 \\ &= \frac{2CT_S}{(2n-1)N_C} \sum_{k=1}^{2n-1} \left| \frac{y_1^{(k)}}{S_{1\_\mathrm{est}}} - \frac{y_2^{(k)}}{S_{2\_\mathrm{est}}} - \delta\nu_{b\_\mathrm{FR}}^{(k)} \right|^2 , \end{aligned} \tag{5.2}$$

where superscript (k) denotes the Fourier-transformed quantity using k-th chunk, T is a measurement duration, T_S is a sampling duration, and C is a correction factor specific to the window function. In our case, the Hann window was applied and the correction $C = 8/3$ was used.

Chapter 6
DEMONSTRATION OF SUBTRACTION

6.1 Demonstration of subtraction

Two sets of data were recorded at different times. One is without the frequency noise excitation for estimating the noise floor as shown in Figs. 5.7 and 5.8. The other is with the frequency noise excitation enabled as shown by the blue plots in Figs. 6.1 and 6.2. In both cases, the frequencies of lasers were locked to the Fabry-Perot cavities all the time, producing a continuous train of time series data.

To obtain an accurate estimation of the sensing transfer function S_j, we experimentally measured the transfer functions between the beatnote and the error signals. The sensing transfer function was modeled by a single-pole system,

$$S_{j\_\mathrm{est}}(f) = \frac{a_j \exp(-2\pi f \tau_j \mathrm{i})}{1 + \mathrm{i} f / f_{c,j}}, \tag{6.1}$$

as same as in Eq. 5.1. The measurement of the transfer functions includes also the response of the frequency readout G_{FR}. However, G_{FR} was measured independently and the effect was removed by applying its inverse in the frequency domain.

The measurements of the sensing transfer functions were performed in-situ by utilizing the data set with the excitation enabled. The measured transfer function and the result of fitting to the model (6.1) are shown in Figs. 6.3 and 6.4. The models S_{j_est} with the fitted parameters are used in the subtraction.

Fig. 6.5 shows the amplitude spectral densities of the beatnote signals with and without the offline subtraction. The red curve was obtained while keeping

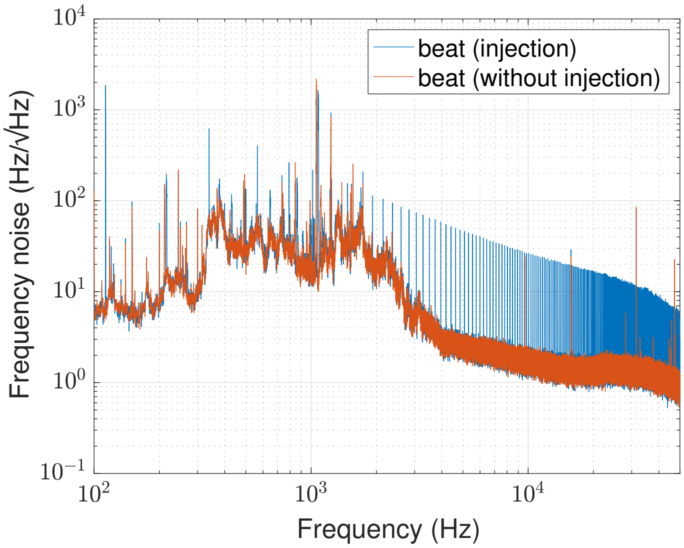

Figure 6.1: The amplitude spectral density of measured beatnote signal with frequency noise excitation (blue) and without frequency noise excitation (orange).

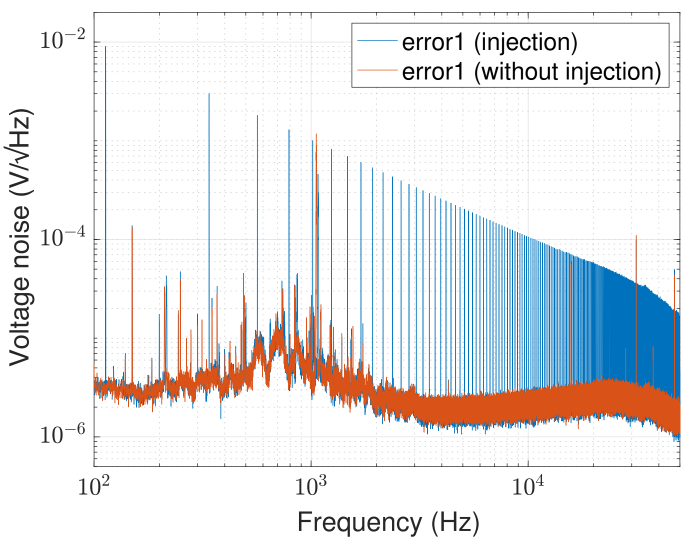

Figure 6.2: The amplitude spectral density of measured error signal 1 with frequency noise excitation (blue) and without frequency noise excitation (orange).

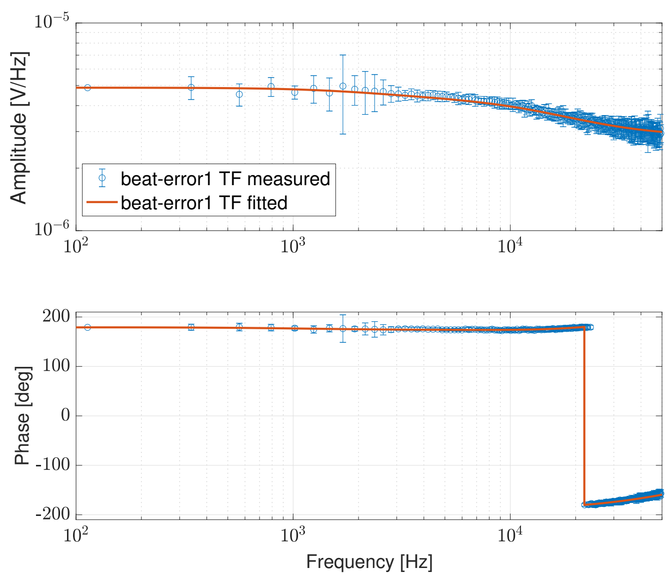

Figure 6.3: The measured transfer function between beat and error signal 1 (blue dots) and the fitted transfer function (orange solid). The dots indicate the values at the fundamental and harmonic frequencies of the excitation signal. The fit was performed using that portion of the signal.

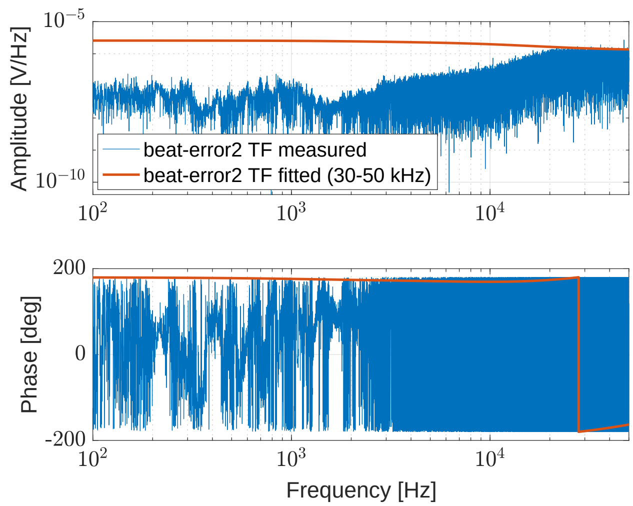

Figure 6.4: The measured transfer function between beat signal and the error signal 2 (blue solid) and the fitted transfer function (orange solid). No signal injection was performed on this side of the loop. However, as shown from the budget in Fig. 5.7, the transfer function is obtained with a relatively high signal-to- noise ratio in the high frequency band above about 30 kHz, where laser frequency noise is expected to dominate. The fitting was performed using the 30-50 kHz measurement results.

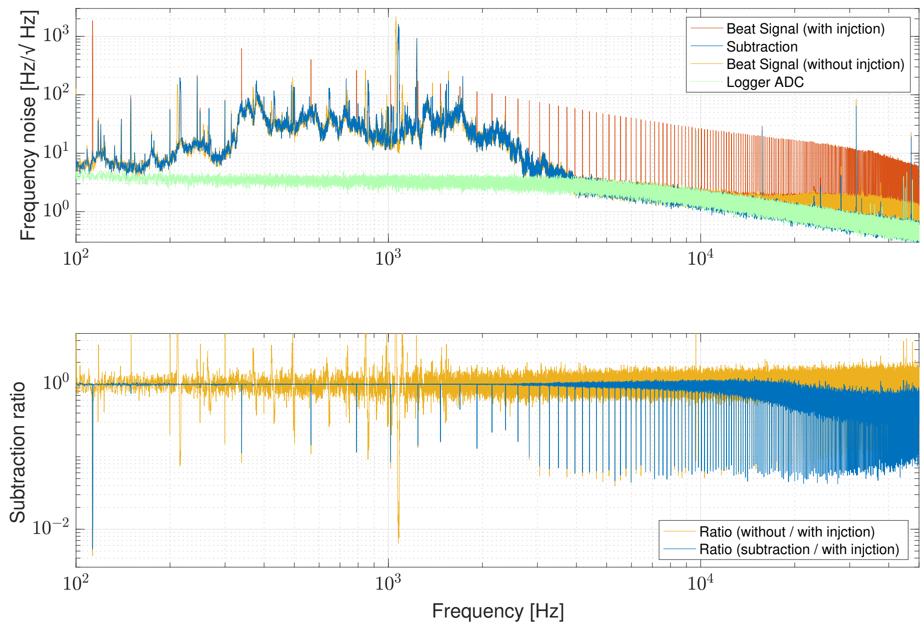

Figure 6.5: The subtraction results. In the top panel, (Blue) spectrum with the offline subtraction applied. (Red) without the subtraction applied. (Yellow) when no excitation was applied. (Green) The ADC noise of the data logger for the beatnote frequency. In the bottom panel, the ratios of spectra are shown. (Blue) Ratio of the spectra with the subtraction applied over the one without excitation signals. (Yellow) Ratio of the spectra without the subtraction applied over the one without excitation signals.

the square wave excitation enabled. As expected, the higher order harmonics at frequencies of odd integer multiples of 113Hz are clearly visible in the spectrum.

As seen in Fig. 6.5, the excitation peaks were successfully subtracted to the levels as low as the ambient noise floor not only in the low frequency region, where the sensing transfer functions S_j are almost constant, but also at around the cavity pole and frequencies above. In particular, a reduction of a broad continuum is confirmed at frequencies above 10 kHz by a factor of two at most compared to the spectrum without the excitation. In this region, the laser frequency noises are expected to be the dominant components as summarized in Fig. 5.7. This means that, albeit limited, the subtraction has been achieved without the aid of a deliberate excitation in this frequency region.

Figure 6.6 shows the subtraction ratio and the residuals at each excitation peak. The error bars in these plots are given by the 1-sigma uncertainties in the estimate of the power spectral density.

In the top panel of Fig. 6.6, the best noise subtraction ratio of 188 ± 29 is achieved at 113 Hz where the peak height is the highest relative to the ambient noise floor. The middle and bottom panels show respectively the residuals and the relative residuals normalized by the ambient noise floor. If the relative residual is 0, it means that the excitation is reduced to the noise floor. For example, some peaks, including the first to third and the fifth peaks at 113 Hz, 339 Hz, 565 Hz, and 1017 Hz, respectively, have significant residuals relative to the noise floor. On the other hand, in the high frequency region above 10 kHz, where frequency noise is expected to be predominant, not only the injection peaks but also the noise floor itself were reduced to the half of the original noise floor at best.

In Appendix A, we have verified that the subtraction can be performed in a different region from that used for the fitting. However, as discussed below, subtraction cannot be performed with sufficient accuracy if the transfer function of the system varies significantly after fitting.

6.2 Limiting factors in subtraction

The residuals in the subtraction can be primarily caused by features that were not modeled in the transfer function implemented to the subtraction in numerous peaks. At the same time, temporal variations in the system parameters could be critical for the peaks with fine subtraction ratios, such as the first peak.

To consider these effects, S_j is replaced to $S_j + \delta S_j$ by the stationary com-

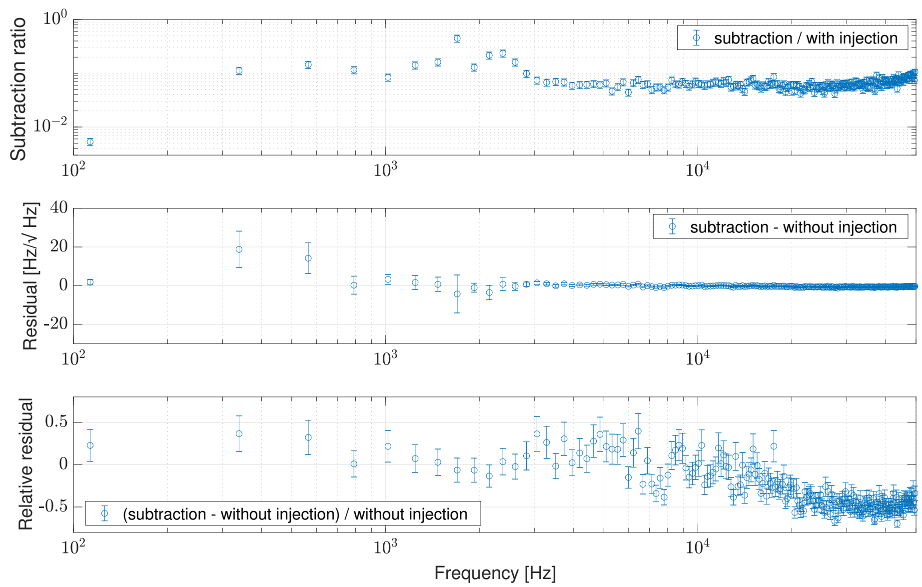

Figure 6.6: The top panel is the noise reduction ratio at each injection peak. The middle panel is the amplitude noise residual for the without injection state of the after subtraction, and the bottom panel is the corresponding relative value. Error bars are derived from the 1-sigma range of the power spectrum estimation error.

ponents S_j and fluctuating components δS_j. Similarly, the estimated value S_{j_est} is replaced to $S_j + \mathit{\Delta} S_j$ by the stationary component of the true value S_j and the stationary deviation $\mathit{\Delta} S_j$. In addition, $\delta\nu_\mathrm{b}$ is replaced with $\delta\nu_\mathrm{b} + \delta n_\mathrm{sen}$ to account for the sensing noise δn_sen. Plugging these into Eq. (4.5), the residual of frequency noise can be expressed as

$$\frac{\mathit{\Delta} X_{\nu\_\mathrm{residual}}}{S_{1\_\mathrm{est}}\, S_{2\_\mathrm{est}}} = \frac{1}{1+G_1}\frac{\Delta\mathrm{S}_1 - \delta\mathrm{S}_1}{\mathrm{S}_1 + \Delta\mathrm{S}_1}\delta\nu_1 - \frac{1}{1+G_2}\frac{\Delta\mathrm{S}_2 - \delta\mathrm{S}_2}{\mathrm{S}_2 + \Delta\mathrm{S}_2}\delta\nu_2 + \delta n_\mathrm{sen}. \tag{6.2}$$

Here, we assumed $G_{\mathrm{FR}\ \_\mathrm{est}} = G_\mathrm{FR}$ since the calibration with a known signal was performed, and the frequency readout response estimation is sufficiently accurate. The calibration details for G_FR are shown in appendix B.

Moreover, As an effect not taken into account in the Eq. (6.2), the residuals may be worse due to the nonlinear effects as mentioned below at the frequencies which are integer multiple of the peaks with large subtraction.

We now discuss the limiting factors with special attention to the first to third and fifth peaks at 113 Hz, 339 Hz, 565 Hz, and 1017 Hz, respectively, which have significant residuals. The main limiting factors and these contributions for each peak are summarized in Table 6.1. In what follows, we detail each factor.

6.2.1 Unmodeled features in transfer function

The sensing transfer function S_j was estimated by fitting the measurement as shown in Fig 6.3. To confirm the accuracy of the transfer function model, the phase and amplitude of the transfer function were tuned to minimize the residuals at the peak frequencies where there had been residuals. If there is a large improvement in the noise residual, it could indicate that there exist some features such as peaks and notches that are not taken into account in the model and implies that $\mathit{\Delta} S_j$ in Eq. (6.2) is significant. It is relatively difficult to find such unmodeled features in the regions where the signal-to-noise ratio of the measurement is low.

The residual noises after tuning are shown in the row 6 of Table 6.1. There was no significant improvement in the fundamental peak at 113 Hz and the second peak at 339 Hz. On the other hand, the residuals improved by approximately half for the third peak at 565 Hz and the fifth peak at 1017 Hz. Therefore, it is possible that a local feature in the transfer function is the main cause of the deterioration in the subtraction ratio for the third and fifth peaks whereas the residuals in the first and second peaks seem to be due to other factors.

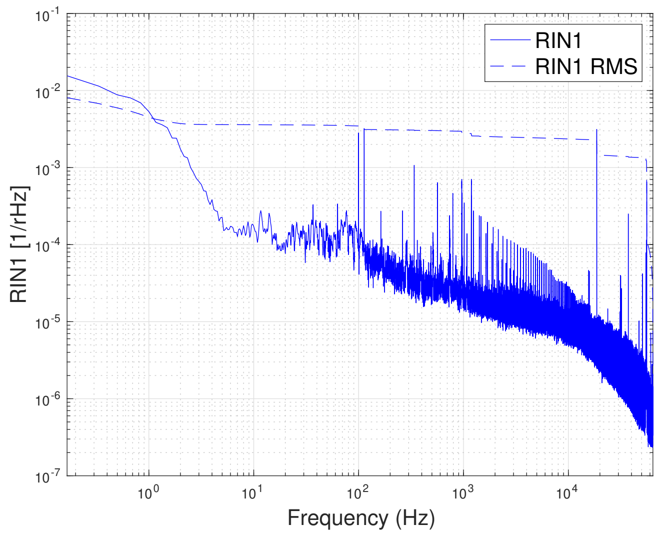

Figure 6.7: The measured RIN and corresponde RMS of the trans transmitted beam of cavity 1

6.2.2 Temporal variation in system

Temporal variations in the system parameters represented by δS_j in Eq. (6.2) alter the sensing transfer function S_j as a function of time. This could limit the subtraction ratio, too. To study the stability of the parameters associated with the sensing transfer function, the transmitted light of the cavities have been monitored.

As shown in Fig. 6.7, The RMS (root mean square) of the RIN (Relative Intensity Noise) was measured to be 0.81 % for cavity 1. This transmitted light RIN could be attributed to the variation of the incident laser power into the cavity or the variation of the optical gain. The latter is caused by changes in the transmittances of the cavity mirrors or the internal loss of the cavity. However, it was difficult to distinguish which parameter dominated in the RIN. Therefore, we consider the case where one of them is dominant.

The amplitude variation of the PDH signal can be directly regarded as the variation of the sensing transfer function amplitude δa_j. Therefore, we evaluated δa_j as a function of the RIN for the transmitted light. For convenience, we introduce the relation $\delta a_j/a_j = \alpha RIN$ with α being a constant of real value. We show that the coefficient α takes different values depending on what parameter

Table 6.1: Residual noise at each peak and contribution of possible main factors.

Peak number	1st (113 Hz)	2nd (339 Hz)	3rd (565 Hz)	5th (1017 Hz)	Above 5th
Subtraction ratio	0.53 ± 0.08 %	11.3 ± 1.7 %	14.5 ± 2.2 %	8.4 ± 1.3 %	> 4 %
Reduction ratio	188 ± 29	8.9 ± 1.4	6.9 ± 1.1	11.9 ± 1.8	< 25
Noise residual	1.8 ± 1.4 Hz/$\sqrt{\mathrm{Hz}}$ (0.23 ± 0.19)	18.8 ± 9.4 Hz/$\sqrt{\mathrm{Hz}}$ (0.37 ± 0.21)	14.2 ± 7.9 Hz/$\sqrt{\mathrm{Hz}}$ (0.32 ± 0.20)	3.3 ± 2.6 Hz/$\sqrt{\mathrm{Hz}}$ (0.22 ± 0.19)	-
Temporal variation (typical value)	~ 0.81 %				
Noise residual after tuning	1.8 ± 1.4 Hz/$\sqrt{\mathrm{Hz}}$ (0.23 ± 0.19)	18.3 ± 9.4 Hz/$\sqrt{\mathrm{Hz}}$ (0.36 ± 0.21)	6.2 ± 7.3 Hz/$\sqrt{\mathrm{Hz}}$ (0.14 ± 0.18)	1.7 ± 2.4 Hz/$\sqrt{\mathrm{Hz}}$ (0.11 ± 0.17)	-
Nonlinear effects (estimated maximum)	-	8.3 ± 0.9 Hz/$\sqrt{\mathrm{Hz}}$	-	2.8 ± 0.2 Hz/$\sqrt{\mathrm{Hz}}$	-
Sensing noises	Not effective in the demonstration with the noise injection				

is the cause for the variations.

In the case where the cause of the variation is either the power of the incident light, the transmittance of the cavity input mirror, or the loss in the cavity, the coefficient becomes $\alpha = 1$. These parameters affect the PDH signal and the transmitted light intensity in the same way. On the other hand, in the case where the variation of the PDH signal is caused by the variation in the transmittance of the end mirror, the coefficient takes a value much smaller than unity or $\alpha \ll 1$. This is confirmed by performing the partial differentiation of the expression for the PDH signal and the transmitted light with respect to the end mirror transmittance. We find that the coefficient can be approximated to be T_e/L where L is the loss in the cavity and T_e is the power transmittance of the end mirror. Assuming $T_e = \sim 10^{-5}$ and $L = \sim 10^{-2}$ for our experimental setup, we estimated the coefficient α to be on the order of 10^{-3}. In this case, the PDH signal is almost unaffected even when the transmitted light power fluctuates.

Since sub-percent levels of variations are unlikely to occur in the mirror transmittance, the variations may be mainly due to the incident laser power and the loss in the cavity. Thus, the relative variations in the PDH signal should equal the transmitted light RIN or $\alpha = 1$.

Although the RMS value of 0.81 % for RIN represents the typical value of variability, this measurement suggests that the amplitude of the sensing transfer function a_1 fluctuates at the sub-percent level. Given the fact that the subtraction ratio at the first injection peak at 113 Hz was about 0.5 % in accuracy, time variations of a_1 may be the main factor for the residuals. Further investigation is necessary to achieve a more stable system in the future.

A similar RIN of about 1.1 % is also observed for cavity 2. However the influence of laser 2 on the injection peaks is negligible and does not affect the subtraction ratio.

For the peaks at the second harmonic and higher, the subtraction accuracies are about 4 % at best. Thus, the effect of temporal variation is not critical.

6.2.3 Sensing noises

Noise coupled after the laser light is split into the back-link and cavity sides becomes an uncorrelated component between the beatnote and error signals. Therefore, such noises, expressed as δn_{sen} in Eq. (6.2), cannot be subtracted and contaminate the detector sensitivity directly. The main candidates for such sensing noises are phase noise introduced by mirror reflections, optical fibers, air disturbances in the free space region, etc., or noise introduced from the phasemeter, and ultimately shot noise in the backlink heterodyne.

As shown in Fig 5.7, the unidentified noise below 4 kHz and ADC noise of the data logger at high frequencies are examples. Although these noises were not a problem in our demonstration because of the relatively high excitation peaks, they would be critical factors if a lower noise level is pursued. Even if an excitation is applied to the laser frequencies, the sensing noise must be sufficiently reduced because the excitation with a too high amplitude would worsen the state of resonance and lead to an enhancement of the nonlinear effects.

For phase noise, there are ideas for common-mode rejection of fiber phase noise by acquiring beat signals at two photodetectors, as shown in Fig 4.1b. An alternative is to lock the length of the back-link heterodyne path to some stabilized reference. Additionally, it is essential to develop a low noise phasemeter. Shot noise can be reduced without reducing the light power sent to the cavity using the heterodyne squeezing scheme [67].

6.2.4 Nonlinearities

The PDH signal is known to come with nonlinearity. The response is not a mere linear line but exhibits an S-shaped curve with respect to the laser frequency. This directly means that the error signal contain higher order terms together with the linear. When the subtraction is performed for a specific frequency, noises are expected to worsen at the multiplier frequency.

The PDH signal V_{PDH} can be expressed as follows based on Fig 3.55, assuming that the modulation sidebands are sufficiently far apart from the resonant frequencies of the cavity.

$$V_{PDH} \propto \frac{\sin\phi}{1 + R^2 - 2R\cos\phi}, \tag{6.3}$$

where ϕ is the phase deviation from a resonance point and R is the product of the amplitude reflectivities of the input and output mirrors of the cavity. R is given as follows using the cavity finesse $\mathcal{F}$.

$$R = \frac{2\mathcal{F}^2 + \pi^2 - \pi\sqrt{4\mathcal{F}^2 + \pi^2}}{2\mathcal{F}^2}. \tag{6.4}$$

Figure 6.8 shows the values of the higher-order components normalized by the linear-order component when Eq. (6.3) is expanded by the power series of ϕ. We have assumed that the operating point is at a perfect resonance without

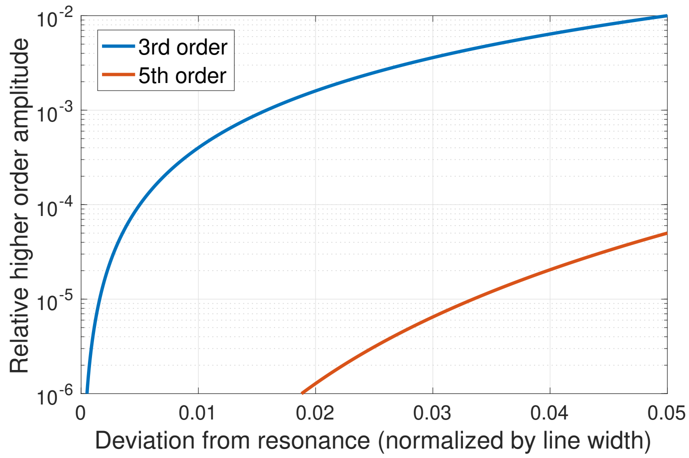

Figure 6.8: The contribution of the higher-order terms relative to the first-order term in the Pound-Drever-Hall signal. The horizontal axis is the deviation from resonance normalized by the cavity linewidth.

considering the effect of offsets for simplicity. Note that this effect would be larger and the even-order contents would appear in the presence of offsets.

The measurement of the transmitted light suggested that the laser frequency fluctuated around the resonance by 2 kHz at most during the excitation test. Therefore, we assume a deviation of about 1 kHz from the resonance. This corresponds to approximately 1/30 of the cavity linewidth. In this case, the effect of the third-order term, which is the most dominant among the higher-order terms, is $\sim 4.5 \times 10^{-3}$ for the first-order term. Therefore, the excitation can introduce the additional noise of the peak amplitude multiplied by this factor at a tripled frequency via the nonlinear effect. The effect of the fundamental peak at 113 Hz on the second peak at 339 Hz and the effect of the second peak at 339 Hz on the fifth peak at 1017 Hz are shown in row 7 of Table 6.1. At the second peak, this effect could be the main cause of the residual. Also, part of the residuals in the fifth peak can be caused by this effect. For harmonic peaks higher than the fifth order, the peak height monotonically decreases by the nature of the square waves. Therefore, the nonlinear effects are less likely to appear.

6.3 Implications for the space gravitational wave antenna and future prospect

Assuming 10^{-23} $/\sqrt{\text{Hz}}$ as the target sensitivity like B-DECIGO for the amplitude of gravitational waves, a noise level of 6×10^{-10} Hz/$\sqrt{\text{Hz}}$ will be required for the the laser frequency of 6×10^{14} Hz with a signal-to-noise ratio of 10 incorporated. Such a noise levels have to be achieved by allocating the capabilities of the initial stability of the laser frequency, the suppression gain of the frequency-locked loop, and the offline noise subtraction, respectively. The reduction by a factor of 10^8 is necessary even if we assume an excellent initial stability of 0.1 Hz/$\sqrt{\text{Hz}}$ which is currently achieved on a laboratory scale [68].

The proposal paper [35] assumed a conservative value of 10^4 for the suppression factor in the frequency-locked loop. The rest of the reduction by 10^4 must be achieved by the offline noise subtraction. In this scenario, the reduction ratio of ~200 achieved in our experiment needs to be improved by another factor of 50. Figure 6.9 shows a comparison of the frequency noise and B-DECIGO sensitivity for several assumed subtraction ratios, including the currently achieved subtraction ratio of 200. It is assumed here that similar subtraction ratios can be achieved in all frequency ranges. However, the frequency dependence of the subtraction ratio needs to be verified in the future. The laser initial frequency stability was assumed to be 0.1 Hz/$\sqrt{\text{Hz}}$ with no frequency dependence.For the frequency-locked loop, a DC gain of 80 dB and a UGF of 3 kHz were assumed. In Fig. 6.9, only the frequency noise is simply considered. However, in reality, as summarized in the sensing noise section above, laser intensity noise, phasemeter noise in the beat acquisition, beat shot noise, etc., must also be taken into account.

A more aggressive control gain in the frequency-locked loop might achieve the requirement even with the current reduction ratio of the subtraction. However, in future missions such as DECIGO will require 10^{-24} $/\sqrt{\text{Hz}}$ or better in the sensitivity [24]. Moreover, regardless of the scenario, the relaxation of design requirements for hardware, such as lasers and control systems, resulting from the improvement of the reduction ratio of the subtraction, is important for spacecraft.

For these reasons, we are planning to upgrade the experimental setup to achieve a high reduction ratio of the subtraction over 10^4. To achieve this, we have to identify the dominant factors causing time variations and stabilize the system. It is also important to address nonlinear effects to achieve high reduction ratio at broad frequencies.

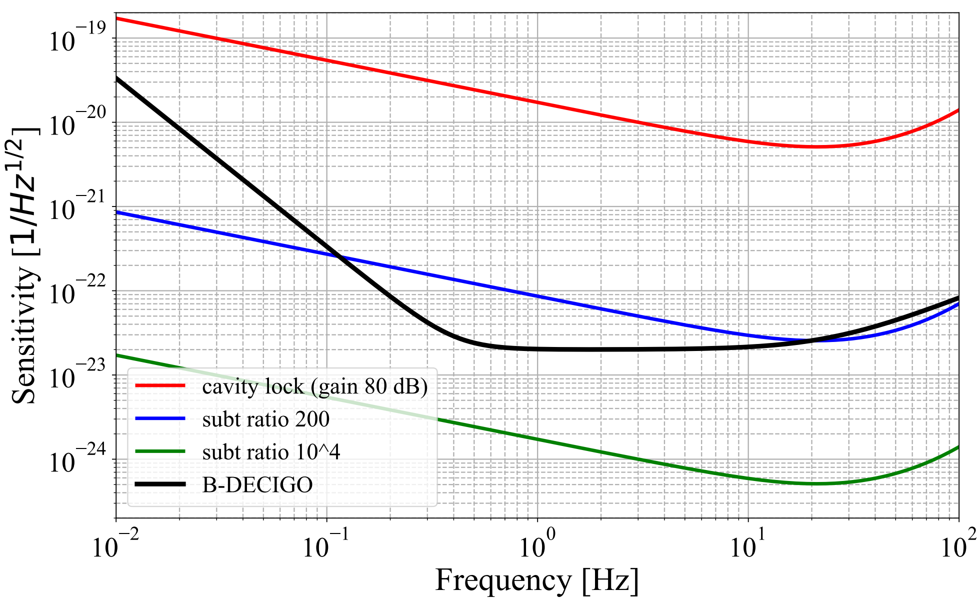

Figure 6.9: Comparison of laser frequency noise and BDECIGO sensitivity for each subtraction ratio.

Possible hardware upgrades include the introduction of a vacuum environment, a vibration isolation system, and a monolithic optical system. We also plan to introduce a much tighter frequency-locked loop to reduce nonlinear effects, as well as an additional system controlling the offset in the operating point using the transmitted light.

As for improvements to the subtraction process, we plan to implement an adaptive transfer function that takes into account the temporal variation of the system [69], an advanced subtraction process that takes into account nonlinear effects, and a time domain process to avoid the undesirable residuals expected in the finite-length Fourier transform.

Chapter 7
CONCLUSION

We have experimentally demonstrated for the first time the laser frequency noise subtraction in the back-linked Fabry-Perot interferometer. A miniature of the interferometer was built on a tabletop under atmospheric pressure where two identical Fabry-Perot cavities simulate a single set of the back-linked Fabry-Perot interferometer. Deliberately increasing noise in the laser frequency, we succeed in subtracting laser frequency noises in the broad frequency band, including the cavity pole frequency. We confirmed that the highest subtraction ratio reached 188 ± 29 at 113 Hz. This marks the experimental proof of the concept for the noise subtraction for the first time.

Currently, the subtraction performance at the frequency where the highest subtraction ratio has been achieved seems to be limited by temporal variations of the system parameters. In addition, a large noise amplitude at a frequency may exacerbate residuals at frequencies integer multiple to the original through the nonlinearity of the error signal. Such nonlinear effects could become a critical issue when performing large subtractions over a broad frequency bandwidth in future. To demonstrate a higher subtraction ratio, we plan to upgrade the setup by stabilizing the experimental system and implementing an advanced subtraction process.

Appendix A
SUBTRACTION AT A DIFFERENT TIME FROM THE DATA USED FOR FITTING

It may appear obvious that subtraction can be demonstrated in the same time region as the time region used for the fitting. In this chapter, we confirm that subtraction can be performed in a different time region used for the fitting.

A.1 Division and stability of data

As shown in Fig. A.1, the acquired time series data is divided into two regions: the first half and the second half. Hereafter, the first region is labelled 'A' and the second half region is labelled 'B'. This is the same data used in the demonstration in Chapt. 6. The RIN of transmitted light in cavity 1 in each region is shown in Fig. A.2. In the course of this verification process, it was found that the stability of the data of B is worse than that of A by a factor of 1.7, as shown in the plot. This fact is an important clue in the search for the cause of time variability in the experimental system. A detailed investigation is required in the future.

A.2 Verification of subtraction

I performed a fitting on the transfer function between the beat and error signals in each region. After the fitting, I performed a subtraction in each region. There are four possible combinations, including those that use the same data as the fitting. The results of the subtraction and the residuals of the subtraction for each combination are shown in Figs. A.3 to A.10.

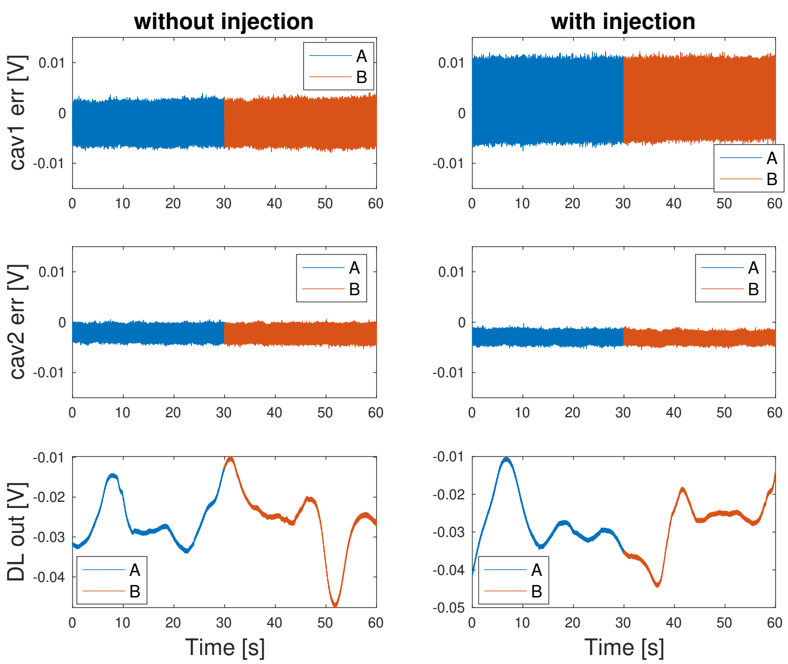

Figure A.1: Data divided in the time domain.

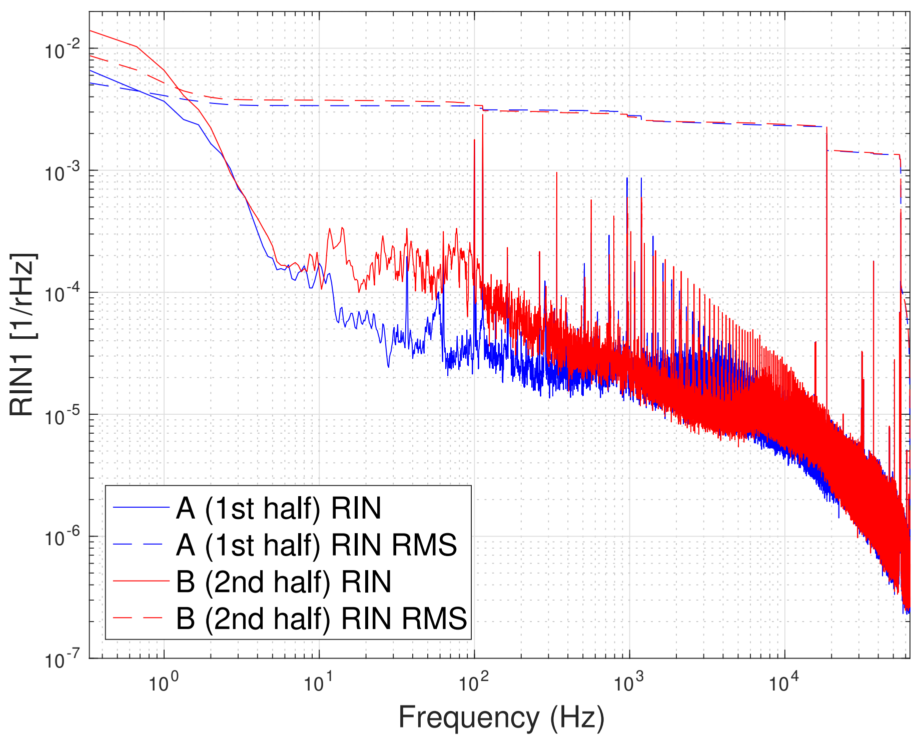

Figure A.2: The RIN of the cavity transmitted light in each time region.

First, we focus on the noise residuals resulting from subtraction in the stable time region A. Although this is not the original purpose of this verification, the result of using the fitting parameters obtained in the same region A used for subtraction is shown in Fig. A.4. This result shows that the residuals of the first peak, which was not able to reduce to a level below the floor in Chapt. 6, can be reduced to a level that includes the floor in its error bars. This result supports that a cause of residual at the first peak is temporal variation. On the other hand, for the subtraction ratio in Fig. A.3, the highest value is not improved because the peak height is lower by a factor of $1/\sqrt{2}$ due to the fact that the integration time has decreased by a factor of two. It can also be seen that the subtraction results using the parameters obtained from region B in Figs. A.5 and A.6 can be reduced to a level comparable to that discussed in Chapt. 6.

Next, the subtraction results in region B shown in Figs. A.7 to A.10, which has less stability, show that the residuals worsen regardless of the fitting data used. In particular for the low-order peaks with high subtraction ratios. On the other hand, the relatively high-order peaks still showed noise reduced to the floor or lower level. This is because their subtraction ratios are not high enough to be affected by time variation.

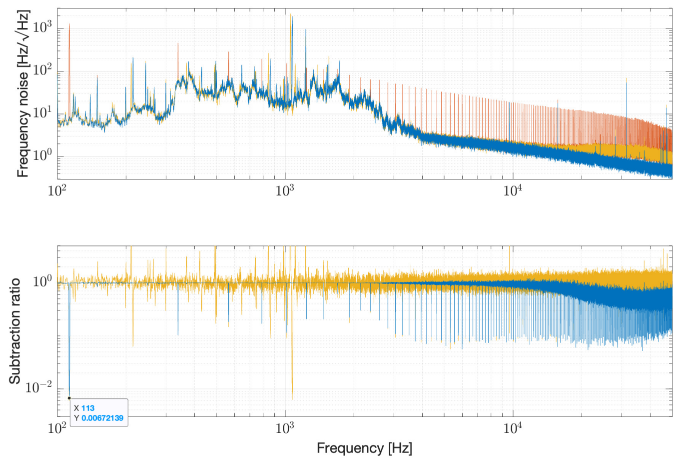

Figure A.3: Result with fitting region A, subtraction region A.

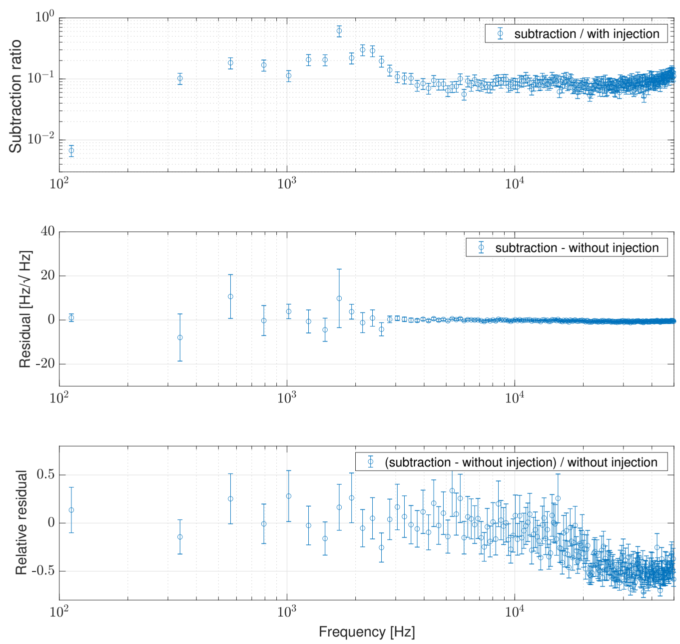

Figure A.4: Noise residuals with fitting region A, subtraction region A.

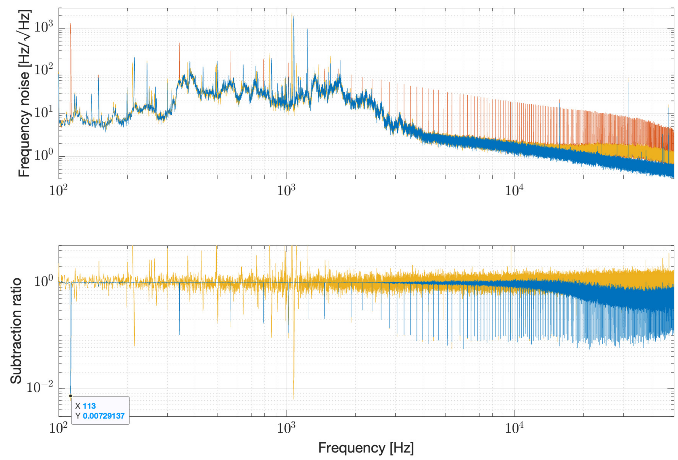

Figure A.5: Result with fitting region B, subtraction region A.

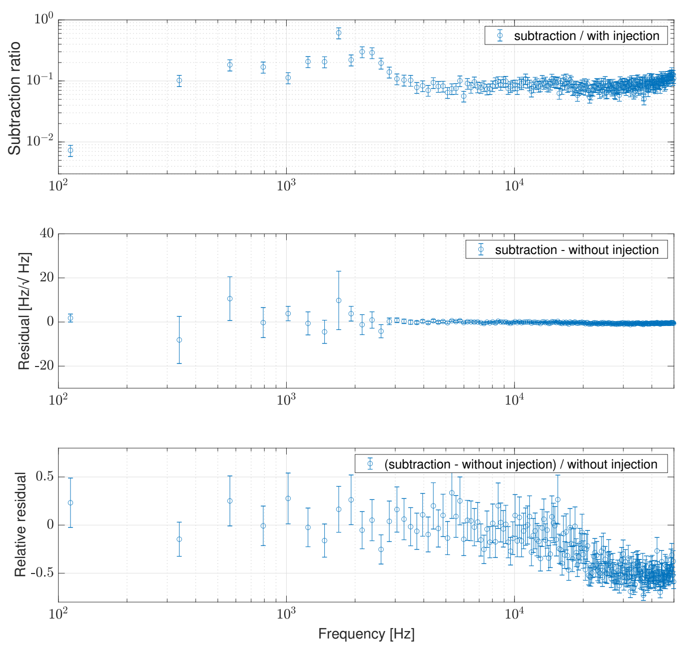

Figure A.6: Noise residuals with fitting region B, subtraction region A.

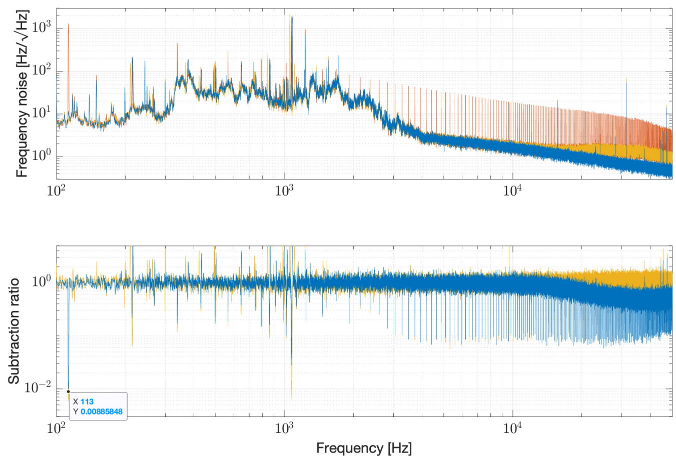

Figure A.7: Result with fitting region B, subtraction region B.

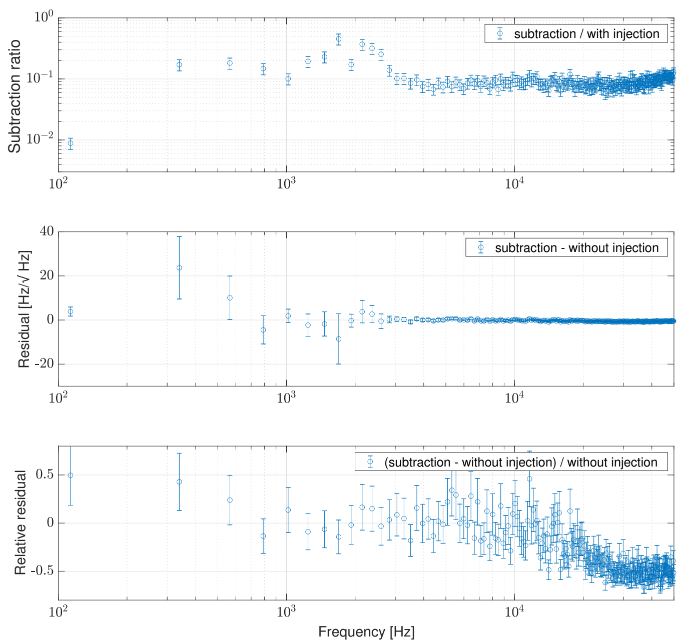

Figure A.8: Noise residuals with fitting region B, subtraction region B.

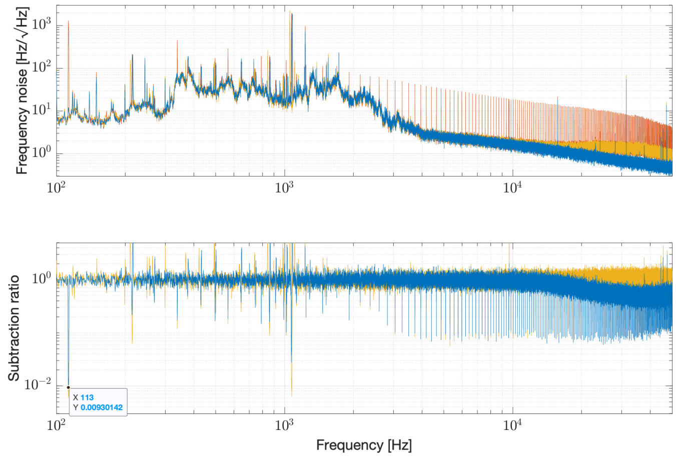

Figure A.9: Result with fitting region A, subtraction region B.

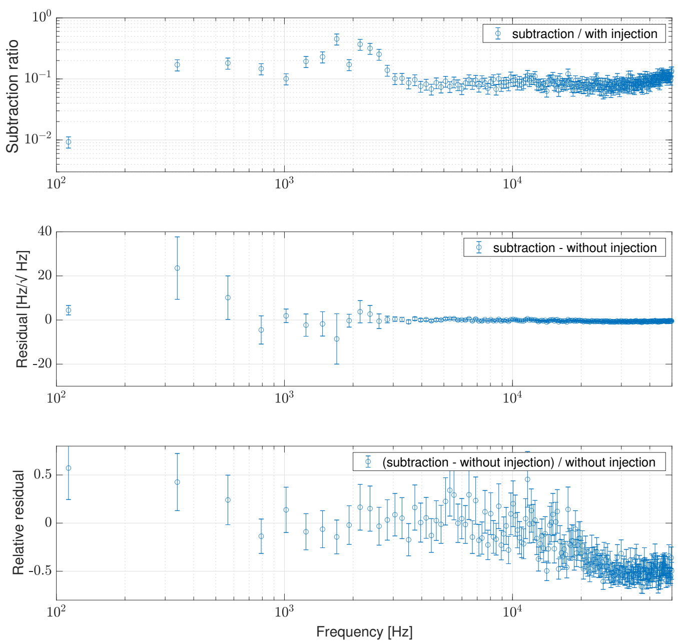

Figure A.10: Noise residuals with fitting region A, subtraction region B.

Appendix B

RESPONSE MEASUREMENT OF THE FREQUENCY READOUT

B.1 Phase meter response

In this section, I describe the details of the measurement of the response of the phasemeter (Moku:Lab, Liquid instruments).

The measurement was performed by using Moku:Go, a multi-measurement device. Moku:Go has a function that compares the phase and amplitude of the output excitation signal and the input signal at each frequency to obtain the transfer function.

The measurement system is shown in Fig. B.1. First, frequency modulation is applied to the RF output of the FG (DSG821) by the excitation signal from the MokuGo. Then the RF signal from the FG is input to the phase meter, and the frequency fluctuation of RF output, which is phase locked to the input, is read out by the delay line and returned to MokuGo for transfer function measurement. In the above measurement, the obtained transfer function includes the response of the FG and delay line. So the same measurement was performed in the state without the phase meter (Fig. B.2), and the transfer function of the phase meter was obtained by dividing the first obtained transfer function by the second obtained transfer function.

The results of the above two measurements are shown in Fig. B.3, and the transfer function of the phasemeter obtained from them is shown in Fig. B.4.

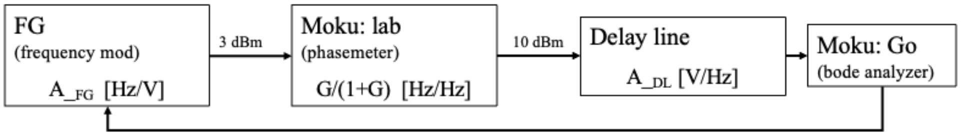

Figure B.1: Measurement includes phasemeter.

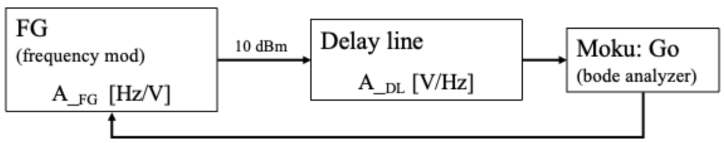

Figure B.2: Measurement without phasemeter.

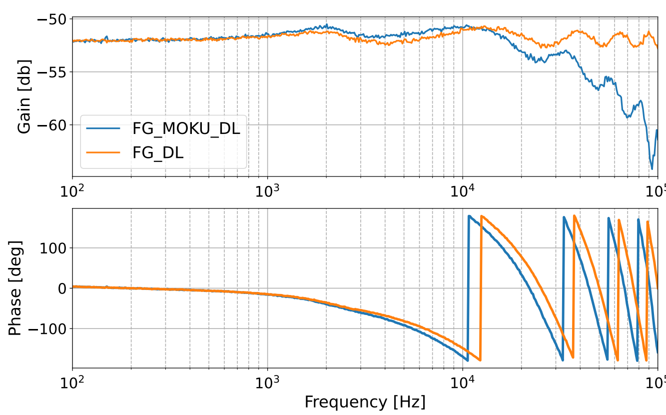

Figure B.3: Obtained TFs with Fig. B.1 setting and B.2.

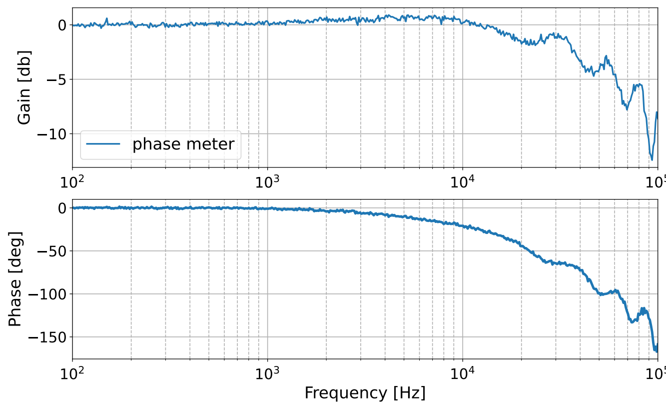

Figure B.4: Obtained phasemeter response.

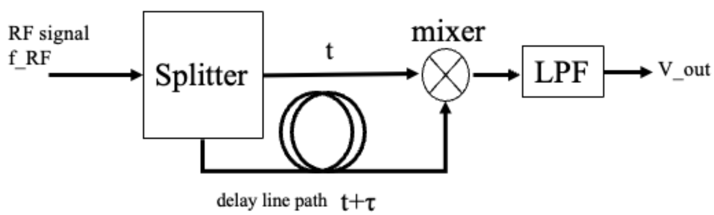

Figure B.5: The schematic view of the delay line frequency readout.

B.2 Delay-line response

The delay line frequency readout can obtain the DC voltage signal, which is proportional to the frequency of the RF signal, by splitting the RF signal and multiplying these signals by a mixer. The schematic view of the delay line frequency readout is shown in Fig B.5.

Assuming that the relative time delay between the two split paths is τ and the frequency of the input FR signal is $f_{\_\mathrm{RF}}$, the output voltage of the delay line frequency readout $V_{\_\mathrm{out}}$ can be expressed as follows.

$$V_{\_\mathrm{out}} = \zeta \cos\left(2\pi f_{\_\mathrm{RF}} \tau\right). \tag{B.1}$$

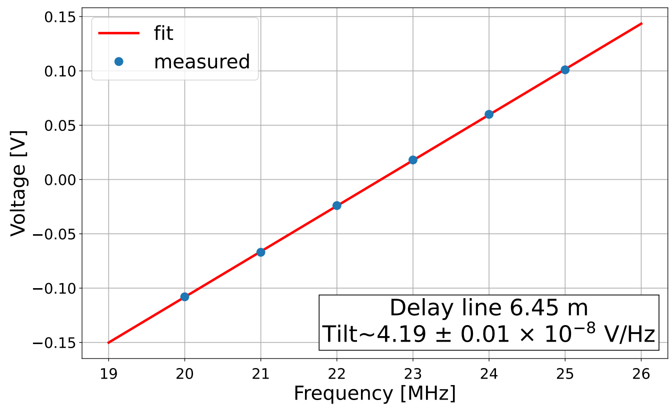

Figure B.6: Delay line output with each frequency.

Especially around the linear range,

$$V_{\_out} \approx 2\pi f_{\_RF}\tau\zeta. \tag{B.2}$$

Namely, by choosing an appropriate tau for the value of $f_{\_RF}$ and bringing the output signal into the linear region, we can obtain an output voltage that is proportional to the RF signal frequency, and the conversion factor is $2\pi\tau\zeta$.

We adjusted the delay so that the around of the beat frequency got in the linear region and directly obtained conversion factor $2\pi\tau\zeta$ by applying a known frequency signal. The results are shown in Fig. B.6.

Appendix C
CONSIDERATION OF DATA LOGGER NOISE

Currently, in the layout of the back-link demonstration, the high-frequency region of the beat signal is limited by the readout noise of the data logger. The budget shown in Fig. 5.7 used actual measured value under conditions where the logger input was terminated with a 50-ohm resistor. The cause of the logger noise was considered to be ADC noise, but as shown below, the measured noise is about 27 dB worse than the theoretical value derived from the resolution of A/D conversion. Although countermeasures such as the introduction of a preamplifier can be considered, investigation of the essential cause is also necessary in the future.

C.1 General theory on ADC noise

Let us consider converting the analog signal to a digital signal with a minimum voltage resolution q. At this time, the converted signal has the deviation voltage e from the true value before conversion in the range of $-q/2 < e < q/2$, which becomes the ACD noise [70]. Assuming that the appearance of the e is constant over the $-q/2 < e < q/2$ range, it has the probability density function, as shown in Fig. C.1. The magnitude of the probability density is $1/q$ from the normalization condition. Thus, the expected value of the power of the ACD noise can be written as

$$\begin{aligned} \mathrm{E}\left(e^2\right) &= \int_{-\frac{q}{2}}^{\frac{q}{2}} \frac{1}{q} e^2 de, \\ &= \frac{q^2}{12}. \end{aligned} \tag{C.1}$$

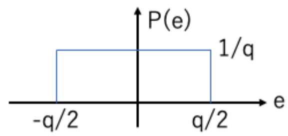

Figure C.1: Probability density function of e.

Therefore, the RMS value of the ADC noise voltage, $V_{\mathrm{ADC\_RMS}}$, by taking the root of Eq. (C.1) is,

$$V_{\mathrm{ADC\_RMS}} = \frac{q}{\sqrt{12}}. \tag{C.2}$$

On the other hand, the RMS of a sinusoidal signal voltage with full range swing can be written as

$$\mathrm{V}_{\mathrm{S\_(rms)}} = \frac{2^N q}{2\sqrt{2}}, \tag{C.3}$$

where N is the number of bits of the ADC. From Eq. (C.2,C.3), the best signal-to-noise ratio $\mathrm{SNR}_{\mathrm{max}}$ is

$$\begin{aligned} \mathrm{SNR}_{\mathrm{max}} &= 20 \log \frac{\mathrm{V}_{\mathrm{S\_(rms)}}}{V_{\mathrm{ADC\_RMS}}} \text{ [dB]}, \\ &= 20 \log \left(\frac{\sqrt{6}}{2} \right) + 20N \log 2 \text{ [dB]}, \\ &= 1.76 + 6.02N \text{ [dB]}. \end{aligned} \tag{C.4}$$

C.2 Measured Noise

The measured noise is shown in Fig. C.2. The RMS value of the noise is approximately 1.4×10^{-5} V. The RMS is taken from 100 kHz, which is the Nyquist frequency. On the other hand, a 16-bit logger (Yokogawa DL950 with Module 720256) is used for the measurement, with a voltage range of ± 70 mV. Thus the maximum signal RMS is 5×10^{-2} V. By plugging these into the first term of Eq. (C.4), the SNR can be obtained as approximately 71 dB. This is approximately 27 dB worse than the theoretical value 98 dB assumed from the 16-bit ADC.

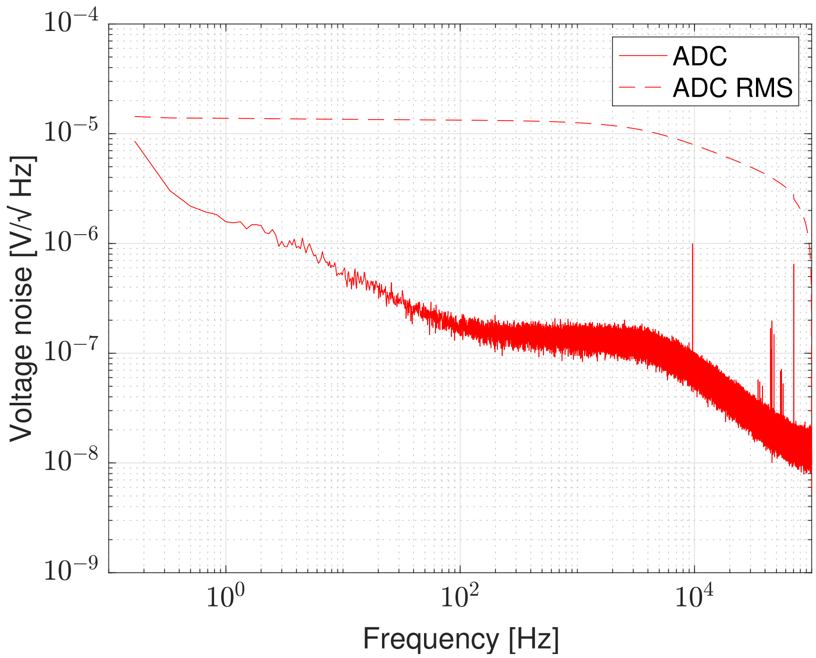

Figure C.2: PDH signal and cavity transmitted light near the resonance

Appendix D
DETAILS OF THE EXPERIMENTAL SETUP

This chapter presents the details of the BLFPI experimental setup.

D.1 Optical layout

Figure D.1 shows details of the optical layout. Table D.1 shows the model number of each optic. Figure D.2 shows an external view of the entire optical system.

D.2 Control system

Figure D.3 shows the layout of the BLFPI control system. Table D.2 shows the model number of each component.

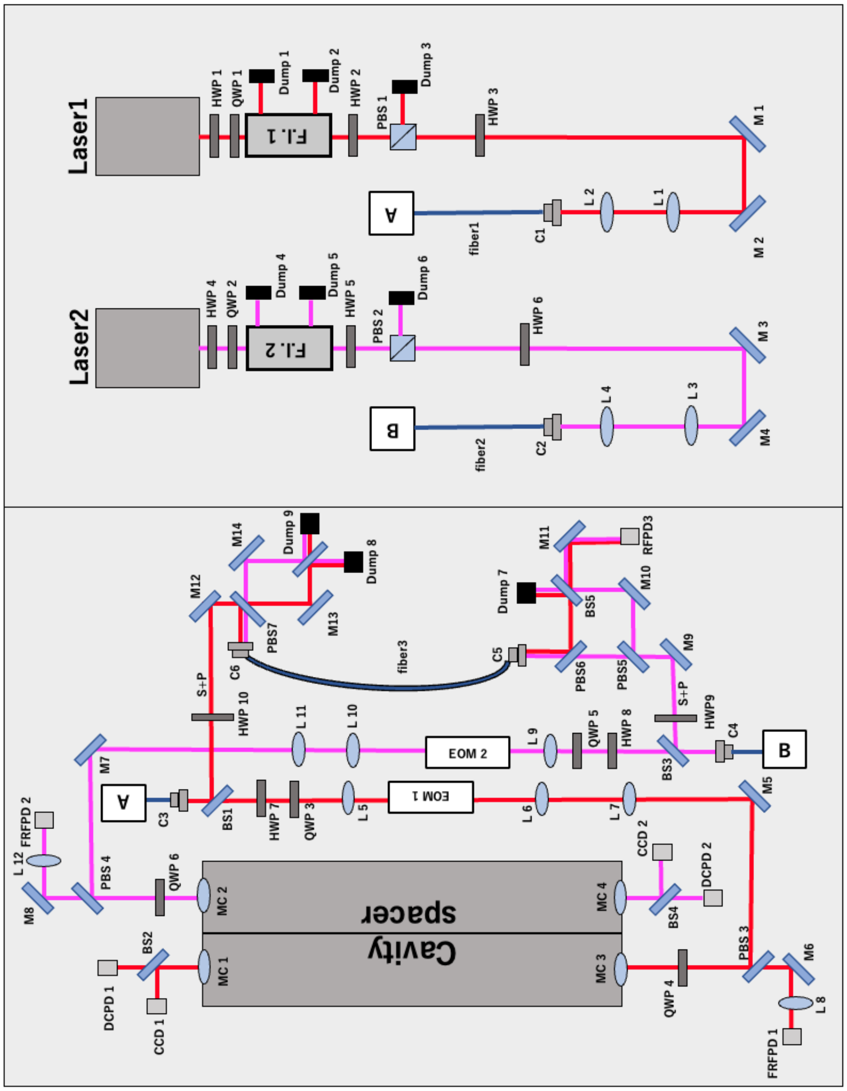

Figure D.1: The upper part of the figure shows the input optics, and the lower part shows the Fabry-Perot cavity and backl-inked interferometer. The light from the input optics is transmitted to the cavity side by the optical fiber. The 'A' and 'B' parts in the figure are connected by the same letter of the alphabet.

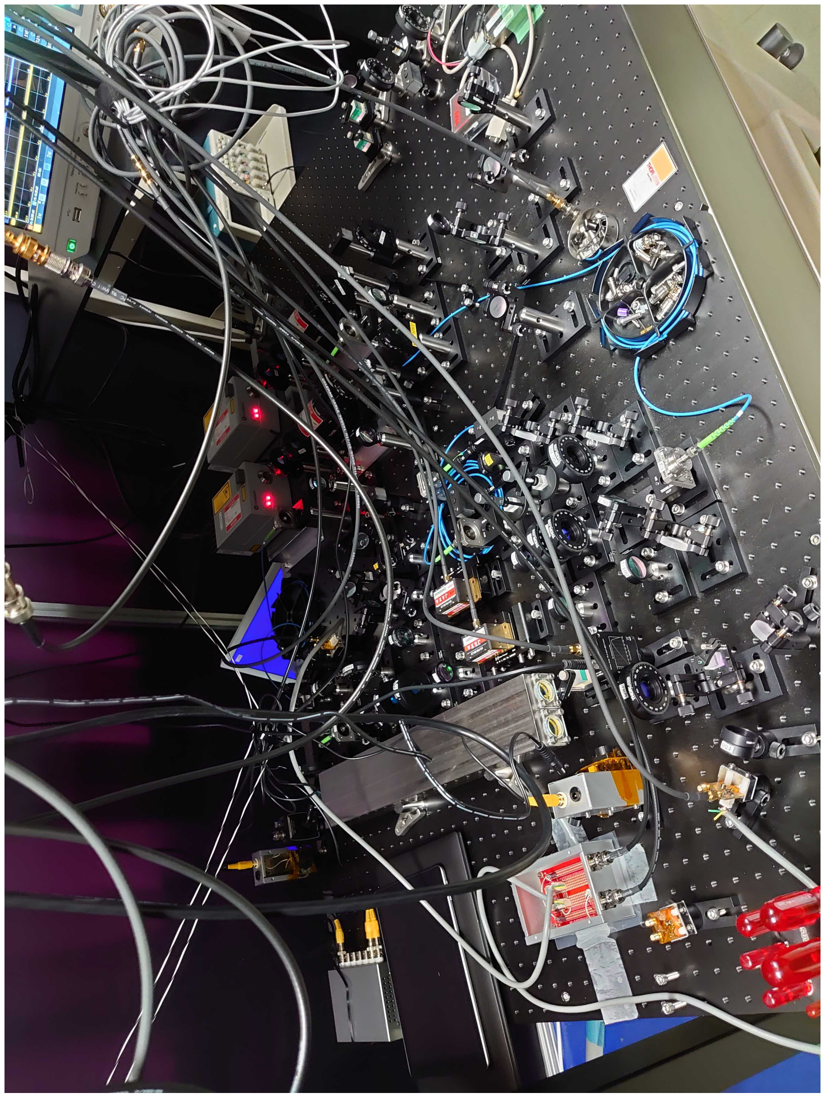

Figure D.2: A picture of external view of the optical system.

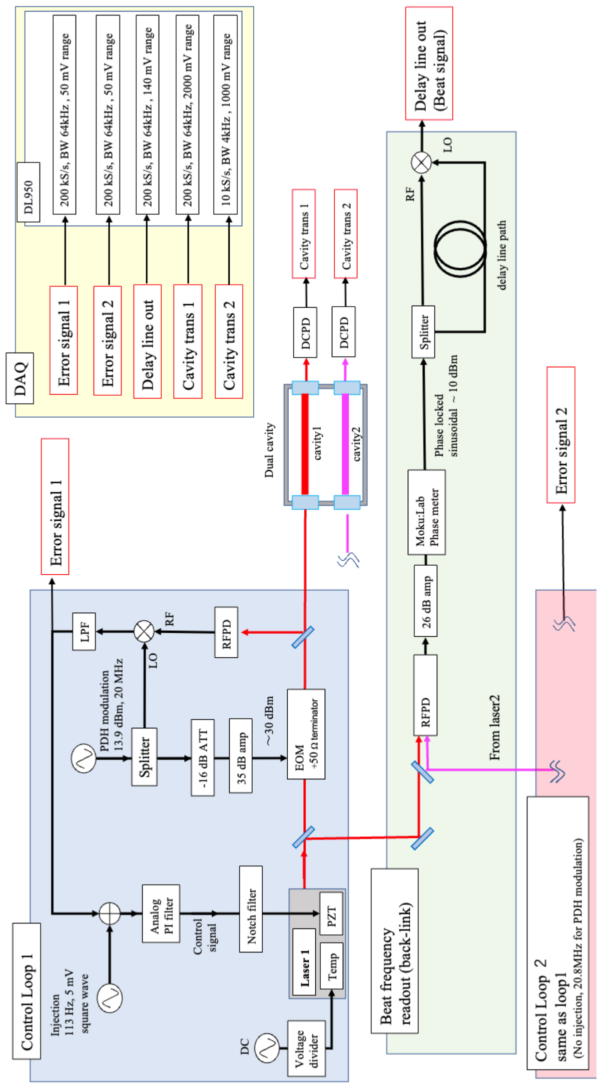

Figure D.3: The control system of BLFPI consists of the frequency lock portion of the laser (blue and red frames), the backlink heterodyne signal acquisition portion (green frame), and the data acquisition portion (yellow frame).

Table D.1: Model number list of optical components

symbol	property	model numbe
Laser1, 2	Laser	Mephisto S
M1-14	Mirror	BB1-E03 - Ø1
L1-L12	Lens	N-BK7 25.4 mm EFL 1064 nm
F.I. 1,2	Faraday Isolator	IO-5-1064-VLP
HWP 1,4-10	Half wave plate	10RP02-34
HWP 2,3,5,6	Half wave plate	FOCtec 25.4 mm Diameter HWP
QWP 1-6	Quarter wave plate	10RP04-34
PBS 1,2	Polarization beam splitter	FOCtec 12.7 mm cube
PBS 3,4,5,6,7	Polarization beam splitter	PBS12-1064
BS 1,3,5,6	Beam splitter	BSW41-1064
BS 2,4	Beam splitter	BS018
C1-6	Fiber collimator	PAF2A-A10C
fiber 1,2	Optical fiber	P3-1064PM-FC-2
fiber 3	Optical fiber	P3-1064PM-FC-1
MC1-4	Cavity mirror	layertec 107442
EOM 1,2	EO Phase Modulator	EO-PM-NR-C2
dump 1-8	beam dump	LB1(/M)
DCPD 1,2	photodetector	PDA100A
CCD 1,2	CCD camera	MTV-2510EM

Table D.2: Model number list of control components

symbol	model numbe
Injection oscillator	DSG821 (LF output)
DC Power Supply for Laser temperature tune	FG330
PI filter	LB1005
Modulation oscillator	DSG821 (RF output)
Mixer	ZFM-3-S+
Splitter	ZMSC-2-1+
LPF (Low pass filter)	SLP-1.9+
35 dB amplifier	ZX60-100VHX+
26 dB amplifier	ZFL-1000LN+
Data logger	DL950 (Module 720256) for 200 kS/s
Data logger	DL950 (Module 701262) for 10 kS/s

BIBLIOGRAPHY

[1] B. P. Abbott, R. Abbott, T. D. Abbott, M. R. Abernathy, F. Acernese, K. Ackley, *et al.*, "Observation of gravitational waves from a binary black hole merger," *Phys. Rev. Lett.*, vol. 116, p. 061102, Feb 2016.

[2] T. L. S. Collaboration, the Virgo Collaboration, the KAGRA Collaboration, R. Abbott, T. D. Abbott, F. Acernese, K. Ackley, C. Adams, N. Adhikari, R. X. Adhikari, V. B. Adya, C. Affeldt, D. Agarwal, M. Agathos, K. Agatsuma, *et al.*, "Gwtc-3: Compact binary coalescences observed by ligo and virgo during the second part of the third observing run," 2021.

[3] B. Abbott, R. Abbott, T. Abbott, *et al.*, "Prospects for observing and localizing gravitational-wave transients with advanced ligo, advanced virgo and kagra," *Living Review in Relativity*, vol. 23, no. 3, 2020.

[4] G. Agazie *et al.*, "The nanograv 15 yr data set: Evidence for a gravitational-wave background," *The Astrophysical Journal Letters*, vol. 951, p. 78, July 2023.

[5] R. X. Adhikari, "Gravitational radiation detection with laser interferometry," *Rev. Mod. Phys.*, vol. 86, pp. 121–151, Feb 2014.

[6] T. Matsubayashi, H. Shinkai, and T. Ebisuzaki, "Gravitational waves from merging intermediate-mass black holes," *The Astrophysical Journal*, vol. 614, p. 864, February 2004.

[7] C. Reisswig, C. D. Ott, E. Abdikamalov, R. Haas, P. Mösta, and E. Schnetter, "Formation and coalescence of cosmological supermassive-black-hole binaries in supermassive-star collapse," *Phys. Rev. Lett.*, vol. 111, p. 151101, October 2013.

[8] L. P. Grishchuk, “Amplification of gravitational waves in an isotropic universe,” *Journal of Experimental and Theoretical Physics*, vol. 40, p. 409, 9 1975.

[9] S. Kuroyanagi, T. Chiba, and N. Sugiyama, “Precision calculations of the gravitational wave background spectrum from inflation,” *Phys. Rev. D*, vol. 79, p. 103501, May 2009.

[10] T. Shimoda, S. Takano, C. P. Ooi, N. Aritomi, Y. Michimura, M. Ando, and A. Shoda, “Torsion-bar antenna: A ground-based mid-frequency and low-frequency gravitational wave detector,” *Int. J. Mod. Phys. D*, vol. 29, no. 4, p. 1940003, 2020.

[11] L. Badurina *et al.*, “Aion: an atom interferometer observatory and network,” *JCAP*, vol. 05, no. 011, 2020.

[12] M.-S. Zhan *et al.*, “Zaiga: Zhaoshan long-baseline atom interferometer gravitation antenna,” *Int. J. Mod. Phys. D*, vol. 29, p. 1940005, 2020.

[13] Y. A. El-Neaj *et al.*, “Aedge: Atomic experiment for dark matter and gravity exploration in space,” *EPJ Quantum Technology*, vol. 7, no. 6, 2020.

[14] H. J. Paik, M. V. Moody, and R. S. Norton, “Sogro — terrestrial full-tensor detector for mid-frequency gravitational waves,” *Int. J. Mod. Phys. D*, vol. 29, p. 1940001, 2020.

[15] P. Amaro-Seoane *et al.*, “Laser interferometer space antenna,” 2017.

[16] W.-H. Ruan, Z.-K. Guo, R.-G. Cai, and Y.-Z. Zhang, “Taiji program: Gravitational-wave sources,” *International Journal of Modern Physics A*, vol. 35, no. 17, p. 2050075, 2020.

[17] J. Mei *et al.*, “The TianQin project: Current progress on science and technology,” *Progress of Theoretical and Experimental Physics*, vol. 2021, 08 2020. 05A107.

[18] G. M. Harry, P. Fritschel, D. A. Shaddock, W. Folkner, and E. S. Phinney, “Laser interferometry for the big bang observer,” *Classical and Quantum Gravity*, vol. 23, p. 4887, jul 2006.

[19] K. A. Kuns, H. Yu, Y. Chen, and R. X. Adhikari, “Astrophysics and cosmology with a decihertz gravitational-wave detector: Tiango,” *Phys. Rev. D*, vol. 102, p. 043001, Aug 2020.

[20] W.-T. Ni, "Gravitational wave detection in space," *International Journal of Modern Physics D*, vol. 25, no. 14, p. 1630001, 2016.

[21] N. G. S. F. Center, "The gravitational wave spectrum with sources and detectors.," 2016. https://science.gsfc.nasa.gov/663/research/index.html.

[22] T. Nakamura *et al.*, "Pre-DECIGO can get the smoking gun to decide the astrophysical or cosmological origin of GW150914-like binary black holes," *Progress of Theoretical and Experimental Physics*, vol. 2016, 09 2016. 093E01.

[23] C. Cutler, "Angular resolution of the lisa gravitational wave detector," *Phys. Rev. D*, vol. 57, pp. 7089–7102, Jun 1998.

[24] S. Kawamura *et al.*, "Current status of space gravitational wave antenna DECIGO and B-DECIGO," *Progress of Theoretical and Experimental Physics*, vol. 2021, 02 2021. 05A105.

[25] S. Isoyama, H. Nakano, and T. Nakamura, "Multiband gravitational-wave astronomy: Observing binary inspirals with a decihertz detector, B-DECIGO," *Progress of Theoretical and Experimental Physics*, vol. 2018, 07 2018. 073E01.

[26] B. P. Abbott *et al.*, "Gw170817: Observation of gravitational waves from a binary neutron star inspiral," *Phys. Rev. Lett.*, vol. 119, p. 161101, Oct 2017.

[27] R. Takahashi and T. Nakamura, "The decihertz laser interferometer can determine the position of the coalescing binary neutron stars within an arcminute a week before the final merging event to the black hole," *The Astrophysical Journal*, vol. 596, p. L231, oct 2003.

[28] S. Vitale, "Multiband gravitational-wave astronomy: Parameter estimation and tests of general relativity with space- and ground-based detectors," *Phys. Rev. Lett.*, vol. 117, p. 051102, Jul 2016.

[29] N. Seto, S. Kawamura, and T. Nakamura, "Possibility of direct measurement of the acceleration of the universe using 0.1 hz band laser interferometer gravitational wave antenna in space," *Phys. Rev. Lett.*, vol. 87, p. 221103, Nov 2001.

[30] K. Sato, “First-order phase transition of a vacuum and the expansion of the Universe,” *Monthly Notices of the Royal Astronomical Society*, vol. 195, pp. 467–479, 07 1981.

[31] A. H. Guth, “Inflationary universe: A possible solution to the horizon and flatness problems,” *Phys. Rev. D*, vol. 23, pp. 347–356, Jan 1981.

[32] K. Nakayama, S. Saito, Y. Suwa, and J. Yokoyama, “Probing the reheating temperature of the universe with a gravitational wave background,” *Journal of Cosmology and Astroparticle Physics*, vol. 2008, p. 020, jun 2008.

[33] C.-F. Chang, “Imprint of early dark energy in stochastic gravitational wave background,” *Phys. Rev. D*, vol. 105, p. 023508, Jan 2022.

[34] C. Caprini, R. Durrer, T. Konstandin, and G. Servant, “General properties of the gravitational wave spectrum from phase transitions,” *Phys. Rev. D*, vol. 79, p. 083519, Apr 2009.

[35] K. Izumi and M.-K. Fujimoto, “A back-linked Fabry–Pérot interferometer for space-borne gravitational wave observations,” *Progress of Theoretical and Experimental Physics*, vol. 2021, 05 2021. 073F01.

[36] K. Nagano, H. Takeda, Y. Michimura, T. Uchiyama, and M. Ando, “Demonstration of a dual-pass differential fabry–perot interferometer for future interferometric space gravitational wave antennas,” *Classical and Quantum Gravity*, vol. 38, p. 085018, mar 2021.

[37] M. Tinto and J. W. Armstrong, “Cancellation of laser noise in an unequal-arm interferometer detector of gravitational radiation,” *Phys. Rev. D*, vol. 59, p. 102003, Apr 1999.

[38] F. Steier, R. Fleddermann, J. Bogenstahl, C. Diekmann, G. Heinzel, and K. Danzmann, “Construction of the lisa back-side fibre link interferometer prototype,” *Classical and Quantum Gravity*, vol. 26, p. 175016, 8 2009.

[39] R. Fleddermann, C. Diekmann, F. Steier, M. Tröbs, G. Heinzel, and K. Danzmann, “Sub-pm$\sqrt{\mathrm{Hz}}^{-1}$ non-reciprocal noise in the lisa backlink fiber,” *Classical and Quantum Gravity*, vol. 35, p. 075007, 2 2018.

[40] K.-S. Isleif *et al.*, “Towards the lisa backlink: experiment design for comparing optical phase reference distribution systems,” *Classical and Quantum Gravity*, vol. 35, p. 085009, 3 2018.

[41] B. Shutzt, *A First Course in General Relativity.* Cambridge University Press, 2010.

[42] R. Abbott, T. D. Abbott, F. Acernese, K. Ackley, *et al.*, "Gwtc-3: Compact binary coalescences observed by ligo and virgo during the second part of the third observing run," *Phys. Rev. X.*, vol. 13, p. 041039, Dec 2023.

[43] K. Hotokezaka, K. Kiuchi, K. Kyutoku, T. Muranushi, Y. ichiro Sekiguchi, M. Shibata, , and K. Taniguchi, "Remnant massive neutron stars of binary neutron star mergers: Evolution process and gravitational waveform," *Phys. Rev. D.*, vol. 88, p. 044026, Aug 2013.

[44] C. D. Ott, "Probing the core-collapse supernova mechanism with gravitational waves," *Classical and Quantum Gravity*, p. 204015, oct 2009.

[45] J. H. Taylor and J. M. Weisberg, "A new test of general relativity - Gravitational radiation and the binary pulsar PSR 1913+16," *The Astrophysical Journal*, vol. 253, p. 908, 1982.

[46] M. Maggiore, *Gravitational Waves. Vol.1, Theory and Experiments.* Oxford Univ. Press, 2008.

[47] R. Abbott *et al.*, "All-sky search for continuous gravitational waves from isolated neutron stars using advanced ligo and advanced virgo o3 data," *Phys. Rev. D.*, vol. 106, p. 102008, Nov 2023.

[48] D. Falta, R. Fisher, and G. Khanna, "Gravitational wave emission from the single-degenerate channel of type ia supernovae," *Phys. Rev. Lett.*, vol. 106, p. 201103, May 2011.

[49] S. Yoshida, "Decihertz gravitational waves from double white dwarf merger remnants," *The Astrophysical Journal*, vol. 906, p. 29, Jan 2021.

[50] C. Cutler and J. Harms, "Big bang observer and the neutron-star-binary subtraction problem," *Phys. Rev. D.*, vol. 73, p. 042001, Feb 2006.

[51] K. Yagi and N. Seto, "Detector configuration of decigo/bbo and identification of cosmological neutron-star binaries," *Phys. Rev. D.*, vol. 83, p. 044026, Feb 2017.

[52] P. Collaboration, "*Planck* 2018 results: . Cosmological parameters," *Astronomy & Astrophysics*, vol. 641, p. A6, 2020.

[53] J. Weber, "Gravitational-Wave-Detector Events," *Physical Review Letters*, vol. 20, pp. 1307–1308, June 1968.

[54] M. Goryachev, W. M. Campbell, I. S. Heng, S. Galliou, E. N, Ivanov, , and M. E. Tobar, "Rare events detected with a bulk acoustic wave high frequency gravitational wave antenna," *Phys. Rev. Lett.*, vol. 127, p. 071102, Aug 2021.

[55] J. Aasi *et al.*, "Advanced LIGO," *Classical and Quantum Gravity*, vol. 32, no. 7, p. 074001, 2015.

[56] F. Acernese *et al.*, "The Advanced Virgo detector," *Journal of Physics: Conference Series*, vol. 610, p. 012014, 2015.

[57] K. Komori, Y. Michimura, and K. Somiya, "Latest estimated sensitivity of kagra (v201708)," 2017. JGWdoc, JGW-T1707038-v9 (Internal).

[58] R. W. Drever, J. L. Hall, F. V. Kowalski, J. Hough, G. Ford, A. Munley, and H. Ward, "Laser phase and frequency stabilization using an optical resonator," *Applied Physics B*, vol. 31, pp. 97–105, 1983.

[59] J. D. E. Creighton and W. G. Anderson, *Gravitational-Wave Physics and Astronomy: An Introduction to Theory, Experiment and Data Analysis.* Wiley-VCH, 2011.

[60] A. J. Farmer and E. S. Phinney, "The gravitational wave background from cosmological compact binaries," *Mon. Notices Royal Astron. Soc.*, vol. 346, p. 1197–1214, Dec 2003.

[61] T. Robson, N. J. Cornish, and C. Liu, "The construction and use of lisa sensitivity curves," *Classical and Quantum Gravity*, p. 105011, apr 2019.

[62] S. Iwaguchi, T. Ishikawa, M. Ando, Y. Michimura, K. Komori, K. Nagano, T. Akutsu, M. Musha, R. Yamada, I. Watanabe, T. Naito, T. Morimoto, and S. Kawamura, "Quantum noise in a fabry-perot interferometer including the influence of diffraction loss of light," *Galaxies*, vol. 9, no. 1, 2021.

[63] M. Armano *et al.*, "Sub-femto-g free fall for space-based gravitational wave observatories: Lisa pathfinder results," *Phys. Rev. Lett.*, vol. 116, p. 231101, Jun 2016.

[64] Y. Enomoto, "Interferometer locking scheme for advanced gravitational-wave detectors and beyond," *Ph.D. thesis, University of Tokyo*, 2019.

[65] “Phase noise characterization of microwave oscillators – frequency discriminator method,” *Hewlett Packard, Product 11729C-2*, 1985.

[66] P. Welch, “The use of fast fourier transform for the estimation of power spectra: A method based on time averaging over short, modified periodograms,” *IEEE Transactions on Audio and Electroacoustics*, vol. 15, pp. 70 – 73, June 1967.

[67] K. Anai, Y. Enomoto, H. Omura, K. Nagano, K. Izumi, M. Endo, and S. Takeda, “Quantum-enhanced optical beat-note detection beyond 3-db noise penalty of image band,” 2023.

[68] K. Numata, A. Kemery, and J. Camp, “Thermal-noise limit in the frequency stabilization of lasers with rigid cavities,” *Phys. Rev. Lett.*, vol. 93, p. 250602, December 2004.

[69] D. Tuyenbayev *et al.*, “Improving ligo calibration accuracy by tracking and compensating for slow temporal variations,” *Classical and Quantum Gravity*, vol. 23, p. 015002, dec 2016.

[70] W. Kester, “Taking the mystery out of the infamous formula, ”snr = 6.02n + 1.76db,” and why you should care,” *Analog Devices, MT-001 TUTORIAL*, 2009.

ACKNOWLEDGMENTS

First of all, I would like to express my deepest gratitude to Professor Toru Yamada for accepting me and for his constant encouragement and support. I am also deeply grateful to Professor Kiwamu Izumi, who also accepted me and has supervised me since the master's program.

I would like to express my gratitude Prof. Tadayasu Doutani as Deputy Supervisor.

I would like to express my gratitude to Dr. Kentaro Komori and Dr. Koji Nagano. They have provided invaluable discussions and useful advice. I would like to express my gratitude to Kenji Fukunabe. He gave me valuable advice not only on electric circuits but also on everyday life.

I would like to express my gratitude to Yusuke Okuma for working with me to do the BLFPI research. I look forward to further development of his research in the future.

I would like to express my gratitude to Takuya Midooka, Hiroki Okasaka, Masami Watabe, Atushi Hoshi, Ryuto Naito, Yuma Norimoto, Karera Mori, Kairi Yakabe, and Takeshi Yoshizawa, who were colleagues in the same laboratory.

I would like to express my gratitude to Dr. Darkhan Tuyenbaye for supporting my research on time series calculations. I would like to express my gratitude to Dr. Yu Zhou, who has shown interest in and supported my research.

I would like to express my gratitude to thank Naoki Yahata, Shunichi Nakatubo, Yoshiaki Mitsutake, and Toru Kaga of the ISAS Advanced Machining Technology Group. In particular, the machining of the inverse spacer of the cavity is the work of Naoki Yahata.

I would like to express my gratitude to Dr. Yutaro Enomoto, Dr. Satoshi Tanioka, and Yohei Nishino for the FNC upgrade in KAGRA.

I would like to express my gratitude to Miyako Ukai, Kumiko Nishimatsu, Yoshikawa Tomoko, Nishino Etsuko, Oshizawa Rie, Naoko Fukayama, Miho Nakayama, Chifumi Hanyuu for their support as ISAS staff.

I would like to express my gratitude to Professors Nobuyuki Kanda, Masaki Ando, Takao Nakagawa, Motohide Kokubun, and Ikkooh Funaki of the Ph.D. thesis review committee.

I would like to express my gratitude to Prof. Tomoaki Toda and Dr. Shugo Oguri as commentators for the interim review. Professor Toda also provided me with the BLFPI optical table.

I would like to express my gratitude to all the other students and staff who supported and provided useful time at ISAS.

Finally, I would like to express my gratitude to my family for supporting, assisting, and encouraging me throughout the years.